VECTOR BACKSCATTERING AND ITS APPLICATION TO WIRELESS SENSING IN RADIO FREQUENCY IDENTIFICATION

By

Huan-Yang Chen

A dissertation submitted in partial fulfillment of

the requirements for the degree of

Doctor of Philosophy

(Electrical Engineering)

at the

UNIVERSITY OF WISCONSIN–MADISON

2012

Date of final oral examination: 12/05/11

The dissertation is approved by the following members of the Final Oral Committee:

Daniel van der Weide, Professor, Electrical and Computer Engineering
Dharmaraj Veeramani, Professor, Industrial and Systems Engineering
John Booske, Professor, Electrical and Computer Engineering
Akbar Sayeed, Professor, Electrical and Computer Engineering
Nader Behdad, Assistant Professor, Electrical and Computer Engineering

ACKNOWLEDGMENTS

It is an amazing journey pursuing the Ph.D., and it would not have been possible without the guidance, the help, and the support of several individuals.

I would like to express my utmost gratitude to my advisor, Professor Daniel van der Weide, whose sincerity and inspiration I will never forget. Professor Daniel van der Weide has been guiding and encouraging me as I hurdle all the obstacles in the completion of my research work. I am indebted to Professor Dharmaraj Veeramani and Alfonso Gutierrez for providing great opportunities and supports in a number of ways. I owe my deepest gratitude to Professors Dharmaraj Veeramani, John Booske, Akbar Sayeed, and Nader Behdad of University of Wisconsin-Madison as the members of my committee for their remarks on this thesis and numerous valuable counsels.

I am so grateful to Atul Bhadkamkar, Sangchul Bae, Yue Weng Mak, and Tzu-Han Chou who had been collaborating with me closely for a lot of lab work and discussions helping me broaden my views of various research topics. Special thanks to Atul Bhadkamkar who helps me and gives his best suggestions to me all the time. It would have been a lonely lab without these guys. I would like to thank the graduate students in the vdW groups: Feng-Yu Chang, Matthew Dwyer, Chiya Saeidi, Pushkar Kulkarni, Marcos Martinez, and Jonathan Rodriguez. They always provide constructive feedback to me, and I had a pretty good time with each of them.

Last but not the least, I would like to dedicate this thesis to my family: Ho-Si Chen, Yu-Chin Lin, Huan-Yu Chen, Yu-Hsuan Chang and Wei-Jie Chen in the most sincere thanks for their love, support, encouragement, understanding, and patience.

TABLE OF CONTENTS

LIST OF FIGURES iv

LIST OF TABLES ix

ABSTRACT x

Chapter 1 Introduction 1

1.1 Overview of RFID Sensing 1

1.2 RFID Fundamentals 4

1.2.1 Active / Semi-passive / Passive 5

1.2.2 LF / HF / UHF / microwave 6

1.3 Backscattered Radar Cross Section of a Loaded Antenna 8

1.4 Outline and Contribution 13

Chapter 2 Piggyback Modulation for RFID Sensing 15

2.1 Concept and Design Scheme 15

2.2 Passive UHF RFID Tag 22

2.3 RFID Sensing by Active Sensor Signal 26

2.3.1 Active Sensor Coupling Module 26

2.3.2 Measurement Results 33

2.3.3 Analysis of Demodulation Schemes 42

2.4 RFID Sensing by Passive Sensor Loads 50

2.4.1 Passive Sensor Coupling Module (PSCM) 51

2.4.2 Measurement Results 54

Chapter 3 Vector Backscattering from Planar Dipole Antenna with Complex Loads 58

3.1 Introduction 58

3.2 Vector Backscattering Model 60

3.2.1 Backscattered Electric Field 61

3.2.2 Backscattered Voltage Signal 63
3.3 Planar Dipole Antenna 65
3.4 Loads under Test 71
3.5 Simulation Results 73
3.5.1 Polarization and Orientation Effects 82
3.5.2 Environmental Effect 88
3.6 Experiment Results 95
Chapter 4 Wireless Impedance Measurement by Vector Backscattering 100
4.1 Introduction 100
4.2 Wireless Impedance Measurement Model 102
4.3 Loaded Planar Dipole Antenna 107
4.3.1 Experiment Setup 107
4.3.2 Characterization of Structure Mode Vector 108
4.3.3 Experiment Results 109
4.4 Passive UHF RFID Tag 117
4.4.1 Experiment Setup 118
4.4.2 Experiment Results 120
Chapter 5 Conclusion and Future Directions 123
REFERENCES 125

LIST OF FIGURES

Figure 1.1. The operations for passive, semi-passive, and active tags [19]. 5
Figure 1.2. RFID frequency bands. 7
Figure 1.3. The expression of the scattered field of a loaded antenna. 11
Figure 2.1. The piggyback modulation scheme. 15
Figure 2.2. Equivalent circuit model of the tag and the sensor coupling module with voltage signal from sensors. 18
Figure 2.3. Simplified block diagram of an UHF RFID reader. 21
Figure 2.4. The block diagram of a passive UHF RFID tag. 22
Figure 2.5. The balanced-mode measurement of the input impedance [Ω] of the tag ASIC, Z_{ASIC}, versus frequency ranged from 860 MHz to 960 MHz; the red line is for the real part of Z_{ASIC} and the blue line is the imaginary part of Z_{ASIC}. 24
Figure 2.6. The layout of the tag, AD-222; the ASIC is located in the center. 25
Figure 2.7. The balanced-mode measurement of the input impedance [Ω] of the tag antenna, Z_A, versus frequency ranged from 860 MHz to 960 MHz; the red line is for the real part of Z_A and the blue line is the imaginary part of Z_A. 25
Figure 2.8. Sensor coupling module: one coupling loop and one PIN diode modulator. 26
Figure 2.9. Coupling design consists of coupling loop (red) and commercial UHF RFID passive tag, AD-222 (yellow). 27
Figure 2.10. PIN diode modulator equivalent circuit. 27
Figure 2.11. The input impedance of the PIN diode modulator, Z_{PM}, versus input voltage, V_S. 28
Figure 2.12. (a) Coupling design consists of coupling loop (red) and commercial UHF RFID passive tag, AD-222 (yellow). (b) RFID sensor prototype is comprised of AD-222 and the fabricated sensor coupling module; the emulated sensor signal is fed through the SMA connector. 29
Figure 2.13. Binary signal waveforms of the ASIC data stream and the sensor data stream, and the corresponding four symbols of the combination. 30
Figure 2.14. Graphical representation of backscattering of loaded tag antenna with four different states on Smith Chart. 31

Figure 2.15. The illustration of the vector backscattered signals without piggyback modulation: {$\boldsymbol{V_0}$, $\boldsymbol{V_1}$} and the vector backscattered signals with piggyback modulation: {$\boldsymbol{V_{S1[00]}}$, $\boldsymbol{V_{S2[01]}}$, $\boldsymbol{V_{S3[10]}}$, $\boldsymbol{V_{S4[11]}}$} on the I-Q plane. 32
Figure 2.16. RCS variation with V_S from 0 to 800 mV. 33
Figure 2.17. Experimental setup for real-time backscattered signal measurement..... 34
Figure 2.18. Real-time signal measurement (a) without digital piggyback modulation; (b) with digital piggyback modulation. 35
Figure 2.19. Real-time piggybacking signal measurements at f_C = 915 MHz; V_S is a 5 kHz sawtooth waveform from 0 mV to 800 mV..... 35
Figure 2.20. The transfer function measurement at f_C = 915 MHz: received power of real-time backscattered signal (blue), static RCS with V_S from 0 to 800 mV..... 36
Figure 2.21. Schematic diagram of the measurement setup. 37
Figure 2.22. Time-domain measurements of the vector backscattered signals with piggyback modulation in (a) Amplitude and (b) constellation diagram. (V_S: 5 kHz square wave between 0 and 800 mV; RF output power: +15.0 dBm)..... 39
Figure 2.23. Two trajectories start from S1[00] and S2[01] to S3[10] and S4[11]. (VS: sawtooth wave ramping upward from 0 to 800 mV with an interval of 50 mV; RF output power: +15.0 dBm)..... 40
Figure 2.24. The constellation diagram of the received vector signals of the tag and the sensor prototype. (V_S: 5 kHz square wave between 0 and 800 mV; RF output power: +15.0 dBm, +17.5 dBm, and +20.0 dBm). 41
Figure 2.25. Read rate versus amplitude and frequency of the voltage source from digital piggybacking signal. 43
Figure 2.26. The four-level ASK demodulation. 45
Figure 2.27. Quasi-4-QAM demodulation. 45
Figure 2.28. Monte-Carlo simulation of BER versus SNR for the measured vector backscattered signals of a tag and a sensor prototype. The bit rate ratio of the ASIC signal and the sensor signal is 5. (a) RF output power: +15.0 dBm. (b) RF output power: +17.5 dBm. (c) RF output power: +20.0 dBm. 48
Figure 2.29. Operation of passive sensor coupling and the equivalent circuit model for the RFID passive sensor prototype. 51

Figure 2.30. Conceptual illustration of the vector backscattered signals without passive sensor coupling: $\{V_0, V_1\}$ and the vector backscattered signals with passive sensor coupling: $\{V_{S1}, V_{S2}, V_{S3}, V_{S4}, V_{S5}, V_{S6}\}$ on the I-Q plane. 53
Figure 2.31. Conceptual illustration the one-to-one mapping for the backscattering vectors and corresponding impedances on the I-Q plane when Z_{ASIC} holds constant. Blue dash lines represent for the constant resistive loads; red dot lines represent for the constant reactive loads. 54
Figure 2.32. Measurement of vector backscattered signals from the tag coupled to various loads, each load composed of one resistive and one reactive component in series. The blue dash lines represent the constant resistive; the red dot lines represent the constant reactive loads. 56
Figure 3.1. Backscattering of (a) a scatterer (b) a loaded scattering antenna. 60
Figure 3.2. UHF RFID tag antenna designs: (a) Alien Technology (using tip loading, meandered lines, and additional inductor portions), (b) Symbol Technology (using dual dipoles), and (c) Texas Instruments (using tip-loading and additional inductor portions) [19]. 67
Figure 3.3. UHF planar dipole antenna. 68
Figure 3.4. Simulation result of the input impedance of the planar dipole antenna. 69
Figure 3.5. Simulation result of the structural mode vector, A_S. Frequency: 800 – 1200 MHz. 70
Figure 3.6. Simulation of the vector backscattering model for a planar dipole antenna with polarization-matching and front-facing incidence 74
Figure 3.7. The far-field simulation error of the backscattered electric field of the scattering antenna loaded with Z_{LR}; (a) Amplitude: $AERR_S$ (b) Phase: PER_S. 77
Figure 3.8. The far-field simulation error of the backscattered electric field of the scattering antenna loaded with Z_{LC}; (a) Amplitude: $AERR_S$ (b) Phase: PER_S. 78
Figure 3.9. The non-far-field simulation error of the backscattered electric field of the scattering antenna loaded with Z_{LR}; (a) Amplitude: $AERR_S$ (b) Phase: PER_S. 79
Figure 3.10. The non-far-field simulation error of the backscattered electric field of the scattering antenna loaded with Z_{LC}; (a) Amplitude: $AERR_S$ (b) Phase: PER_S. 80

Figure 3.11. The model-predicted results and simulation results of the vector backscattering of a dipole antenna with different tilted angles. 84
Figure 3.12. The field pattern of the dipole antenna. 86
Figure 3.13. The model-predicted results and simulation results of the vector backscattering of a dipole antenna with different angles. 87
Figure 3.14. Simulation setting of the vector backscattering model for a planar dipole antenna with the presence of an object, a square sheet. 90
Figure 3.15. Simulation results for the antenna characterization parameters under the environmental effects; the range of the dielectric constants: [1, 2, 3, 4, 5, 20, 40, 60, 80]. (a) Z_A (b) A_S (c) gain. 92
Figure 3.16. Experiment setup for the backscattered voltage signal measurement of the loaded planar dipole antenna in an anechoic chamber. 95
Figure 3.17. The experiment error of the backscattered electric field of the scattering antenna loaded with Z_{LR}; (a) Amplitude: $AERR_E$ (b) Phase: PER_E. 97
Figure 3.18. The experiment error of the backscattered electric field of the scattering antenna loaded with Z_{LC}; (a) Amplitude: $AERR_E$ (b) Phase: PER_E. 98
Figure 4.1. Experiment setup for the backscattered voltage signal measurement of the loaded planar dipole antenna in an anechoic chamber. 108
Figure 4.2. The structure mode vector A_S for frequency = 800, 900, 1000, 1100, and 1200 MHz. (Black: simulation; color: measurement). 109
Figure 4.3. (a) The modified reflection coefficient Γ_m for five Z_{LR} for 800 MHz – 1200 MHz. (b) The absolute value of the modified reflection coefficient error $|\Delta\Gamma_m|$ for 800 MHz – 1200 MHz. 110
Figure 4.4. (a) The measured impedances of five Z_{LR} for 800 MHz – 1200 MHz. (b) The average error of measured impedances of five Z_{LR} through five frequencies. 112
Figure 4.5. (a) The modified reflection coefficient Γ_m for five Z_{LC} at 1000 MHz. (b) The absolute value of the modified reflection coefficient error $|\Delta\Gamma_m|$ for five Z_{LC} at 1000 MHz. 114
Figure 4.6. (a) The measured impedances of five Z_{LC} at 1000 MHz. (b) The error of measured impedances of five Z_{LC}. 115
Figure 4.7. UHF RFID passive tag under test: AD-222 (loaded with Monza2 chip). 119

Figure 4.8. Experiment setup for the backscattering measurement of AD-222. 119
Figure 4.9. The structure mode vector A_S and the modified reflection coefficients of open load, short load, and the tag chip in two states (ASIC1 and ASIC2) on the Γ_m– plane. 120
Figure 4.10. The measurement of the tag chip in absorbing state (Z_{ASIC1}) and the reflecting state (Z_{ASIC2}) at 915 MHz. 121

LIST OF TABLES

Table 2-1. Resistive and reactance Loads 57
Table 3-1. Planar dipole antenna layout parameters. 69
Table 3-2. Planar dipole antenna characterization parameters. 70
Table 3-3. Resistive loads under test. 71
Table 3-4. Modified reflection coefficient of resistive loads under test. 71
Table 3-5. Complex loads under test. 72
Table 3-6. Impedance (Ω) of complex loads under test. 72
Table 3-7. Modified reflection coefficient of complex loads under test. 72
Table 3-8. Simulation settings for the vector backscattering model with polarization-matching and front-facing incidence. 75
Table 3-9. Averaged $AERR_S$ and PER_S for far-field and non-far-field simulations 81
Table 3-10. Simulation settings for the vector backscattering model for polarization effect. 83
Table 3-11. Simulation settings for the vector backscattering model for orientation effect. 85
Table 3-12. Dielectric constants for common materials at room temperature and 915 MHz [65] 89
Table 3-13. Simulation settings for the vector backscattering model for environmental effects 90
Table 3-14. Averaged $AERR_S$ and PER_S under the environmental effect. 93

ABSTRACT

Radio Frequency Identification (RFID) with high data capacity, long read range, high security, and multiple tag readings is being widely deployed. Emerging applications include RFID sensing, which is implemented by the integration of sensors and RFID tags. A RFID sensor not only presents the identification of each node, but also provides information such as temperature, humidity, vibration, or timing. It is a candidate for constructing a wireless sensing network for environmental monitoring, vehicle detection, automation, and so on. Existing RFID sensors are bulky, expensive, and less compatible with current standards. In addition, the application-specific integrated circuit (ASIC) of the tag needs to be customized for integrating different types of sensors. By contrast, the piggyback modulation method, which integrates sensor data into existing commercial passive UHF RFID tag, is presented to provide a solution for RFID sensors featuring compact size, low cost, simplicity, and high compatibility. This technique can be applied to both active and passive sensors. Furthermore, the proposed vector backscattering model of a scattering antenna with a complex impedance load is analyzed and fully described by closed-form model equations. The wireless impedance measurement by vector backscattering is presented; this method is applicable to planar dipole antennas and standard passive UHF RFID tags.

Chapter 1 Introduction

1.1 Overview of RFID Sensing

Radio-frequency identification (RFID) is one wireless communication technology that is primarily used for identification and data access in a very simple and economical fashion. This technology has been studied and developed for more than half of century and its exclusive attributes, like simplicity, compactness, low price, and robustness, make it distinctively outstanding among present wireless communication technologies and ubiquitous through numerous applications in our daily lives.

In a RFID system, each tag, also known as electronic label and transponder, has its unique identification number which is stored, modified, and transmitted back to a reader in kilohertz, megahertz or gigahertz ranges. The RFID technology, which allows the contactless data transmission via electromagnetic waves, is used to identify items like what the barcode technology does. Having larger data storage, longer read range, and the immunity of the line-of-sight requirement makes RFID superior to barcodes in various aspects. RFID has been widely applied in diverse fields, such as supply chain and inventory management, access and control, healthcare, and real time location tracking (RTLS) [1].

Recently, one of the most appealing RFID emerging applications is RFID sensing [2–5], which combines sensor functions with RFID systems to construct a wireless sensing network. By definition, wireless sensing network (WSN) is a network of spatially distributed autonomous sensors cooperatively monitoring physical or environmental conditions, such as temperature, vibration, pressure, pollutants, or motion. A wide variety of applications as listed below, [6]

- Health Care Monitoring
- Military Surveillance and Tracking
- Industrial Process Monitoring and Control
- Smart Home
- Environmental and Ecological Habitat Monitoring

The integrations of sensors and RFID systems are categorized into groups based on the integration level. In this thesis, we mainly focus on the integration of RFID tags and sensors. An RFID sensor not only offers the identification of each node, but also provides sensing information. Active tags are used in the majority of the solutions nowadays for RFID sensors. Most of them are able to send signals actively for more than tens of meters, and are embedded with powerful computing capability, sophisticate functions, and on-board power source. However, active RFID sensors are relatively bulky, expensive, and complicated compared with passive and semi-passive ones. They also have low compatibility with other systems because they lack a standard protocol. On the other hand, item-level sensing is not practical for some applications in which the value of the objects under monitoring is lower than the active RFID sensors.

A number of applications, including cool chain logistics, healthcare, or "smart home", demand item-level wireless sensing capabilities with compact size, adequate accuracy, relatively low price, and compatibility with existing standards. For example, the solution of item-level RFID temperature sensing is very appealing to the logistics management and quality control for cold chain supply systems which include the transportation of perishable foods, like fruits, vegetables, dairy products, and meats, and biomedical transportation for blood transfusion, organ transplantation, biochemical samples, and pharmaceuticals. The wireless vibration sensing is also desired for the transportation of fragile and delicate goods. For the healthcare markets, wireless sensing has huge potentials for periodically monitoring each patient's temperature, blood glucose levels, and blood pressure. This technology can also facilitate "Smart Home," the integration of residences' various home automation systems, like water and heating leakage detection, security motion detection, and so on.

Passive RFID sensors were presented in [7–10], but few of these solutions can match all the needs. To fill this niche, we propose the design of self-powered RFID sensor, the integration of sensing functions and printed battery with commercial UHF RFID passive tag, which has no built-in energy source, acquires power wirelessly, and utilizes the backscattering manipulation for communications [11], [12]. The most essential portion of this design is the "piggybacking" technique and its modulation scheme which provide a solution for simple, small, inexpensive RFID sensors with high compatibility with most of existing UHF RFID passive tags. Rather than

directly integrating sensing functions into the ASIC of tags in circuit-level, the piggyback modulation design overlays an additional sensing signal through the well-established communication channel between readers and tags. In other words, this technique can be applied to generic sensors [13–17].

Although the piggyback modulation technique is not only valid for UHF RFID passive tags, choosing this specific category for sensing function integration brings superior benefits as compared with other RFID tags. UHF RFID tags have longer read range, higher read rate, and wider bandwidth than LF and HF ones. Also, UHF RFID passive tags have a broadly accepted standard, like EPC Global Gen2 [18] and ISO/IEC 18000 while there are few well-accepted standards for microwave RFID actives tags. Passive tags are always more cost-efficient than active ones for the price is one of the primary concerns.

1.2 RFID Fundamentals

Radio-frequency identification (RFID) is designed mainly for reading and writing identification of an object via wireless data transmissions. RFID technology is a very general term which covers a wide range of technologies and it is categorized into several subgroups depending on frequency, power supply, and protocol and so on.

The key character that differentiates RFID technology from most of other wireless communication schemes is the choice of utilizing the mechanism of the modulated backscattering. Scattering is a physical process in which a trajectory of wave propagation is deviated to an arbitrary direction when the wave encounters an object with a medium discontinuity; backscattering is the special case of scattering when waves are reflected back to where the wave is generated.

This idea was originated from the need to identify hostile aircraft detected by microwave radar during World War II. Radar was able to detect an object appearance only, but not to identify it. The radar station could separate friends and foes only if the scattering object, the aircraft, could alter its status by changing the backscattered signal. At that time, the pilots rolled in a pattern to vary the signals backscattered by their plane and then couples of simple bits were sent back to the radar station so that the pilots can identify themselves [19].

A typical RFID system contains readers and tags, also known as interrogators and transponders. A reader builds up communications with multiple tags and access to (read/write) their identifications in time-division multiplexing. Each tag has its own unique identification number for differentiating itself from the others. Most of tags are comprised of application-specific integrated circuit (ASIC) and tag antenna. A tag ASIC is also called a tag chip and it can do power conversion, modulation/demodulation, coding/decoding, and data storage while tag antenna efficiently transduce electromagnetic field or radiation into electric current and vice versa at one specific frequency band.

Today, RFID technology using the similar concept is far cheaper, more powerful, and more compact due to the development of integrated logic. Communication between the reader and a passive tag is established as follows. First, the reader sends out signals into the air. The

passive tag is awakened by impinging RF power from the reader and demodulates signals to the logic circuit. The logic IC then uses binary information to modulate the backscattered signals received by the reader.

1.2.1 Active / Semi-passive / Passive

Based on how the RFID tags are powered up, there are three types of RFID tags: passive tags, semi-passive/semi-active tags, and active tags. At the tag side, two power consumptions are needed for signal transmission through air and the operation of the ASIC in every communication between reader and tag. What the power sources are for each of these two power consumptions determine which type of the tag is.

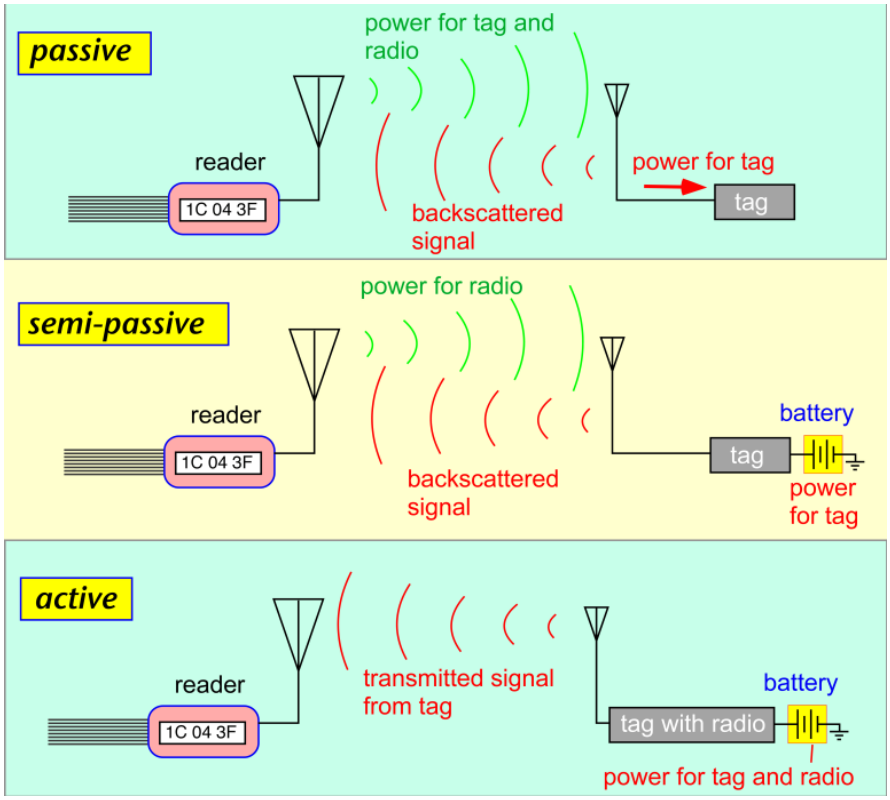

Figure 1.1. The operations for passive, semi-passive, and active tags [19].

No on-board power source is needed for passive tags and all of the required power is provided external electromagnetic field or impinging electromagnetic wave generated by a reader. For most of the time, passive tags in the sleep mode do nothing until they are awaked by harvesting powers through electromagnetic induction or capturing incoming electromagnetic wave from a reader. Once the ASIC of a tag is powered up, it starts processing the request signal from the reader and reacts to the request by sending its identification back to the reader through the modulation of the adjacent electromagnetic field or the backscattered electromagnetic wave.

For semi-passive/semi-active tags, one on-board power source supports only the power needed for the operation of the ASIC. Since the ASIC reap no power externally, more power can be manipulated for the backscattering modulation so that the longer read range and shorter reading time are achievable.

Active tags also have an on-board power source which takes care of all the required powers. Rather than doing any modulation on the backscattered electromagnetic wave, one active tag has its own transmitter which makes it possible to communicate with a reader actively with a longer distance and faster reading speed.

The communication launched by a reader through sending requests is so-called reader-talk-first; both passive tags and semi-passive/semi-active tags are in this category. If tags, like active ones, are able to send signals to readers actively without being awaked at all, this is the tag-talk-first communication.

1.2.2 LF / HF / UHF / microwave

Besides the issues of power supplies, the operation frequency band is another key parameter to set the boundaries from one RFID system to others. The mechanism of the interaction between readers and tags, the antenna size, the read range, the data throughput, the standards, and the regulations are all highly determined by which frequency band one RFID system operates.

Based on the International Telecommunication Union (ITU) radio regulation, the radio spectrum is subdivided into several frequency bands with designated names. Most common used

RFID frequency bands are located in Low Frequency (LF, 30 ~ 300 kHz), High Frequency (HF, 3 ~ 30 MHz), Ultra High Frequency (UHF, 300 MHz ~ 3 GHz), and Microwave (300 MHz~ 300 GHz).

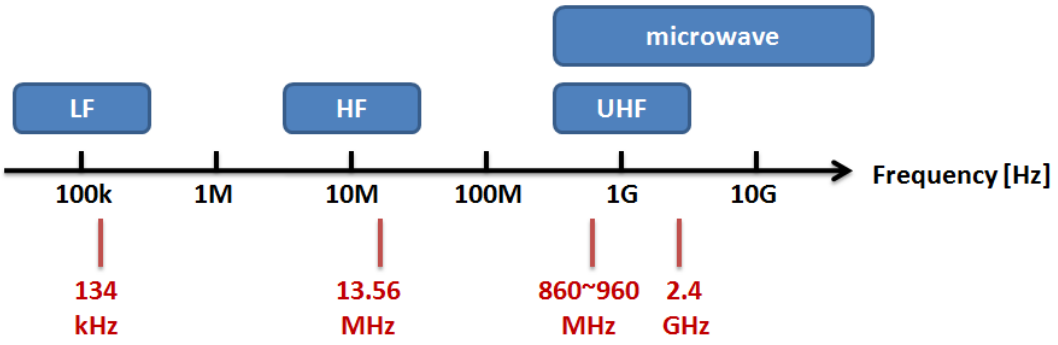

Figure 1.2. RFID frequency bands.

The operation frequency for a LF RFID system is 124 kHz or 134 kHz while a HF RFID system operates around 13.56 MHz. Because of relatively narrow bandwidths, both LF and HF RFID systems have a lower data transfer rate. Another shared characteristic for these two is short read range due to the use of electromagnetic induction which highly constrains the energy flow in the adjacent space. However, tags operating in LF and HF bands have higher immunity from the presences of metals and liquids.

A frequency band ranged from 860 MHz to 960 MHz is utilized by typical UHF RFID systems. The wider bandwidth makes UHF RFID provide a higher read rate. The connection between UHF RFID readers and tags is built by electromagnetic radiation and this mechanism increases the read range up to tens of meters. Even though UHF frequency band is also covered by microwave band, UHF RFID is well accepted for 860 MHz to 960 MHz band and normally microwave RFID systems are refer to those operating at 2.4 GHz or 5.8 GHz. Pursuing higher frequency band offers key benefits, such as larger data throughput, faster read speed, longer read range, and more compact tag size while the prices are the increases of cost and complexity [20–26].

1.3 Backscattered Radar Cross Section of a Loaded Antenna

In the section, the review of the studies for the scattering properties of a loaded antenna is provided as a supplement to the theoretical analysis of my work. First of all, the concepts of the scattering and the radar cross section (RCS) are introduced, and the challenge of solving the scattering problem of a loaded antenna is addressed. Then, the development of the equation for the scattered power of an antenna as a function of the load impedance is presented. This equation is able to determine the scattering from a loaded antenna when the specified antenna parameters are characterized.

Scattering is a physical process in which a trajectory of wave propagation is deviated to an arbitrary direction when the wave encounters an object with a medium discontinuity. The radar cross section (RCS), σ, characterizes the scattering property of a scatterer in the far field and it is defined as the area intercepting that amount of power which, when scattered isotropically, produces at the receiver a density which is equal to that scattered by the actual target [27]. Backscattering is the special case of scattering for a radar system in which transmitter and receiver are collocated. Backscattering RCS, σ_{BS}, is a function of the incident field, and the backscattered field as follows,

$$\sigma_{BS} = \lim_{R\to\infty} 4\pi R^2 \frac{W_{BS}}{W_{INC}} = \lim_{R\to\infty} 4\pi R^2 \frac{\left|\overrightarrow{E_{BS}}\right|^2}{\left|\overrightarrow{E_{INC}}\right|^2} \tag{1.1}$$

where W_{INC} is the incident power density at the target and W_{BS} is the backscattered power density at the observation point (or the receiving antenna); E_{INC} is the incident electric field at the target and E_{BS} is the backscattered electric field at the observation point. The distance between the target and the observation point, R, approaches infinity to fulfill the far-field conditions. In the far-field region, E_{BS} is inversely proportional to the distance between the target and the observation point; therefore, σ_{BS} is independent of R.

The scattering of an antenna are dependent on the load impedance at the antenna terminal, and researches have been conducted to provide solutions relating the scattered field and the load impedance of the antenna. Theoretically, the scattered field of a loaded antenna can be analyzed by applying the Maxwell equations and boundary conditions. However, this approach which needs to be repeated for every different antenna is quite challenging for practical cases, since it does not provide a general relation between the scattering and the load impedance of the antenna. The complex boundary-value problem can be simplified by introducing the equivalent circuit model or the scattering matrix model which is similar to the treatment used for transmission lines.

To describe the scattered field of a loaded antenna, the Thevenin equivalent circuit was proposed to model the incident field, the scattering antenna, and the load in a series circuit. The scattered (reradiated) power is expressed in terms of the dissipated power in the antenna resistance. The scattered power is obtained based on the circuit rules. With the scattered power calculated from the Thevenin equivalent circuit model, σ_{BS} of the loaded antenna with polarization-matching is derived in [28–30] as,

$$\sigma_{BS} = \frac{\lambda^2}{4\pi} G_{SA}{}^2 \left|1-\Gamma_m\right| \tag{1.2}$$

where λ is the wavelength, G_{SA} is the scattering antenna gain, and the modified reflection coefficient is defined as

$$\Gamma_m = \frac{Z_L - Z_A^*}{Z_L + Z_A} \tag{1.3}$$

in which Z_L is the load impedance of the scattering antenna and Z_A is the input impedance of the scattering antenna. According to (1.2), σ_{BS} of an open-loaded antenna is supposed to be zero but

actually it is not true for all the cases. Therefore, the scattering property of a loaded antenna cannot be predicted by (1.2).

The scattering matrix representation of a loaded antenna was presented and the expression of the scattered field was derived by Collin [29]. The scattered field is a function of the load impedance and it is given by

$$\overrightarrow{E_S}(Z_L) = \overrightarrow{E_S}(Z_L = 0) - \frac{Z_L}{Z_A + Z_L} \cdot I(Z_L = 0) \cdot \overrightarrow{E_r} \tag{1.4}$$

where

$\overrightarrow{E_S}(Z_L)$ [V/m]: the scattered field when the antenna is terminated in Z_L,

$\overrightarrow{E_S}(Z_L = 0)$ [V/m]: the scattered field when the antenna is terminated in a short circuit,

$I(Z_L = 0)$ [Amp]: the current at the antenna terminal when the antenna is terminated in a short circuit,

$\overrightarrow{E_r}$ [V/m-Amp]: the radiated field with an unit excitation current at the antenna terminal

; this equation was adopted by Hansen [30], Green [31], and Knott [32].

The first term of (1.4) represents a scattered field raised from a short-loaded antenna which is totally load independent since a short-loaded dipole antenna is merely a metallic rod. The second term of (1.4) is a current-driven radiation field and it is determined by the load impedance. Therefore, the first term is called the structure mode and the second term is called the antenna mode, as shown in Figure 1.1.

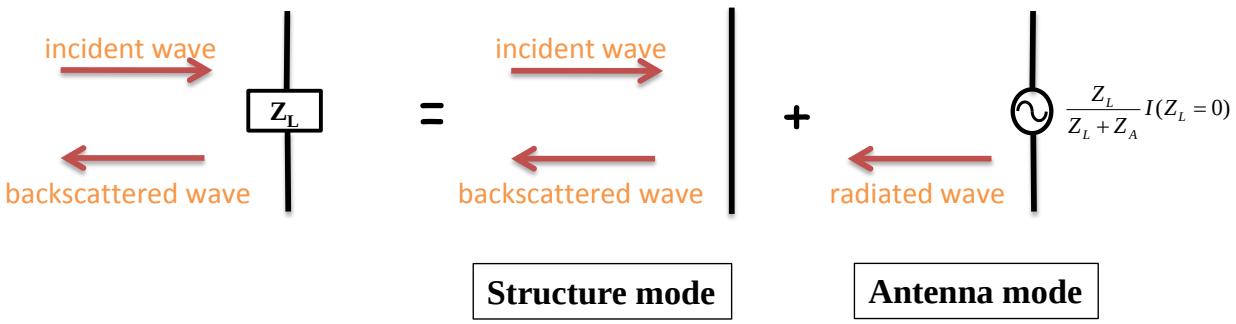

Figure 1.3. The expression of the scattered field of a loaded antenna.

Although, in (1.4), a short circuit is chosen to be the reference load impedance for carrying the physical insight of the structure mode when the first term of (1.4) represents the scattered field from antenna with no load impedance involved, the reference load impedance can be chosen for arbitrary value. To exploit (1.4) further, the reference load impedance is chosen to be the complex conjugate of the input impedance of the antenna and this equation is rewritten by Green as [31]

$$\overrightarrow{E_S}(Z_L) = \overrightarrow{E_S}(Z_L = Z_A^*) + (-\frac{Z_L - Z_A^*}{Z_L + Z_A}) \cdot I(Z_L = Z_A^*) \cdot \overrightarrow{E_r} \tag{1.5}$$

In (1.5), the scattered field is still a function of the load impedance and is composed by two parts: the structure mode and the antenna mode. The first term is a scattered field raised from a conjugate matched antenna and the second one is a current-driven radiation field. The structure mode and the antenna mode vary when the different reference load impedances are applied. And then, the equation (1.5) is rearranged as,

$$\begin{aligned} \overrightarrow{E_S}(Z_L) &= I(Z_L = Z_A^*) \cdot \overrightarrow{E_r} \cdot [\frac{\overrightarrow{E_S}(Z_L = Z_A^*)}{I(Z_L = Z_A^*) \cdot \overrightarrow{E_r}} - \frac{Z_L - Z_A^*}{Z_L + Z_A}] \\ &= I(Z_L = Z_A^*) \cdot \overrightarrow{E_r} \cdot [A_S - \Gamma_m] \end{aligned} \tag{1.6}$$

where the structure mode is represented by A_S which is the structure mode vector (a load-independent complex parameter) and it is dependent on the geometry and material of the antenna; the antenna mode is represented by Γ_m which is the modified reflection coefficient defined in (1.3) and is a function of both the input impedance of the antenna and the load impedance.

Actually, the conjugate matched load is intentionally chosen by Green [31] because the equation of the backscattering RCS, σ_{BS}, of a loaded scattering antenna with polarization-matching can be derived by substituting (1.6) into from (1.1) as

$$\sigma_{BS} = \frac{\lambda^2}{4\pi} G_{SA}{}^2 \left| A_S - \Gamma_m \right|^2 \tag{1.7}$$

which is useful since it can be interpreted geometrically in the format of Smith Chart. In other words, with the antenna characterization parameters (G_{SA}, A_S, and Z_A) and a given direction, polarization, and frequency, the backscattered power is determined by the load impedance. The method for antenna parameter characterization is presented in [33], [34].

Equation (1.7) was verified by Green with the numerical results of a thin cylindrical antenna [31], [35], and by the author with the simulation results of a planar dipole antenna, as shown in the next section. Knott pointed out that this equation may be the first widely distributed RCS equation and the most used definition of the structure mode and the antenna mode [27], [32–34].

1.4 Outline and Contribution

In this section, the content in the subsequent chapters is outlined to provide a glimpse of the main contributions in this thesis.

- Chapter 2: Piggyback Modulation for RFID Sensing

  In this chapter, we introduce the technique of "piggybacking" sensor data onto existing commercial passive UHF RFID tags. Sensor data fed into a PIN diode modulator is coupled onto the tag and transmitted along with the tag ID via backscattering. The radar cross section (RCS) of the tag antenna is a function of the input impedance of the tag ASIC, coupling S-parameters, and the input impedance of the PIN diode modulator. Then, we expand this technique and exploit the vector backscattered signal with piggyback modulation. Measuring both amplitude and phase of the backscattered wave makes advanced demodulation possible. The measurement setup, experimental results, demodulation analysis, and numerical simulation for the conventional amplitude-shift keying (ASK) and quasi-4-quadrature amplitude modulation (quasi-4-QAM) are presented. Quasi-4-QAM demodulation reduces the interference between two independent data streams and improves the bit error rate for the same RF power. Without explicit data from any given sensor, we do show that a generic sensor signal will be improved with our technique.

- Chapter 3: Vector Backscattering from Planar Dipole Antenna with Complex Loads

  As inspired by envisioning the potential vector backscattering in the previous chapter, the vector backscattering model is proposed. A planar dipole antenna is designed as a scattering antenna with resonant frequency located in the UHF band. The three characteristic parameters of the scattering antenna, which are included in these equations, are obtained. The simulated vector backscattered electric fields are presented and compared with the model results as the environmental effect, the oriental effect, and the polarization effect are incorporated. The experiment results of the vector backscattered voltage signal are shown and compared with model outcomes in which the propagation loss factor and the propagation phase shift factor are included.

- Chapter 4: Wireless Impedance Measurement by Vector Backscattering

  The method of wireless impedance measurement by vector backscattering is presented in this chapter. Derived from the equation of the vector backscattering of a loaded scattering antenna, the equation is presented for the link between the ratio of two backscattered voltage signals and the ratio of the corresponding modified reflection coefficients. This equation not only leads to a new and improved process for the characterization of the scattering antenna but also provide an approach of wireless impedance measurement. This method is validated by experimental results of a UHF planar dipole antenna loaded with a number of resistive and complex loads. This method also applies to the passive ultra high frequency (UHF) radio-frequency identification (RFID) tag chips in both the absorbing state (Z_{C1}) and the reflecting state (Z_{C2}). The measurements are performed for the tag chip connected to the tag antenna in the balanced mode as it operates. No test fixture and matching network is needed. The chip impedance measurement in both the absorbing state and the reflecting state is achieved by using the time-domain vector reflectometer system, which is composed of a vector signal generator and a vector signal analyzer. The experimental results are presented for a UHF RFID Gen2 chip (Impinj Monza2).

Finally, in Chapter 5, we summarize our results and suggest some possible directions for this work.

Chapter 2 Piggyback Modulation for RFID Sensing

2.1 Concept and Design Scheme

To provide a solution for simple, small, inexpensive RFID sensors with high compatibility with most of existing UHF RFID passive tags, the piggyback modulation technique is proposed. Most of current RFID sensors are implemented by integrating sensing functions directly into the ASIC of tags; however, the circuit-level integration requires time-consuming and complex IC designs and it also has low compatibility and high price. Instead of being stuck with the troublesome circuit-level integration, we choose to circumvent this difficult situation by providing a novel solution – the piggyback modulation technique.

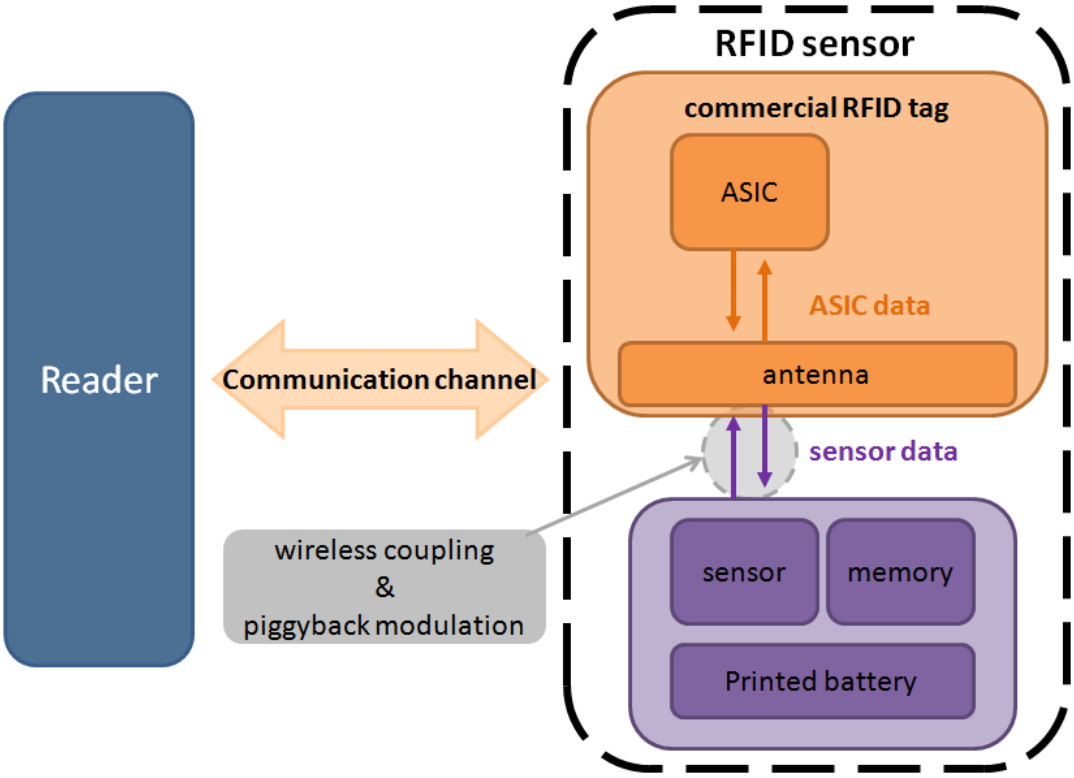

Figure 2.1. The piggyback modulation scheme.

Since RFID communication channels between readers and tags work well, why not use them for transmitting sensing signals along with the existing identification data flow? As mentioned previously, a passive UHF RFID tag transmitting its identification number back to a reader through the modulation of the backscattered electromagnetic wave (or the tag's radar cross-section, RCS). If one passive tag's RCS can be modulated according to the data from sensors with acceptable effects on the identification data stream, both of the ID and sensing information can be sent back to and recognized by a reader with an additional simple demodulation function.

One sensing signal source is able to manipulate the backscattered electromagnetic wave of a passive tag through wireless coupling by simply attaching a sensor coupling module. In other words, two signal sources of the ASIC and the sensor operate independently and simultaneously to modulate the RCS of the combination of a passive tag and a sensor coupling module connected to a sensor. The wireless sensing is realized by piggybacking the data from sensors on top of the identification data stream while no circuit-level integration is needed. This overlaying modulation scheme transmitting two data streams at the same time makes the utilization of the well-established communication channel linking readers to tags more efficient.

The most essential element of the piggyback modulation technique is the sensor coupling module which enables an arbitrary sensing signal source to modulate the backscattered electromagnetic wave through wireless coupling. In this section, we present the equivalent circuit model of the tag and the sensor coupling module and the transfer function of the RFID sensor which has V_S, arbitrary sensor signal, as input and RCS or V_{BS}, backscattered signal strength, as output.

The radar cross-section (RCS) is a far-field parameter for characterizing the scattering property. The backscattered RCS of a UHF RFID passive tag with polarization-matching is formularized as

$$\sigma_{BS} = \frac{\lambda^2}{4\pi} G_{0,tag}{}^2 \left|\Gamma_m - A_S\right|^2 \tag{2.1}$$

where λ is the wavelength, G is the tag antenna gain; A_S, is a load-independent complex parameter representing for the structural mode scattering; Γ_m is the modified reflection coefficient which is determined by tag antenna impedance, Z_A, and the load impedance of the tag antenna, Z_L.

$$\Gamma_m = \frac{Z_L - Z_A^*}{Z_L + Z_A} \tag{2.2}$$

The sensor coupling module is comprised of a coupling loop and a PIN diode modulator. This PIN diode modulator is comprised of a PIN diode, a capacitor, and an inductor. The input impedance of the PIN diode modulator, Z_{PM}, is controlled by a voltage source which could by an arbitrary sensor signal source, V_S.

$$Z_{PM} = \frac{1}{j\omega C} + j\omega L // Z_{PIN}(V_S) \tag{2.3}$$

Attaching the sensor coupling module to a passive tag with a gap provides a link between them through coupling. The equivalent circuit model of the tag and the sensor coupling module with voltage signal from sensors is shown in Figure. 2.2.

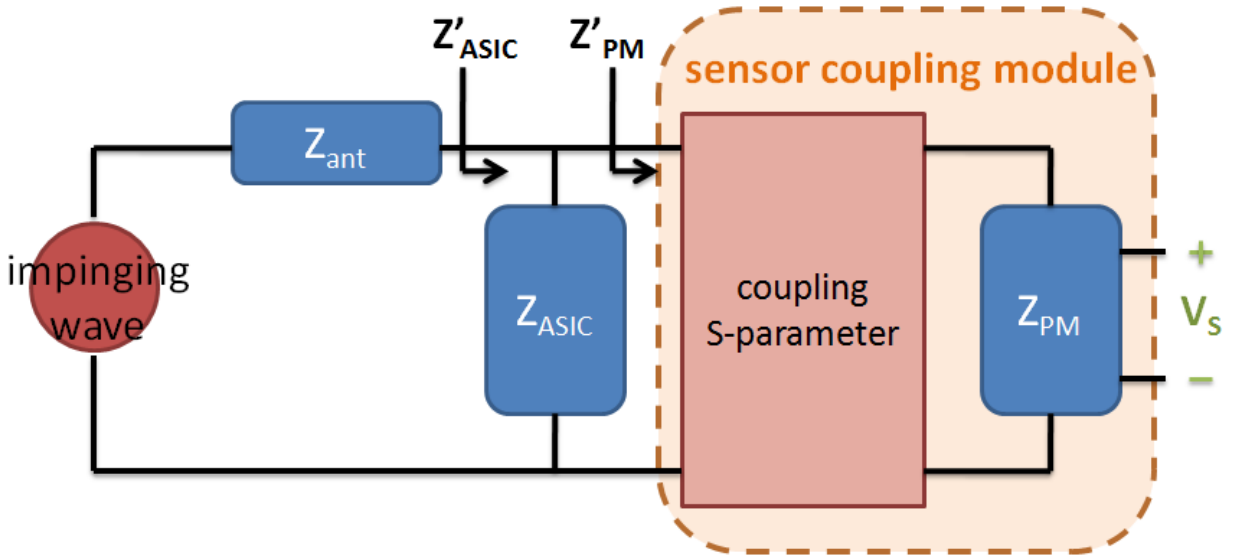

Figure 2.2. Equivalent circuit model of the tag and the sensor coupling module with voltage signal from sensors.

The effective load impedance seen from the tag antenna, Z'_{ASIC}, is modified to be the parallel connection of the tag ASIC and sensor coupling module with input impedance Z'_{PM}.

$$Z'_{ASIC} = Z_{ASIC} // Z'_{PM} \tag{2.4}$$

The coupling mechanism is treated as 2-port network and modeled by a 2-by-2 S-parameter matrix which is a function of the material, the shape, and the gap between the coupling loop and the tag. Z'_{PM} is determined by both of the input impedance of the PIN diode modulator, Z_{PM}, and the coupling S-parameter.

$$Z'_{PM} = Z_0 \frac{1+\Gamma'_{PM}}{1-\Gamma'_{PM}} \tag{2.5}$$

$$\Gamma'_{PM} = S_{11} + \frac{S_{12}S_{21}\Gamma_{PM}}{1 - S_{22}\Gamma_{PM}} \tag{2.6}$$

$$\Gamma_{PM} = \frac{Z_{PM} - Z_0}{Z_{PM} + Z_0} \tag{2.7}$$

Once the effective load impedance seen from the tag antenna, Z'_{ASIC}, is obtained, the modified reflection coefficient, Γ_m, is ready. With the operation wavelength, λ, and the parameters of the tag antenna, including the tag antenna gain, $G_{0,tag}$, and the load-independent structural mode, A_S, we are able to estimate the backscattered RCS of the combination of tag and sensor coupling module.

The backscattered RCS of the combination of tag and sensor coupling module or the V_{BS}, the backscattered signal strength, changes as varying V_S and the transfer function describes what is needed for connecting the input and the output thoroughly. That means anyone who wants to integrate one sensor into a commercial tag only need to know what the transfer function is and does not have to care about these complex equations.

In a backscattering measurement, the transmitting antenna and receiving antenna are at the same location. In our setting, only one antenna is used for both transmitting and receiving signal. The radar range equation [27] describes the ratio of the received power of backscattering and the transmitted power as

$$\frac{P_{r,BS}}{P_t} = \sigma_{BS} \frac{G_{0,reader}^2}{4\pi} \left(\frac{\lambda}{4\pi R^2}\right)^2 \tag{2.8}$$

$$P_{r,BS} = \frac{|V_{BS}|^2}{2Z_0} \tag{2.9}$$

Combining (2.1), (2.2), (2.4), (2.8), and (2.9) leads to

$$|V_{BS}| = \sqrt{2Z_0 \frac{\lambda^4}{(4\pi R)^4} G_{0,tag}^2 G_{0,reader}^2 P_t} \cdot \left| A_S - \frac{Z'_{ASIC}(V_S) - Z_{ant}^*}{Z'_{ASIC}(V_S) + Z_{ant}} \right| \tag{2.10}$$

which is derived from the combination of the radar range equation and the backscattering RCS equation, and links the magnitude of the backscattered signal, $|\boldsymbol{V_{BS}}|$, and the complex input impedance of tag antenna's load, Z_{load}. Since Z_{load} is a function of the sensor signal, V_S, the backscattered signal is manipulated by V_S and that's how the piggyback modulation works. Even though this equation does not explicitly point out the relationship between V_S and $\boldsymbol{V_{BS}}$, it reveals the potential of the vector backscattered signal.

The backscattered RCS is a scalar value of area size as a measure of how detectable of an object and it is proportional to the square of the distance between Γ_m and A_S in the complex plane. Nonetheless, $\boldsymbol{V_{BS}}$ is a vector which contains both amplitude and phase and it is also determined by A_S and Γ. For amplitude-shift keying (ASK) modulation, knowing the scalar RCS values of different Γ is enough. Compared with measuring scalar RCSs for signal detection, having both amplitude and phase of $\boldsymbol{V_{BS}}$ could make the backscattered signal more immune to noise.

The "vector backscattered signal" is used to describe the backscattered signals in both amplitude and phase. For most of the passive tags, either the ASK or the phase shift keying (PSK) is selected to modulate the backscattered wave, since Gen2 standard readers are regulated by the EPCglobal UHF Class-1 Generation-2 air interface protocol to fully perform demodulation for both of these two modulation schemes. To demodulate signals backscattered from tags that adopt ASK/PSK modulation, only the amplitude/phase is detected while the other one is discarded even though both of them are modulated by switching the complex input impedances of the tag ASIC.

As mentioned in the previous chapter, a RFID reader is an important part of a RFID system and it is actually a RF transceiver, which is a combination of a transmitter and a receiver. To communicate with tags, a reader transmits signal and provide power to tags as a transmitter, and then receives signal backscattered from a tag as a receiver. The simplified architecture of a RFID reader is shown in Figure 2.3. An antenna, a circulator, a local oscillator, and a digital processor are shared by the transmitter and the receiver, whereas a power amplifier (PA), a I/Q modulator, and a digital-to-analog converter (DAC) belong to the transmitter and a low noise amplifier (LNA), a I/Q demodulator, and a analog-to- digital converter (ADC) belong to the receiver.

In the UHF RFID protocol, EPCglobal Class-1 Generation-2, the demodulation function of ASK (Amplitude Shift Keying) and PSK (Phase Shift Keying) are required for RFID readers, but complex (amplitude and phase) demodulation, which is essential in the proposed piggyback vector backscattering modulation scheme, is not. Although the complex demodulation is not a mandatory function for a RFID reader in the existing protocol, the I/Q demodulator is commonly included in the block diagram of the UHF RFID reader chip design architecture [36–45]. In addition, commercial UHF RFID readers provide the I/Q demodulation function [46–51] and these readers are ready for the vector backscattering detection. Therefore, the proposed RFID sensor design in which the piggyback vector backscattering modulation is used can be implemented in the existing RFID readers with little additional modification.

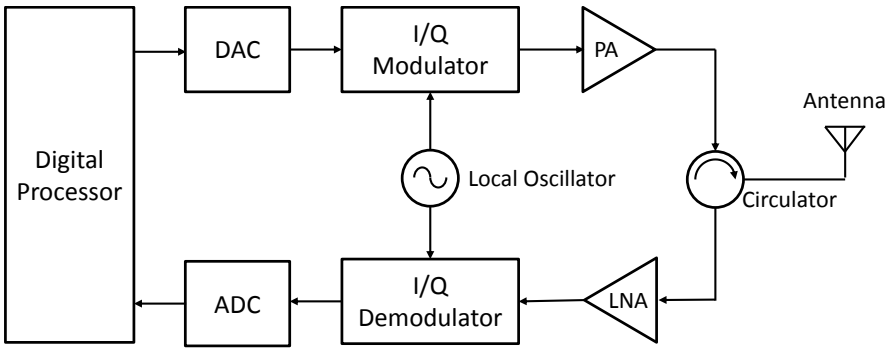

Figure 2.3. Simplified block diagram of an UHF RFID reader.

2.2 Passive UHF RFID Tag

Two main components of one RFID tag are a tag antenna and a tag application-specific integrated circuit (ASIC). Rather than being designed as a general-use integrated circuit (IC), an ASIC is custom-made for particular purposes. The circuit structures and functions of ASICs for passive/semi-passive/active tags differ from one another. To avoid ambiguity, all the "tag ASICs" in the following are referred to the ASICs for UHF RFID passive tags only. The key components in a tag ASIC are RF/DC power converter, downlink signal demodulator, digital logic circuit, uplink signal modulator, and non-volatile memory, as depicted in Figure 2.4.

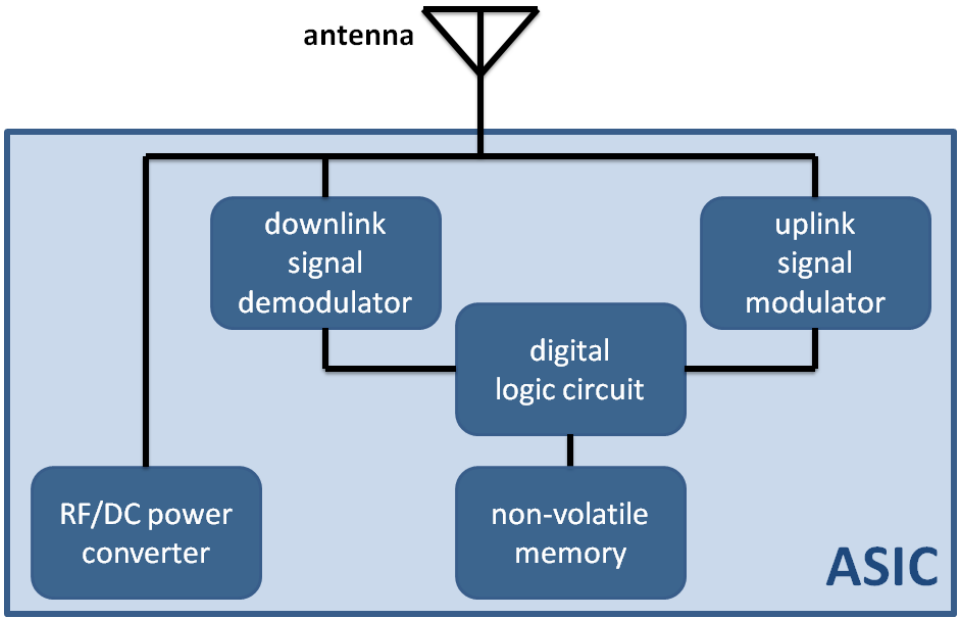

Figure 2.4. The block diagram of a passive UHF RFID tag.

After receiving an impinging RF signal from a reader through a tag antenna, a tag extracts both power and information in its ASIC. A RF/DC power converter, which is composed of a rectifier and a single/multiple stage of charge pump circuit, is needed for providing DC power with an appropriate voltage level from harvested RF power. Meanwhile, the request embedded in the same RF signal has to be recognized via processes of demodulation and decoding; they are conducted in the downlink signal demodulator and the digital logic circuit

individually. As long as the request from a reader is confirmed, an ASIC reacts to it by a series of reactions: access (write/read) to its identification numbers in a non-volatile memory, encode the uplink signals and generate modulating signal to the uplink modulator. The last step for an ASIC to complete one conversation with a reader is the uplink signal modulation that is done by switching the ASIC input impedance between two states in the uplink signal modulator.

To create better quality for backscattering, the ASIC input impedance has two states in terms of having two distinctive complex input impedances. For passive and semi-passive tags, the uplink communication that is from tag to reader is achieved by manipulating the backscattering waves through the forward and backward switching of ASIC input impedance. Depending on the modulation scheme, which could be either amplitude shift keying (ASK) or phase shift keying (PSK), two complex ASIC input impedances are designed correspondingly. Typically, one state is better matched to the input impedance of tag antenna for receiving stronger signal and harvesting more power while the other state provides higher backscattered signal strength by less impedance matching to the tag antenna.

The majority of the tag antennas operate in the balanced mode which is different from the unbalanced mode (single ended mode), like coaxial cables. Therefore, most of the ASICs are operated in the balanced mode, so does the ASIC in this study. Input impedance measurements are commonly done by using a vector network analyzer with coaxial connections in the unbalanced mode. To provide results with higher accuracy, one balanced-unbalanced text fixture is used to implement the balanced measurement. The measurement results for both the real part and the imaginary part of the ASIC input impedance, Z_{ASIC}, versus frequency ranged from 860 to 960 MHz is indicated in Figure 2.5.

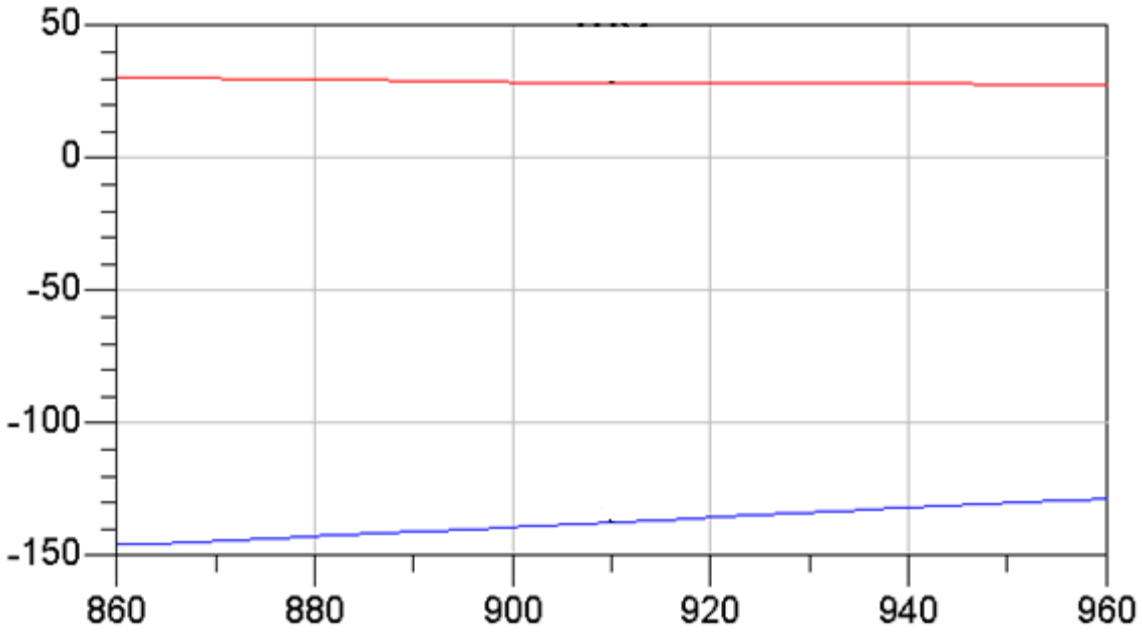

Figure 2.5. The balanced-mode measurement of the input impedance [Ω] of the tag ASIC, Z_{ASIC}, versus frequency ranged from 860 MHz to 960 MHz; the red line is for the real part of Z_{ASIC} and the blue line is the imaginary part of Z_{ASIC}.

A tag antenna, like all the other antennas, is used to transmit and received electromagnetic waves. To be omni-directionally detectable, the directivity of a tag antenna needs to be low; hence the dipole antenna design that has low directivity and low profile is popular. Another key parameter of a tag antenna is the impedance which determines the power transferred to a tag ASIC. Passive tags have tighter power budget and need better impedance matching between tag antennas and ASICs to deliver higher power to ASICs. On the other hand, the radar cross-section (RCS) of a tag is also a function of the load-independent structural mode vector of a tag antenna, A_S, and the gain of a tag antenna, $G_{0,tag}$. In this study, the AD-222 manufactured by Avery Dennison is chosen. The dimension is 94.9 x 7.9 mm^2 and the thickness is 2 mil (51 micron), shown in Figure 2.6.

Like the impedance measurement of an ASIC, we use one balanced-unbalanced text fixture for the measurement in the balanced mode. Figure 2.7 shows the experimental results of the input impedance of the tag antenna at the threshold power versus within the range from 860 to 960 MHz.

Figure 2.6. The layout of the tag, AD-222; the ASIC is located in the center.

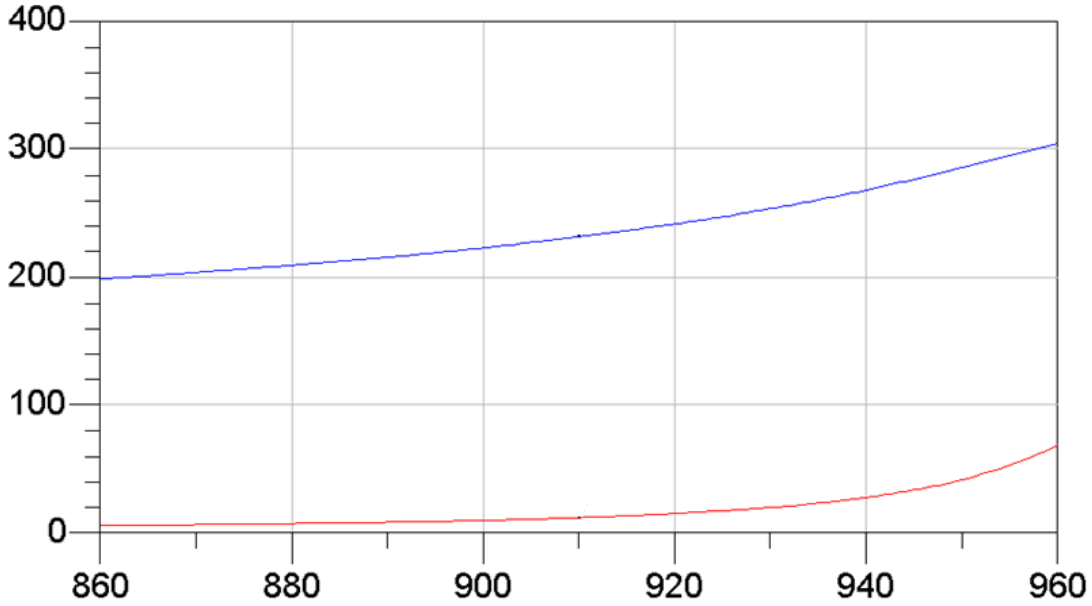

Figure 2.7. The balanced-mode measurement of the input impedance [Ω] of the tag antenna, Z_A, versus frequency ranged from 860 MHz to 960 MHz; the red line is for the real part of Z_A and the blue line is the imaginary part of Z_A.

2.3 RFID Sensing by Active Sensor Signal

For a passive tag, the application-specific integrated circuit (ASIC) of the tag switches its input impedance between two states to modulate the RCS of the tag antenna. Piggyback modulation technique operates based on the same principle: the voltage controlled sensor coupling module manipulates the backscattering wave by varying the effective input impedance of the tag antenna. Figure 2.1 shows the block diagram of the concept of piggyback modulation.

2.3.1 Active Sensor Coupling Module

For passive RFID tags, the backscattered modulation is achieved by controlling the input impedance of tag antenna's load and it can be manipulated through coupling a sensor signal via a sensor coupling module. The sensor coupling module consists of a coupling loop and a PIN diode modulator, as indicated in Figure 2.8. The modulation overlay is both physical and logical as shown in Figure 2.9.

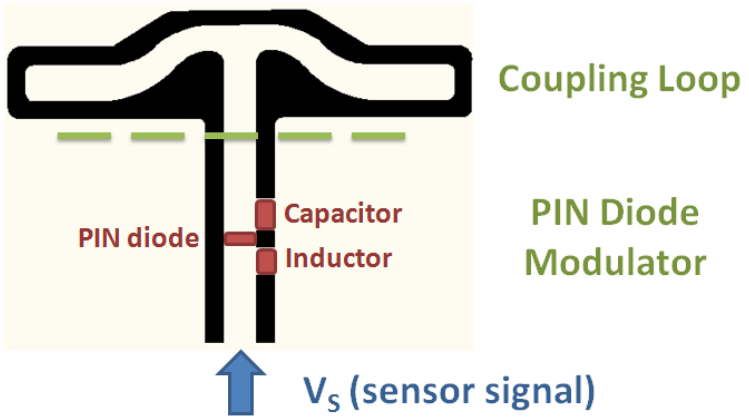

Figure 2.8. Sensor coupling module: one coupling loop and one PIN diode modulator.

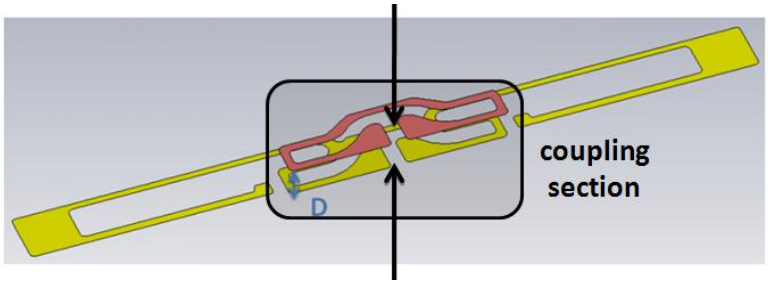

Figure 2.9. Coupling design consists of coupling loop (red) and commercial UHF RFID passive tag, AD-222 (yellow).

The coupling loop connects the sensor coupling module and ASIC so that the signal is modulated on the backscattered signal. The coupling is a function of the material, the shape, and the gap between coupling loop and tag, and it is characterized with S-parameters. In this study, the shape of the coupling loop is identical to the loop section of the AD-222 antenna, and the material of the coupling loop is good conductors, like copper. The coupling mechanism is modeled as a two-port network, and the full set of S-parameters from 860 to 960 MHz with various gaps is obtained by using CST Microwave Studio.

The PIN diode modulator is composed of a capacitance, an inductance, and a PIN diode, shown in Figure 2.10. Given the PIN diode as a current controlled device, the input impedance of the PIN diode modulator is a function of the voltage source.

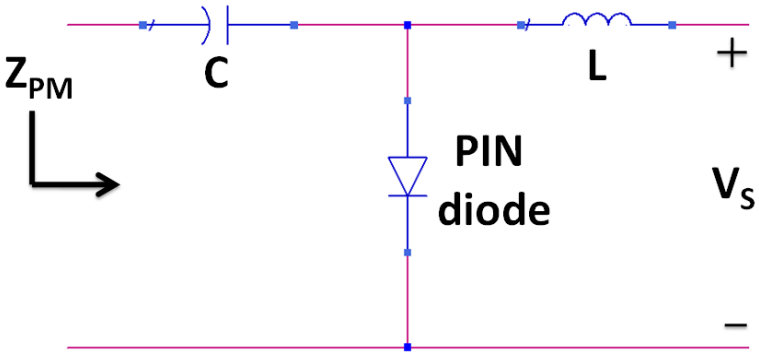

Figure 2.10. PIN diode modulator equivalent circuit.

The PIN diode modulator impedance is a function of the equivalent resistance of the PIN diode, which decreases exponentially as the voltage increases in forward bias. In this design, the inductance and the capacitance are chosen to be 68 nH and 22 pF individually. The measurements of the input impedance, Z_{PM}, versus input voltage, V_S, from are shown in Figure 2.11. The fact of the input impedance of the PIN diode modulator at low V_S (0~100 mV) is distinct from that at high V_S (700~800 mV) is good for digital modulations. On the other hand, the linear transition region between these two distinctive cases is located at the middle range of V_S (300~700 mV) where a good linearity is provided for analog modulations.

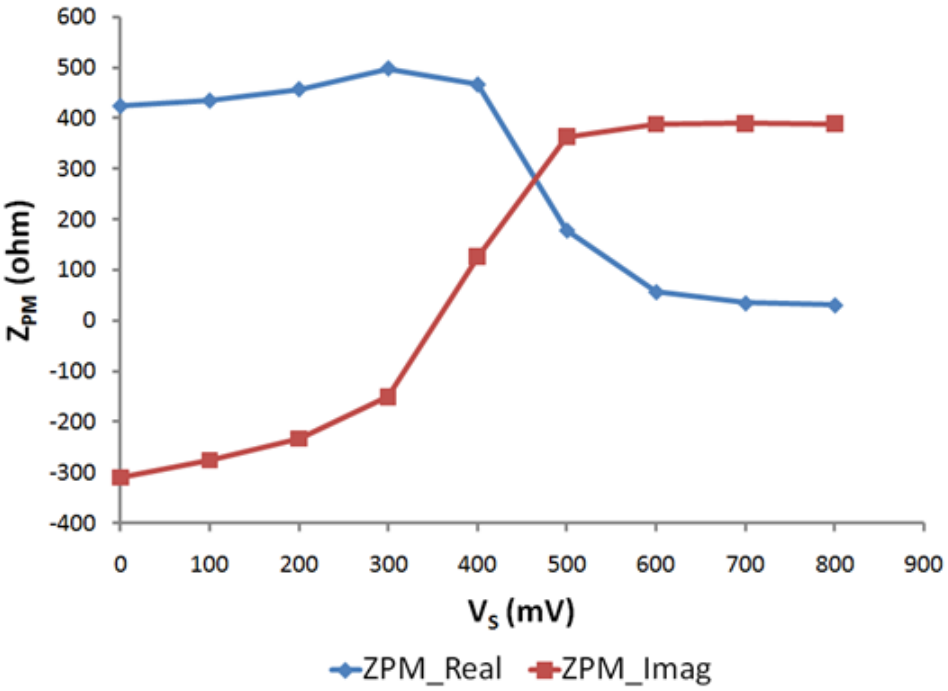

Figure 2.11. The input impedance of the PIN diode modulator, Z_{PM}, versus input voltage, V_S.

For a sensor set that has its own power source and storage device, the proposed RFID sensor, an integration of a commercial passive RFID tag and a sensor, could acquire sensing information without being illuminated by a reader although the data transmission still relies on the backscattering modulation, like typical passive tags. This design is also applicable for sensors that can harvest power from the reader or consume no power at all. The key of the piggyback modulation is the coupling mechanism that provides a link to the reader through the existing communication channel for sensor data transmission. This coupling is implemented by attaching a coupling loop to a tag with a small gap. The coupling characterized by 2-port S-parameters depends on not only the material, the shape, and the size of the coupling loop, but also the gap between the coupling loop and tag. The backscattering modulation is performed by two independent sources, the tag ASIC through a conductive connection and the additional sensor through the wireless coupling.

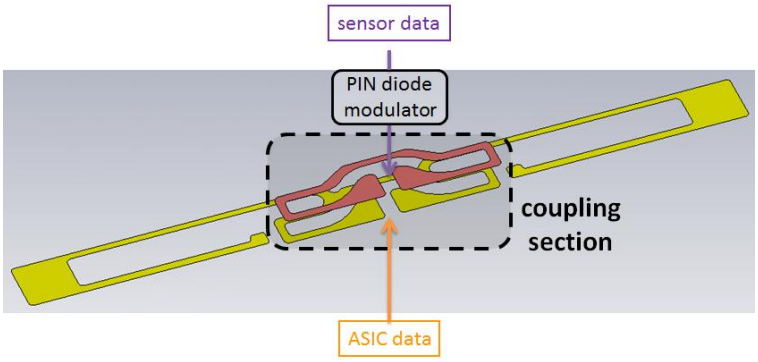

(a)

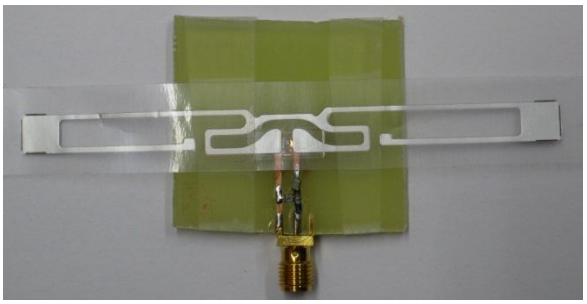

(b)

Figure 2.12. (a) Coupling design consists of coupling loop (red) and commercial UHF RFID passive tag, AD-222 (yellow). (b) RFID sensor prototype is comprised of AD-222 and the fabricated sensor coupling module; the emulated sensor signal is fed through the SMA connector.

The RCS of the combined tag and sensor coupling module or the V_{BS}, the backscattered signal strength, changes as varying V_S and the transfer function describes what is needed for connecting the input and the output thoroughly. That means anyone who wants to integrate one sensor into a commercial tag only need to know what the transfer function is and does not have to care about these complex equations. To be noticed, the RCS is a scalar value of area size as a measure of how detectable of an object and it is proportional to the square of the distance between Γ_m and A_S. Nonetheless, the vector from A_S to Γ_m is comprised of the amplitude and the phase. For ASK modulation, knowing the scalar RCS values of different Γ_m is enough. Compared with measuring scalar RCSs for signal detection, having both amplitude and phase of V_{BS} could make the backscattered signal more immune to noise.

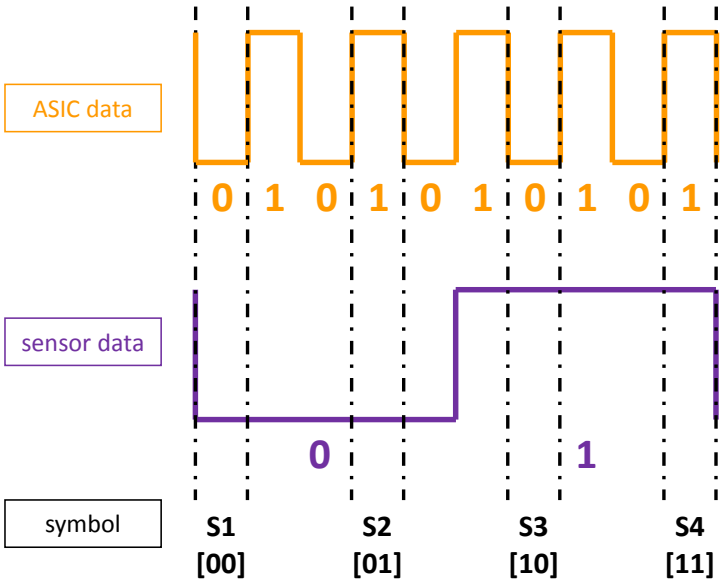

Figure 2.13. Binary signal waveforms of the ASIC data stream and the sensor data stream, and the corresponding four symbols of the combination.

In prior of attaching the sensor coupling module, the RCS of a tag only has two values corresponding to two states of Z_{ASIC}, and it is used for either ASK or PSK modulation. The reflection coefficient, Γ_m, has two different locations individually representing state "0" and "1" for ASIC data. Adding the sensor coupling module makes the effective input impedance at the tag antenna Z'_{ASIC} which is dependent on both Z_{ASIC} and Z'_{PM}, input impedance of the sensor

coupling module. In other words, the backscattered signal is manipulated by two independent sources.

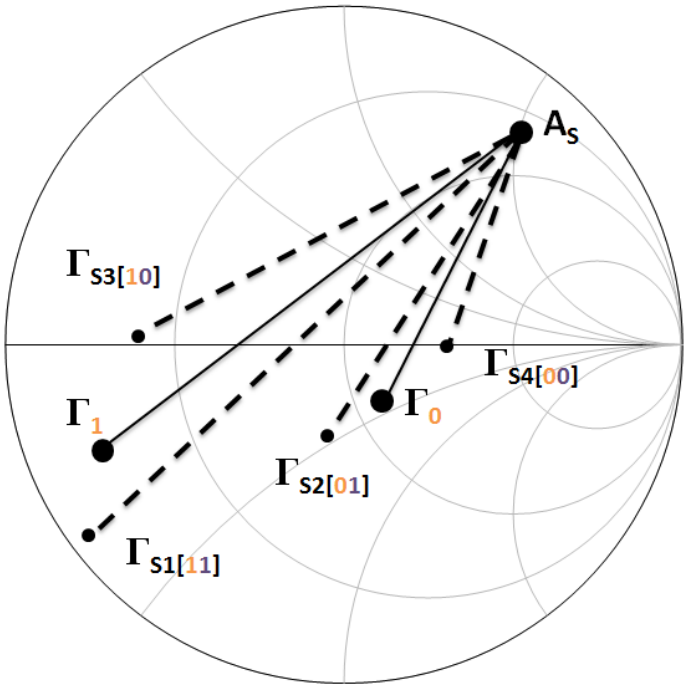

Figure 2.14. Graphical representation of backscattering of loaded tag antenna with four different states on Smith Chart.

With its own modulation states for sensor data, the total number of distinct RCS values increases up to four. The locations of these states are determined by both ASIC data and sensor data. Even though there are only four points corresponding to four difference states when the applied V_S has two distinct values, there could be two continuous trajectories as V_S varies from low level to high level across the turn-on voltage individually for each of the states of ASIC. Actually, these are curves of transfer function which are dependent on the impedance of ASIC and the carrier frequency and the measurements will be presented later. In this design, two independent data sets can be modulated on the backscattered wave independently and simultaneously. For digital signals, both of ASIC and sensor coupling module have its own two distinct states representing “1” and “0”, and the overall four different states modulation on the backscattered wave.

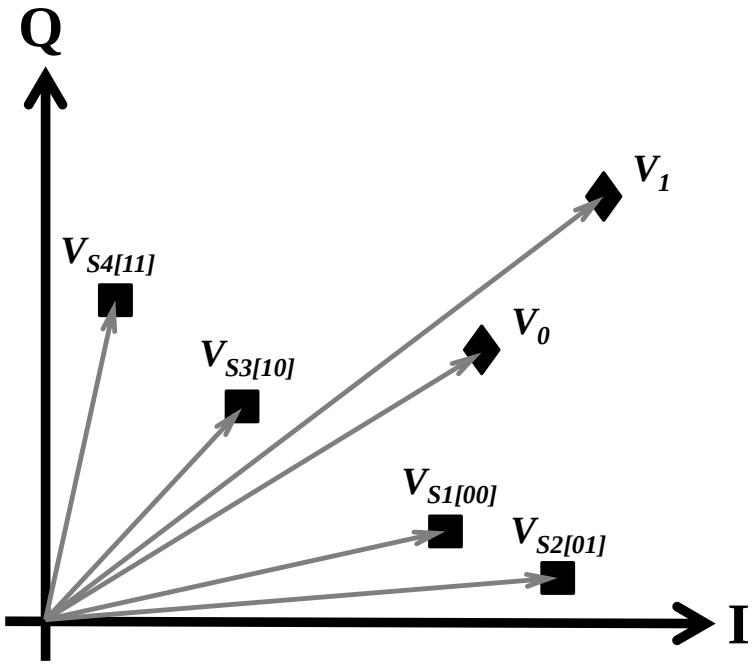

Figure 2.15. The illustration of the vector backscattered signals without piggyback modulation: {V_0, V_1} and the vector backscattered signals with piggyback modulation: {$V_{S1[00]}$, $V_{S2[01]}$, $V_{S3[10]}$, $V_{S4[11]}$} on the I-Q plane.

The vector backscattered signals of a tag are determined by the input impedance of tag antenna's load, Z_L. Without attaching the sensor coupling module, Z_L is equal to Z_{ASIC}, which provides two different complex numbers depending on the design of the ASIC; the vector backscattered signal of a tag has two symbols representing bit '0' (V_0) and '1' (V_1), as indicated in Figure 2.15.

With the attachment of the sensor, the input impedance of the tag antenna is modified and Z_L is a function of both Z_{ASIC} and Z_{SCM}. Eventually the vector backscattered signals of the RFID sensor prototype are decided by the sensor signal, V_S. For transmitting a binary data stream, V_S switches between only two different voltage levels and then two different complex Z_{SCM} are provided correspondingly. Four corresponding symbols are made by the combination of two binary data streams from the ASIC and the sensor. The vector backscattered signals with piggyback modulation, $V_{S1[00]}$, $V_{S2[01]}$, $V_{S3[10]}$, and $V_{S4[11]}$, are shown in Figure 2.15.

The location of each symbols is determined by the choice of V_S. A larger symbol separation on the constellation diagram improves the demodulation of the digital piggyback modulated signal. Thus the performance is related to the absolute values of V_S in the two switching states. Furthermore, two individual trajectories migrating from the coordinates of the $\boldsymbol{V_{S1[00]}}$ and $\boldsymbol{V_{S2[01]}}$ to $\boldsymbol{V_{S3[10]}}$ and $\boldsymbol{V_{S4[11]}}$ are acquired while V_S varies from its minimum operation voltage level to its maximum.

2.3.2 Measurement Results

This section focuses on the measurements of the static RCS and the real-time backscattered signal of the combined tag and sensor coupling module at carrier frequency f_C = 915 MHz. In the static RCS measurement, the impedance of the non-awaken ASIC, Z_{ASIC}, stays constant as the V_S varies from 0 to 800 mV with increment of 100 mV. The curves of the RCS of the tag and sensor coupling module sweeping through global UHF RFID frequency range (860MHz - 960 MHz) for V_S from 0 to 800 mV is shown in Figure 2.16.

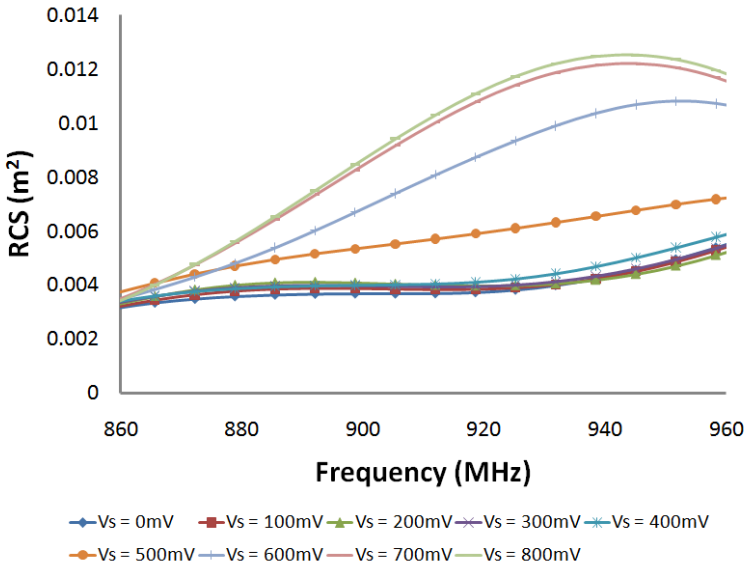

Figure 2.16. RCS variation with V_S from 0 to 800 mV.

In the real-time backscattered signal measurement, one RFID reader is used to build up the communication with the tag by transmitting standard down-link signals. The backscattered signal as seen from the reader is captured by a horn antenna in the same location as the reader antenna and fed to a vector signal analyzer (VSA) along with signals from the RFID reader.

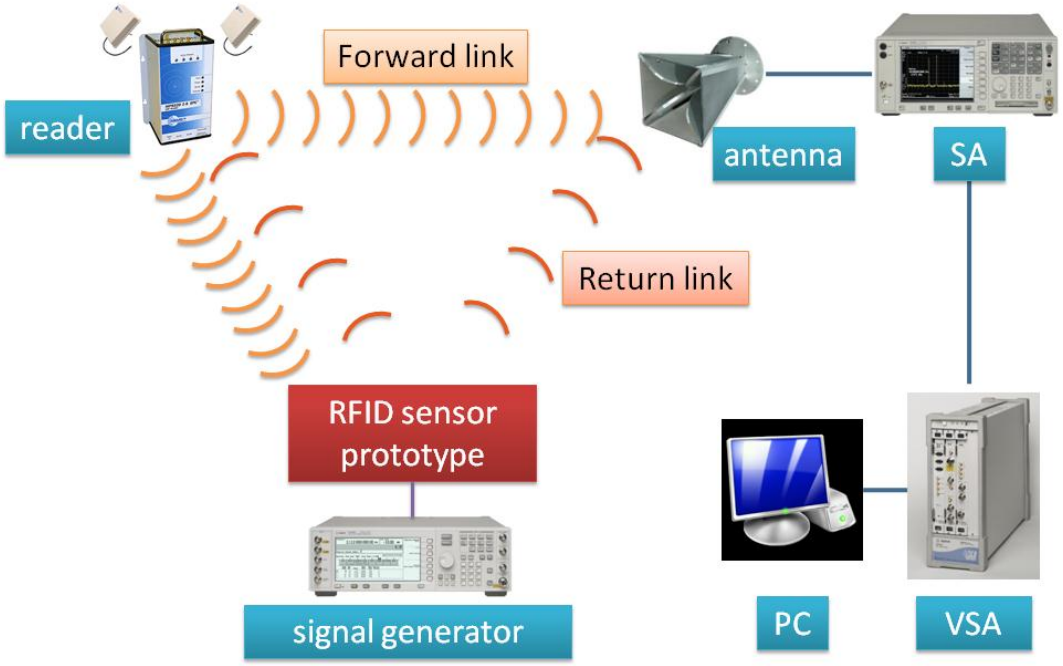

Figure 2.17. Experimental setup for real-time backscattered signal measurement.

First, the square wave is chosen as the waveform of the digital signal with frequency 5 kHz and amplitude 340 mV. The add-on square wave signal is shown coexisting with the identification data string in the time domain measurement. The real-time signal and corresponding spectrum measurements without and with piggyback modulation are indicated in Figure 2.18. Secondly, a 5 kHz sawtooth waveform from 0 to 800 mV is applied as V_S. The real-time signal measurement reveals the transfer function curves while Z_{ASIC} switches between two states, as indicated in Figure 2.19.

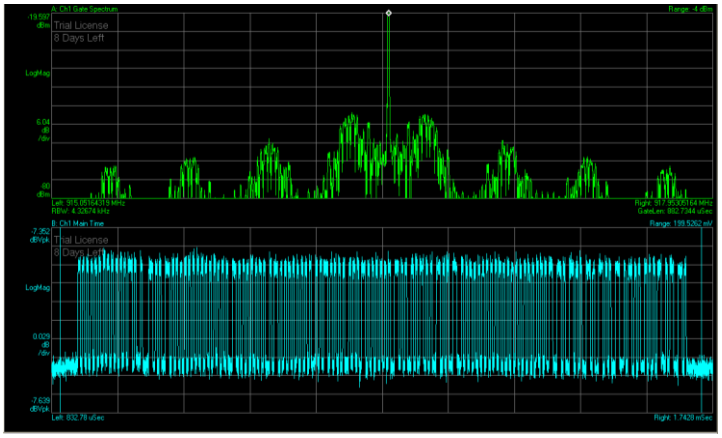

(a)

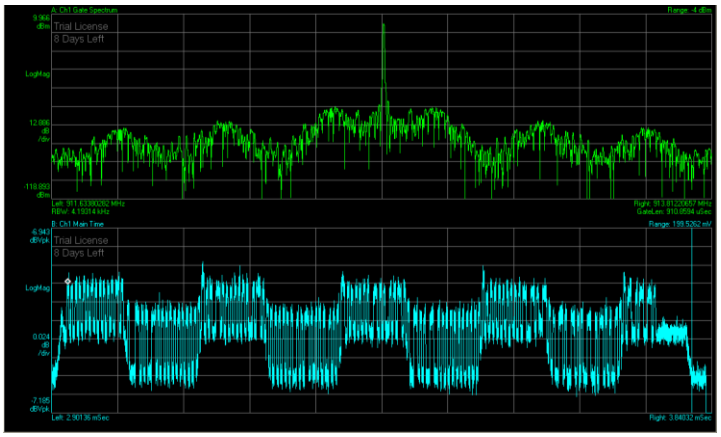

(b)

Figure 2.18. Real-time signal measurement (a) without digital piggyback modulation; (b) with digital piggyback modulation.

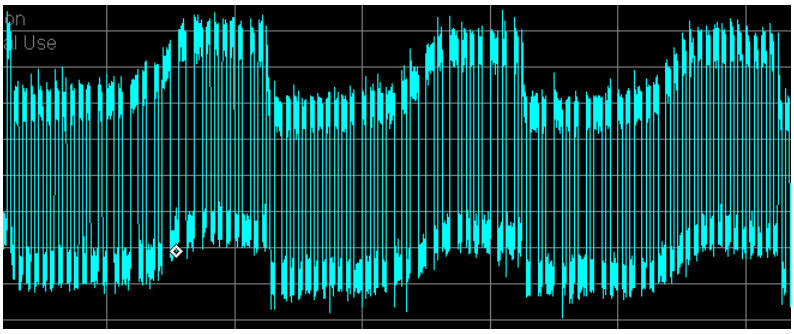

Figure 2.19. Real-time piggybacking signal measurements at f_C = 915 MHz; V_S is a 5 kHz sawtooth waveform from 0 mV to 800 mV.

The measurement results of the received power of real-time backscattered signal and the static RCS show great consistence, as shown in Figure 2.20, while Z_{ASIC} stays one state. The transfer function curve shows three regions. Region I (V_S: 0 ~ 400 mV) provides relative low value of RCS; region II (V_S: 400 ~ 600 mV) is the transition; Region III (V_S: 600 ~ 800 mV) provides relative high value of RCS. To have better received signal quality, the operation points/range of V_S should be wisely chosen for digital/analog signals. Two distinct states are needed for digital signals to achieve better SNR and lower BER; hence the operation points should be in region I and III. Analog signals require good linearity to avoid unwanted harmonic terms, so the operation range should be located in region II.

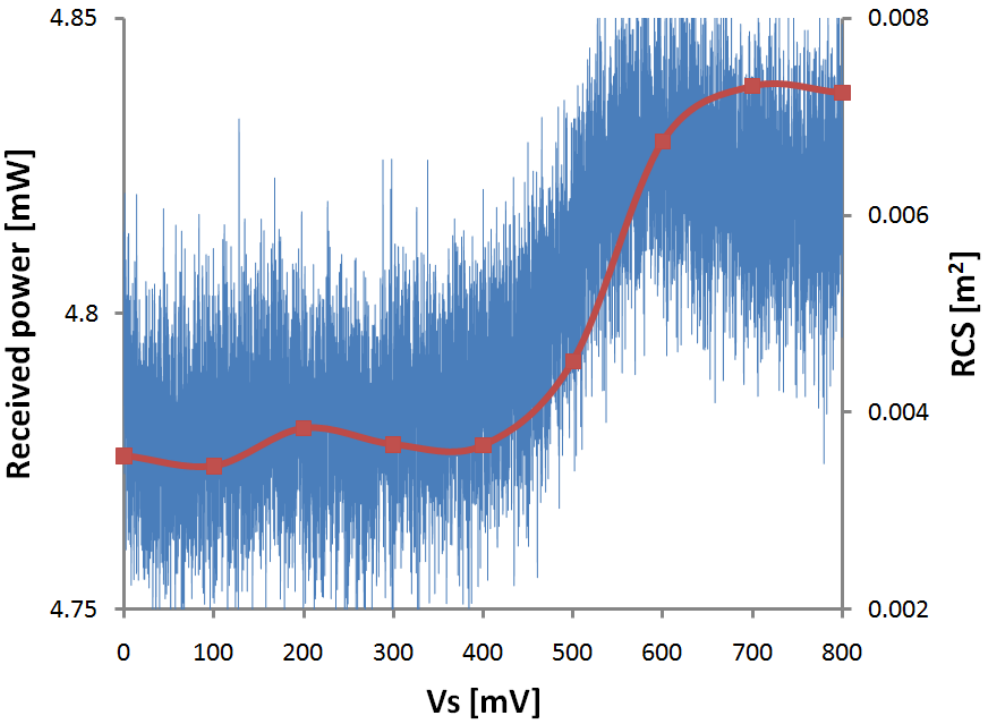

Figure 2.20. The transfer function measurement at f_C = 915 MHz: received power of real-time backscattered signal (blue), static RCS with V_S from 0 to 800 mV.

The measurement setup and the experimental results for the vector backscattered signals with and without piggyback modulation are presented below. In this measurement setup, a vector signal generator, a vector signal analyzer, a circulator, and an antenna are used; the antenna and the target under test are placed in an anechoic chamber. The schematic diagram of the setup is indicated in Figure 2.21.

To have a true backscattering measurement, one single antenna is used to complete both signal transmission and reception. The transmitting/receiving antenna and the target, RFID tag or RFID sensor prototype, are placed in an anechoic chamber to reduce the unwanted reflections from the environment. One 3-port circulator connects the vector signal generator, transmitting/receiving antenna, and the vector signal analyzer to provide two separate paths for transmitted and received signals with isolation around 25 dB.

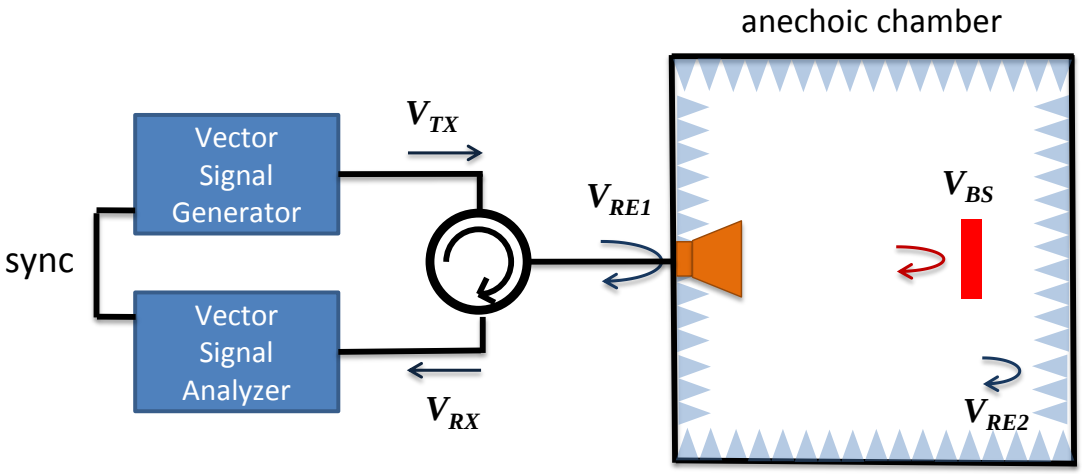

V_{TX} : Transmitted signal
V_{RX} : Received signal
- V_{RE1} : Reflection of antenna mismatching
- V_{RE2} : Reflection of the anechoic chamber
- V_{BS} : Backscattered signal from the scatterer

Figure 2.21. Schematic diagram of the measurement setup.

To capture the two different backscattering vectors from a RFID tag and the four different backscattering vectors from a RFID sensor prototype, the tag ASIC needs to be awakened by receiving a Gen2 standard forward link signal that contains request commands. Rather than using a standard UHF RFID reader to awake and communicate with a tag, a vector signal generator is used to generate the Gen2 standard forward link signal. In addition, it solves the problem of measuring signals at one fixed carrier frequency since standard readers are designed to produce carrier frequency randomly hopping around within 902-928 MHz, the ISM band of UHF RFID systems in North America. The phase measurement is viable because the vector signal generator and the vector signal analyzer are synchronized with rms phase error less than 1 degree.

The experimental results of the vector backscattered signals with piggyback modulation in the time domain are presented. The commercial passive UHF RFID tag AD-222 loaded with the Monza 2 ASIC is used. The sensor coupling module, which is composed of a 22 pF capacitor, a 68 nH inductor and a PIN diode, is fed by an emulated sensor signal, V_S, a 5 kHz square waveform operating between 0 and 800 mV. The carrier frequency is set and fixed at 915 MHz, which is the central frequency of the UHF RFID operation band in North America. The RF output power is set to +15.0 dBm in the vector signal generator. Four symbols of the vector backscattered signal from a sensor prototype are represented by four magnitude levels of the amplitude and four locations in the constellation diagram, as shown in Figure 2.22 (a) and (b).

As addressed in the previous section, the vector backscattered signal of the RFID sensor prototype, which is a function of the input impedance of the tag antenna, Z_{load}, varies whenever Z_{ASIC} or Z_{SCM} changes. In Figure 2.23, two trajectories representing two different Z_{ASIC} impedances are shown as V_S modifies Z_{SCM} by operating from its minimum voltage level to the maximum: 0, 50, 100 … 700, 750, 800 mV; one migrates from S1[00] to S3[10] and the other one is from S2[01] to S4[11].

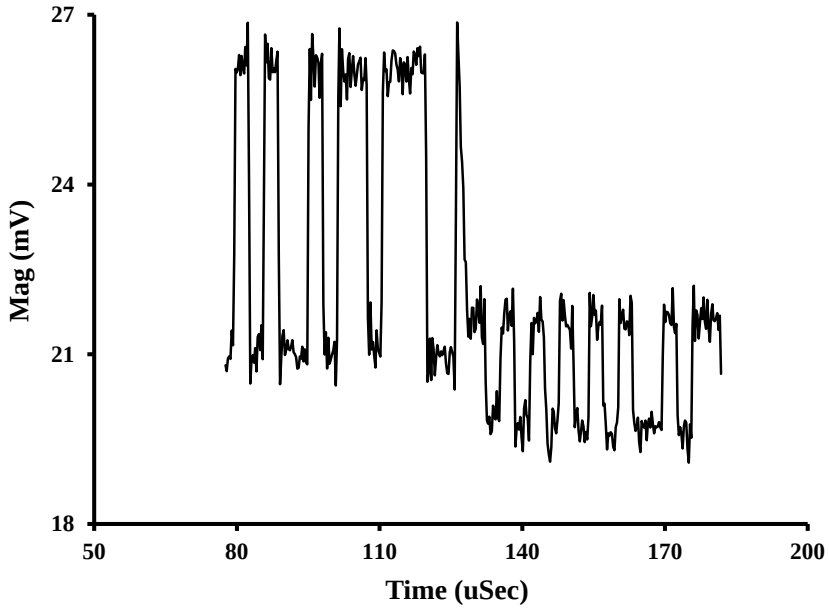

(a)

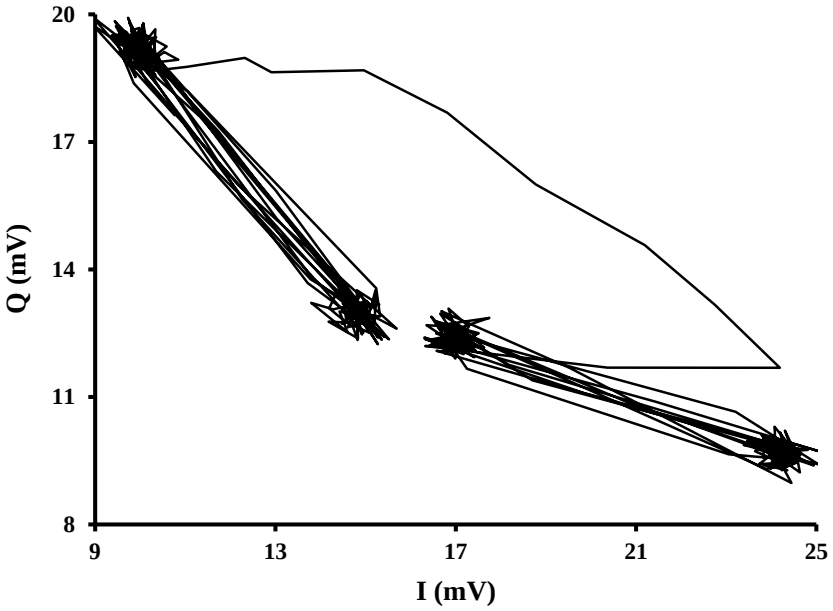

(b)

Figure 2.22. Time-domain measurements of the vector backscattered signals with piggyback modulation in (a) Amplitude and (b) constellation diagram. (V_S: 5 kHz square wave between 0 and 800 mV; RF output power: +15.0 dBm).

A transition is observed for the S2[01] - S4[11] trajectory when V_S varies from 400 to 600 mV while the rest of points are grouped around S2[01] and S4[11] for V_S = 0 - 400 mV and 600 - 800 mV, respectively. The transition also happens on the other trajectory, but it is not obvious because S1[00] and S3[10] are close. For the digital piggyback modulated signal, the distance between each of these four symbols determines the demodulation performance in terms of BER. Therefore, the two switching voltage levels of the digital sensor signal, V_S, can be wisely chosen knowing the trajectories of the backscattered signal. Increasing V_S does not always improve the demodulation performance, since the symbol distance is not necessarily linearly proportional to the value V_S.

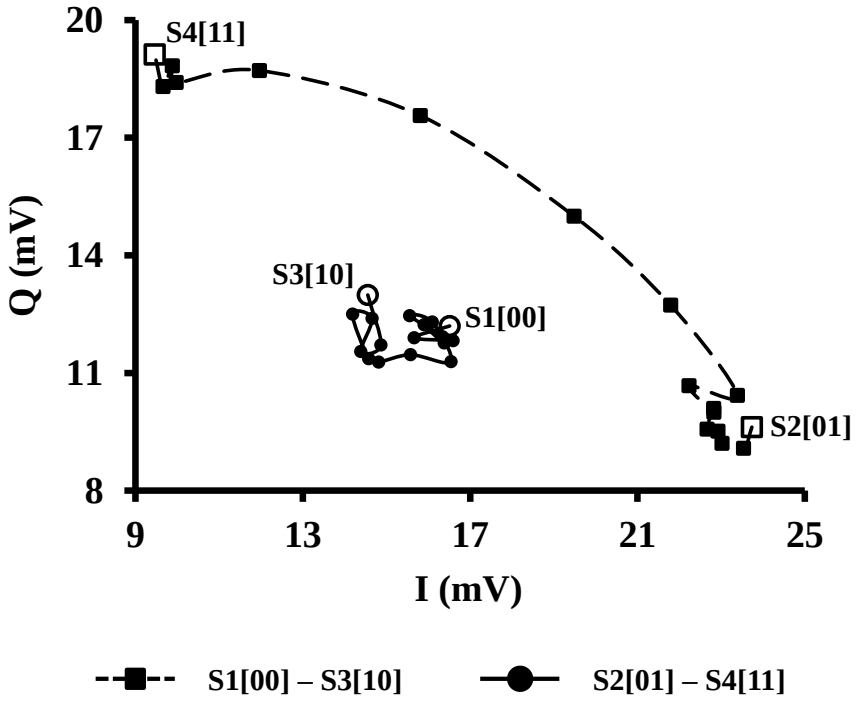

Figure 2.23. Two trajectories start from S1[00] and S2[01] to S3[10] and S4[11]. (VS: sawtooth wave ramping upward from 0 to 800 mV with an interval of 50 mV; RF output power: +15.0 dBm).

Given the fact that Z_{ASIC} depends on the power of the incident wave, the vector backscattered signal varies with different RF power levels set in the vector signal generator. This vector signal experiments of a tag and a sensor prototype is made at a carrier frequency of 915 MHz, with V_S as a square wave between 0 and 800 mV, and three RF output power levels at +15.0, +17.5, and +20.0 dBm. The measurement of the constellation diagram of the received vector signal is shown in Figure 2.24. The received vector signals of a tag and a sensor prototype are shifted rightward and upward as the RF output power increases. The relative locations of the four symbols vary as RF output power increases, while the distance between them is not obviously proportional. Again, the location of each of the symbols plays a key role for the demodulation performance which will be analyzed and presented in the next section.

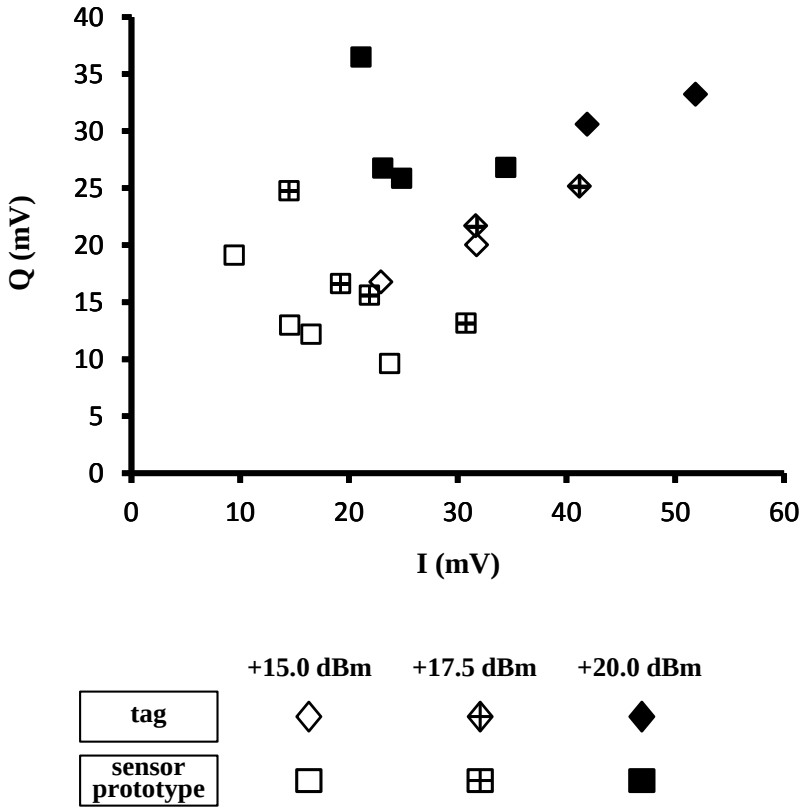

Figure 2.24. The constellation diagram of the received vector signals of the tag and the sensor prototype. (V_S: 5 kHz square wave between 0 and 800 mV; RF output power: +15.0 dBm, +17.5 dBm, and +20.0 dBm).

The received vector signal is the combination of the reflected signal of reader antenna mismatch, $\boldsymbol{V_{RE1}}$, the reflection of the imperfection of the anechoic chamber room, $\boldsymbol{V_{RE1}}$, and the backscattered signal from the target, $\boldsymbol{V_{BS}}$. The backscattered signal from the target is obtained by the subtraction of the background vector signal which is measured for having no target and contains the reflected signal of reader antenna mismatch and the reflection of the imperfection of the anechoic chamber room. The measurement environment must be stable during all measurements.

2.3.3 Analysis of Demodulation Schemes

With the piggyback modulation, two independent data sets are simultaneously modulated on the same carrier wave received by a reader. The current standard demodulation scheme is valid for the signal carrying ASIC data only. Therefore, the demodulation scheme has to be modified to detect both the ASIC data and the sensor data. In this section, we present and analyze the three different demodulation schemes: the split-two-level ASK demodulation, the four-level ASK demodulation, and the quasi-4-QAM demodulation.

In the split-two-level ASK demodulation, the data detection is individually processed for the ASIC data stream and the sensor data stream. The ASIC signal demodulation is by amplitude threshold detection with a threshold performed while the embedded sensor signal is treated as noise. Due to the interference from the sensor signal, the bit error rate (BER) of the ASIC data stream is dramatically deteriorated when increasing frequency or amplitude of the piggybacked signal. The read rate is defined as the number of identification data strings received by a reader within a fixed period of time, and it is an indication of signal quality. Read rate reduction arises from the interference of the piggybacking signal, since it is treated as noise from the perspective of the identification signal. As expected, the read rate is reduced with increasing frequency and amplitude of the piggybacking signal as indicated in Figure 2.25.

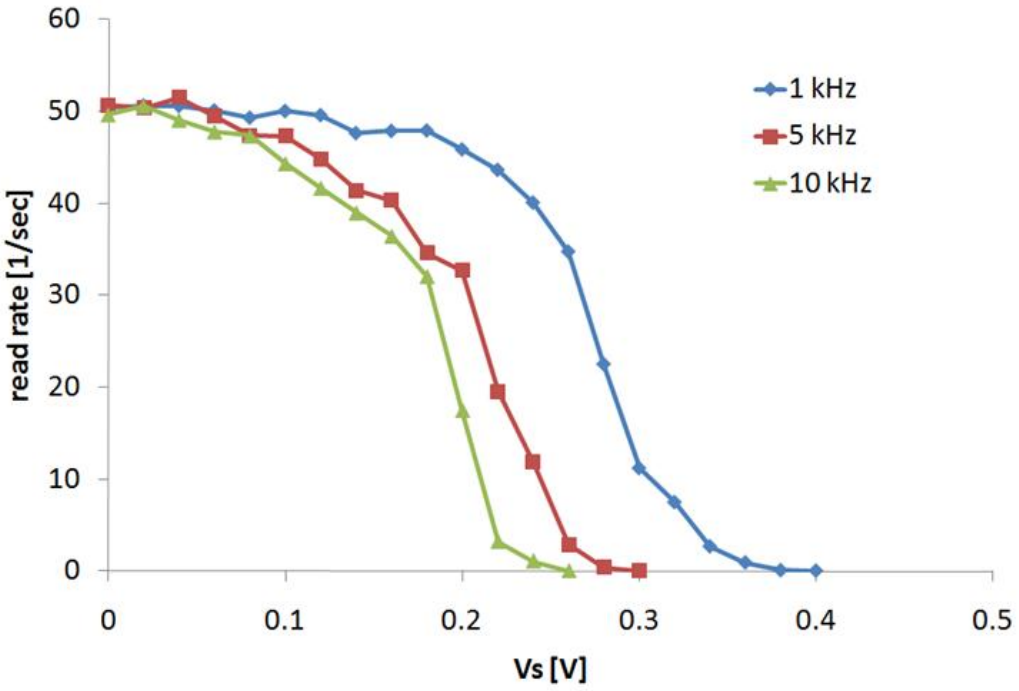

Figure 2.25. Read rate versus amplitude and frequency of the voltage source from digital piggybacking signal.

To demodulate the sensor signal, a low pass filter is required to recover the waveform of the sensor signal, which normally has lower bit rate. The demodulation of the sensor signal is performed based on amplitude threshold detection with a threshold T_{sensor}. The detection output bits, x_{ASIC} and x_{sensor}, can be expressed as

$$x_{ASIC} = \begin{matrix} 0, \ if \ |y| < T_{ASIC} \\ 1, \ if \ |y| > T_{ASIC} \end{matrix} \tag{2.11.1}$$

$$x_{sensor} = \begin{matrix} 0, \ if \ |y_{LF}| < T_{sensor} \\ 1, \ if \ |y_{LF}| > T_{sensor} \end{matrix} \tag{2.11.2}$$

where y and y_{LF} are received signal and its filtered output.

Generally, joint detection is better than individual detection [52]. Also, the problem of interference between two sets of data can be solved by performing the four-level ASK demodulation or quasi-4-QAM demodulation. Furthermore, BER performance of the received signals could be even improved if the demodulation is performed by taking into account both amplitude and phase. Hence, quasi-4-quadrature amplitude modulation is proposed to reduce the BER, transmit more bits per symbol, and use the bandwidth more effectively [53]. In these two joint detection schemes, each received signal is treated as one symbol, represented by two bits from each data stream. The received signal is demodulated according to its amplitude or location on the I-Q plane, as shown in Figure 2.26 and Figure 2.27. To extract two data streams from the piggyback modulated signal using four-level ASK demodulation, the decision rules are

$$x_{ASIC} = \begin{matrix} 0, \ if \ |y| \in A_1 \ or \ A_3 \\ 1, \ if \ |y| \in A_2 \ or \ A_4 \end{matrix} \tag{2.12.1}$$

$$x_{sensor} = \begin{matrix} 0, \ if \ |y| \in A_1 \ or \ A_2 \\ 1, \ if \ |y| \in A_3 \ or \ A_4 \end{matrix} \tag{2.12.2}$$

where A_1, A_2, A_3, and A_4 are the amplitude decision boundaries. On the other hand, quasi-4-QAM demodulation exploits both amplitude and phase of the piggyback modulated signal. The output bits are determined by the rules

$$x_{ASIC} = \begin{matrix} 0, \ if \ \vec{y} \in R_1 \ or \ R_3 \\ 1, \ if \ \vec{y} \in R_2 \ or \ R_4 \end{matrix} \tag{2.13.1}$$

$$x_{sensor} = \begin{matrix} 0, \ if \ \vec{y} \in R_1 \ or \ R_2 \\ 1, \ if \ \vec{y} \in R_3 \ or \ R_4 \end{matrix} \tag{2.13.2}$$

where R_1, R_2, R_3, and R_4 are the decision regions in I-Q plane.

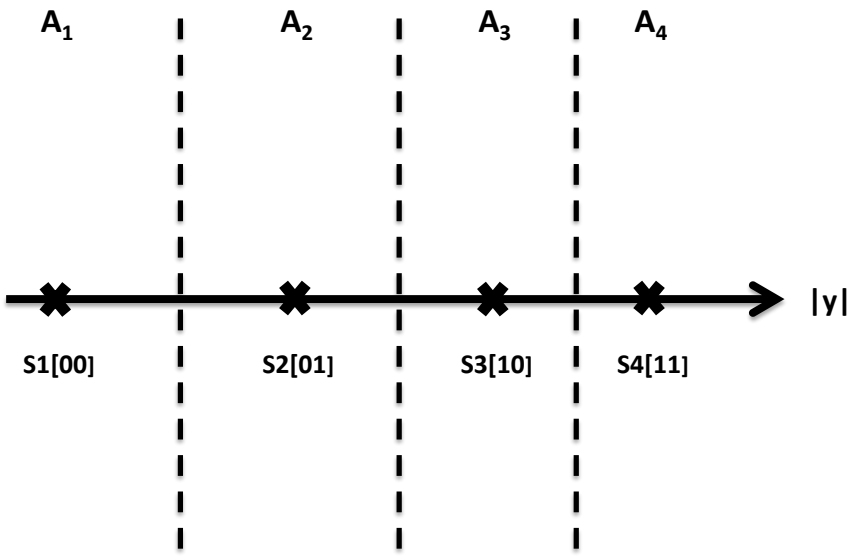

Figure 2.26. The four-level ASK demodulation.

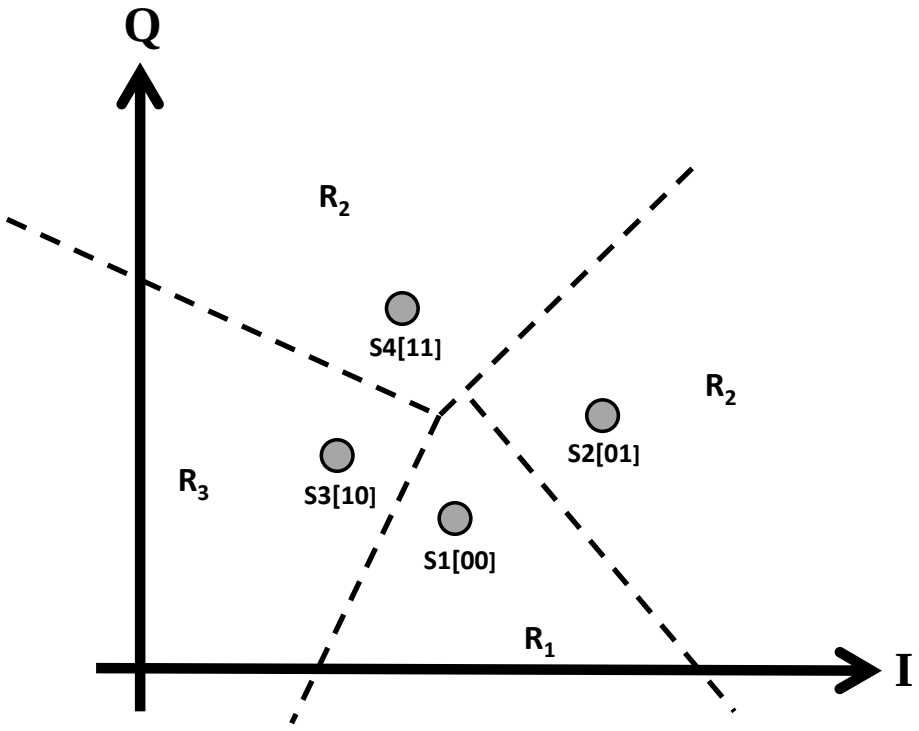

Figure 2.27. Quasi-4-QAM demodulation.

Typical digital modulation schemes have all the symbols uniformly located around the origin of the I-Q plane, while in backscatter modulation, all the symbols are pulled far from the origin. This is because the received signal contains not only the return link signal but also the leakage forward link signal. Therefore, to achieve the same BER performance, much higher signal-to-noise ratio (SNR) is required in the backscattering modulation compared with other more typical digital modulation schemes.

BER comparisons of these two demodulation schemes, in which the symbol constellation is measured by the actual experimental results, are done by numerical simulations. The bit rate ratio of the ASIC signal and the sensor signal is set to 5; therefore, the bandwidth of the sensor data is 1/5 of the bandwidth of the ASIC data. In the simulation, the channel is assumed to be an additive white Gaussian noise (AWGN) channel. At the demodulator, the minimum distance detection rules are applied according to (2.13.1) and (2.13.2). The measured I/Q values for each symbol are imported in the Monte-Carlo simulation. The plots of BER versus SNR for the measured vector backscattered signals of a tag and a sensor prototype are shown in Figure 2.28.

In vector backscattered signals from the tag, we observed little difference between the BER performance of the two-level-ASK demodulation and I-Q demodulation for three RF output power levels. The phases of the bit ‘1’ (≈ 32 deg) and bit ‘0’ (≈ 35 deg) are very close; i.e. the amplitude is the major difference between this two symbols. Therefore, the improvement of the BER performance due to using both amplitude and phase information in the I-Q demodulation is not apparent.

On the other hand, for the vector backscattered signals of the sensor prototype, the BER performance of quasi-4-QAM demodulation is better than that of the four-level ASK demodulation for both the ASIC data and the sensor data. The improvement of using quasi-4-QAM demodulation for the minimum required SNR to achieve target BER = 10^{-2} is ranged from 3 dB to 11 dB. Note that in typical digital modulation schemes, higher RF power provides greater distances between each of the symbols; the BER performance is enhanced. Here, the BER performance of backscattering piggyback modulation gets worse when RF output power increases because the distance between symbols is not markedly increased as higher RF output power is applied.

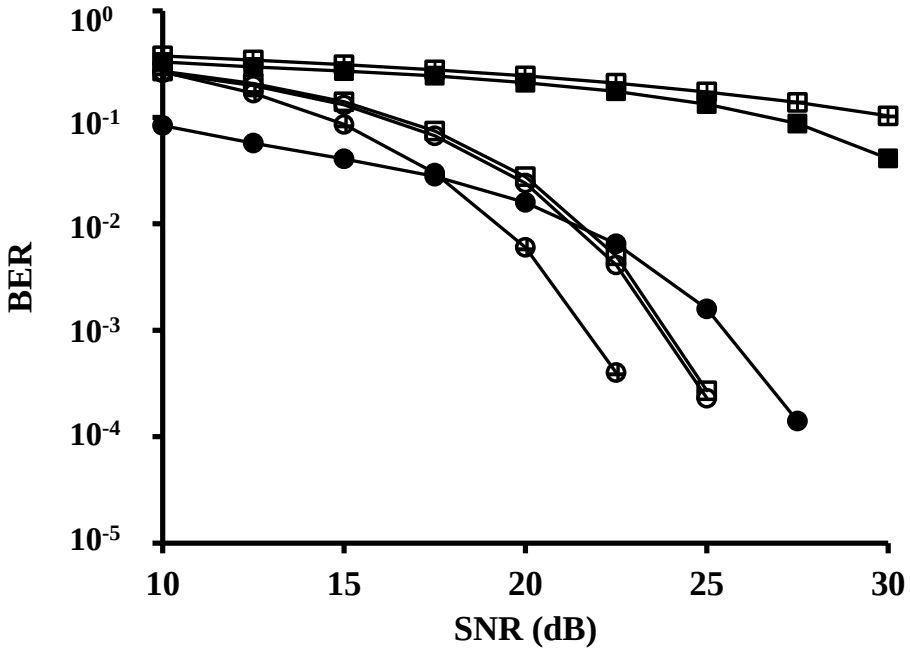
BER
10^{0}
10^{-1}
10^{-2}
10^{-3}
10^{-4}
10^{-5}
10
15
20
25
30
SNR (dB)

(a)

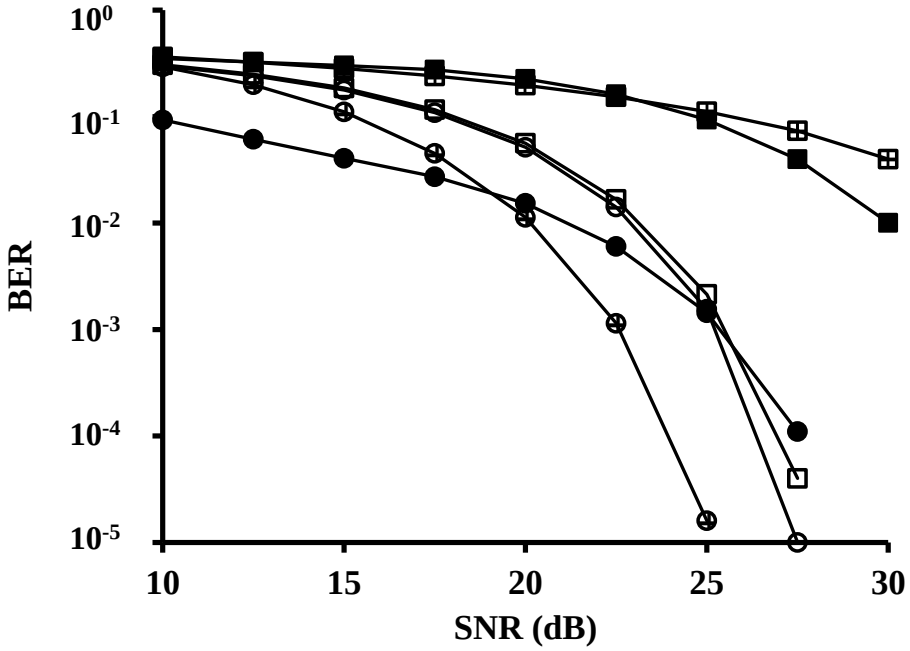
BER
10^{0}
10^{-1}
10^{-2}
10^{-3}
10^{-4}
10^{-5}
10
15
20
25
30
SNR (dB)

(b)

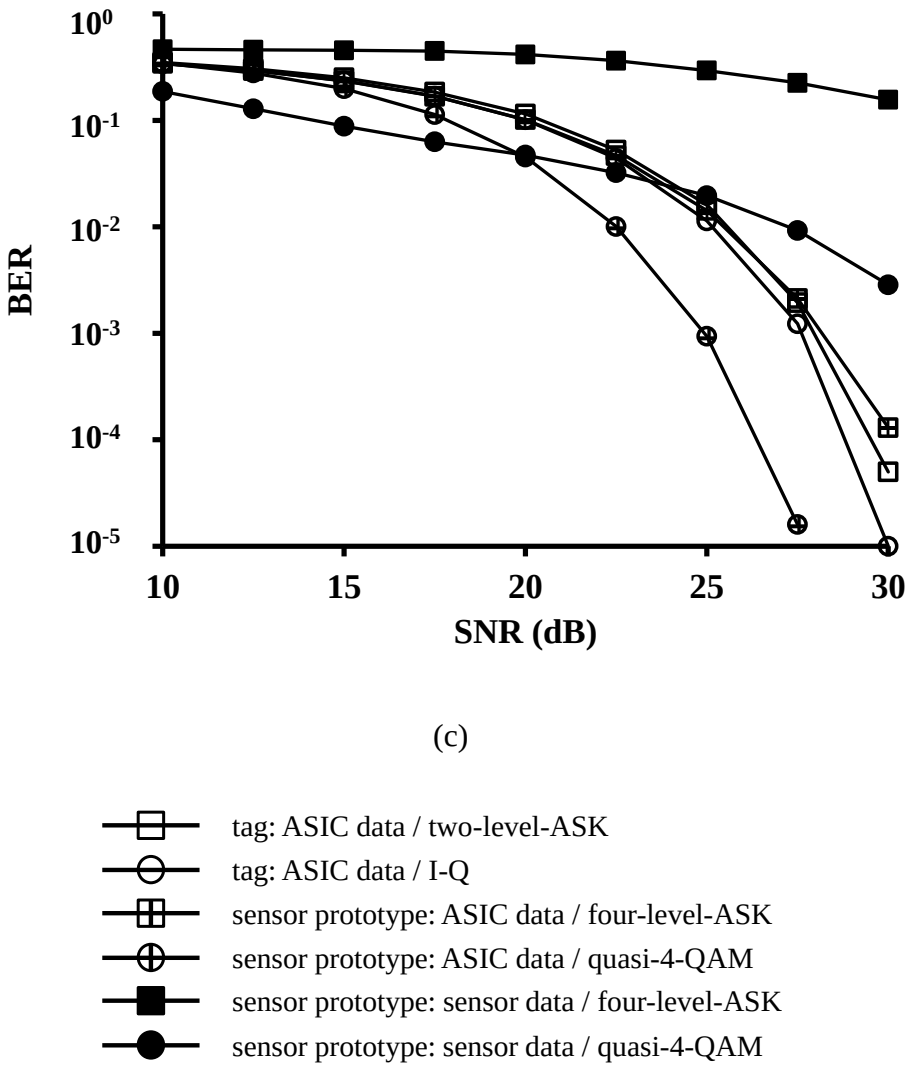

Figure 2.28. Monte-Carlo simulation of BER versus SNR for the measured vector backscattered signals of a tag and a sensor prototype. The bit rate ratio of the ASIC signal and the sensor signal is 5. (a) RF output power: +15.0 dBm. (b) RF output power: +17.5 dBm. (c) RF output power: +20.0 dBm.

In general, RFID tag reply error rates below 20% requires BERs of less than 10^{-3} [19], and typical systems achieve 99% reliability with BERs of 10^{-5} [45]. The quasi-4-QAM demodulation scheme provides sufficient BER for common applications, while the BER performance of the four-level ASK demodulation is inferior.

In this section, vector backscattered signals of the proposed RFID sensor prototype are measured, analyzed, and demodulated in both ASK and quasi-4-QAM schemes. The principle of

the piggyback modulation and the basics of the vector backscatter from a passive tag are addressed. The measurement setup for both amplitude and phase of the backscattered signal is presented. Using experimental results, we conduct the analysis and the numerical simulation of the BER performance comparison for different demodulation schemes. The results show the performance of quasi-4-QAM demodulation is superior to the 4-level-ASK demodulation. Future work could include integrating actual sensor signals, designing the actuation of the sensor, developing the synchronization of the sensor signal with the ASIC backscattered signal, improving the coupling loop design, and applying this technique to different tags.

2.4 RFID Sensing by Passive Sensor Loads

The integration of the sensors and standard RFID tags can be implemented through redesigning the application-specific integrated circuit (ASIC) of the tag. Also, the modification of the reader is needed for recognizing add-on sensor data. Piggyback modulation, which was previously presented for active digital sensor signal overlay [11], [12], [54], is another approach for simultaneously transmitting ID information and sensor data. As in [54], the wireless coupling mechanism is not only applicable to active sensor data but also passive sensor data. Passive sensors provide different impedances corresponding to the physical parameters of sensing, like temperature, humidity, pressure, and so on. The modulated impedance of the passive sensor is embedded in the vector backscattered signals; that is to say, the measurement of the vector backscattered signals enables us to detect the impedance of the passive sensor and then acquire the sensing information. At the same time, the ASIC works for transmitting identification data with little interference.

In the followings, we present the overall conceptual design and the elements of the passive sensor coupling, address the basics of backscatter from a passive tag and the analysis of the vector backscattered signal with passive sensor coupling, and show the measurement setup and the experimental results.

This design shares the same principle of the piggyback modulation design [11], [12], [54], when it has no additional modulation driven by an active digital sensor signal. The wireless coupling implemented by the passive sensor coupling module (PSCM) provides a wireless link from the tag antenna to the passive sensor so that the passive sensor data characterized by the impedance can be included in the backscattered waves. The existing communication channel built between the reader and tag is used for carrying additional sensor data. To accurately detect the passive sensor data in a noisy environment, two reference impedances are needed.

2.4.1 Passive Sensor Coupling Module (PSCM)

The operation of passive sensor coupling and the equivalent circuit model for the RFID passive sensor prototype are shown in Figure 2.29. The passive sensor coupling module (PSCM) consists of two components: a coupling loop and a switch. The wireless coupling mechanism which provides the bridge for sensor data transmission is realized through the attachment of the coupling loop to the tag antenna with a dielectric gap. The shape of the coupling loop is identical to the coupling section of the tag antenna and the extended part connects the switch which is loaded with the first impedance reference, Z_{ref1}, the second impedance reference, Z_{ref2}, and the impedance of the passive sensor, Z_S. A DC voltage source is needed to power up the switch, and it can be supported by an additional rectenna harvesting impinging EM wave or built-in energy storage, such as a battery or a capacitor.

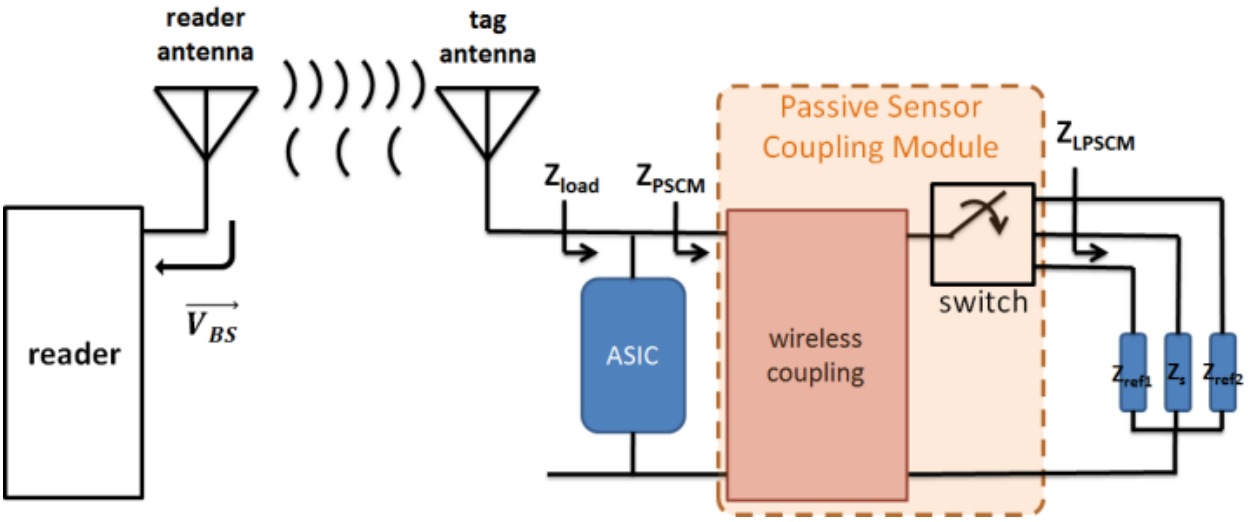

Figure 2.29. Operation of passive sensor coupling and the equivalent circuit model for the RFID passive sensor prototype.

The backscatter modulation is completed by the ASIC impedance modulation for transmitting binary signal; the reader acquires the ASIC data by the differential detection of the backscattering in amplitude or phase. However, the impedance of the passive sensor carrying the sensor data influences the value of amplitude and phase of the backscattering. The measurement

of the vector backscattered signals enables the characterization of the complex load but it is challenging to precisely detect the complex impedance of the passive sensor. For the transmission of the passive sensor data, the load of the passive sensor coupling module, Z_{LPSCM}, is switched between these three loads to provide the connection to one of the two reference impedances or the passive sensor. With two reference impedances, the impedance of the passive sensor is determined.

The vector backscattered signals of a tag are determined by the input impedance of tag antenna's load, Z_{load}. Without attaching the sensor coupling module, Z_{load} is equal to Z_{ASIC}, which provides two different complex numbers, $Z_{ASIC,0}$ and $Z_{ASIC,1}$, depending on the design of the ASIC. With the passive sensor coupling module, the input impedance of the tag antenna is modified and Z_{load} is a function of both Z_{ASIC} and Z_{PSCM}. Since Z_{PSCM} is dependent on the wireless coupling and the impedance of the load of the passive sensor coupling module, Z_{LPSCM}, the vector backscattered signal of the RFID passive sensor prototype is characterized by Z_{ref1}, Z_{ref2}, or Z_S. Six corresponding vectors are made by the combination of two binary data streams from the ASIC and three different values of Z_{LPSCM}. The vector backscattered signals with passive sensor coupling, V_{S1}, V_{S2}, V_{S3}, V_{S4}, V_{S5}, and V_{S6} are shown in Figure 2.30.

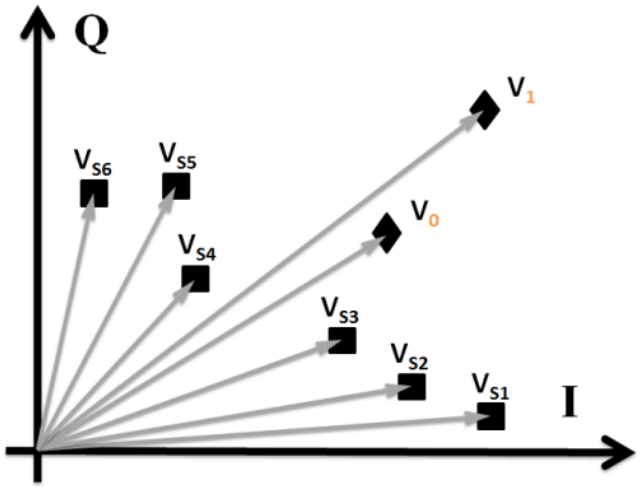

	S1	**S2**	**S3**	**S4**	**S5**	**S6**
$\mathbf{Z_{ASIC}}$	$Z_{ASIC,0}$	$Z_{ASIC,0}$	$Z_{ASIC,0}$	$Z_{ASIC,1}$	$Z_{ASIC,1}$	$Z_{ASIC,1}$
$\mathbf{Z_{LPSCM}}$	Z_{ref1}	Z_S	Z_{ref2}	Z_{ref1}	Z_S	Z_{ref2}

Figure 2.30. Conceptual illustration of the vector backscattered signals without passive sensor coupling: $\{V_0, V_1\}$ and the vector backscattered signals with passive sensor coupling: $\{V_{S1}, V_{S2}, V_{S3}, V_{S4}, V_{S5}, V_{S6}\}$ on the I-Q plane.

The key to wirelessly detecting the passive sensor data is the impedance measurement of the passive sensor. To achieve this, we need two reference impedances and the one-to-one mapping of the backscattering vectors and impedances. The sensing range sets the range of the resistive and reactive loads. Each of the corresponding vectors needs to be measured. The collection of all the vectors forms the one-to-one mapping for the backscattering vectors and impedances. For example, given the number of the resistive loads is M and number of the reactive loads is N; the total number of all the vectors in the mapping is M*N, as indicated in Figure 2.31.

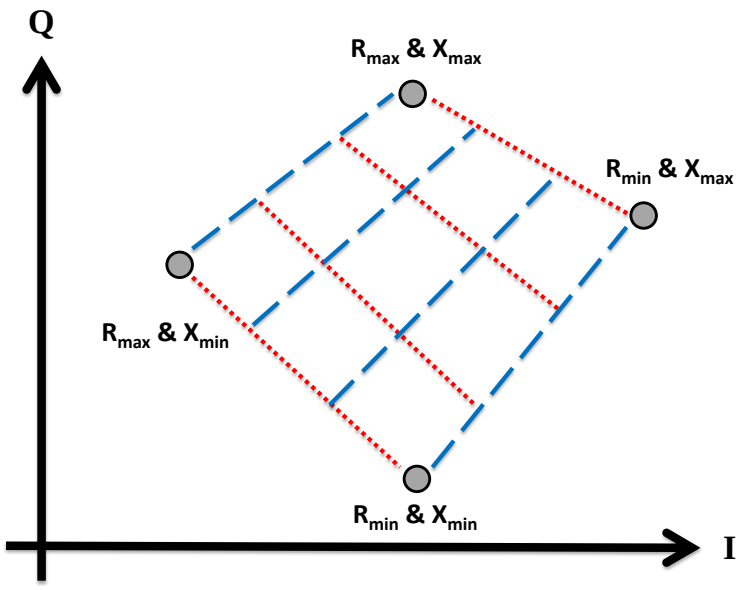

Figure 2.31. Conceptual illustration the one-to-one mapping for the backscattering vectors and corresponding impedances on the I-Q plane when Z_{ASIC} holds constant. Blue dash lines represent for the constant resistive loads; red dot lines represent for the constant reactive loads.

The mapping is consistent for ideal situations, like anechoic chamber room; however, it varies for practical environments with lots of external interferences. Therefore, two reference impedances with the maximum and minimum loads are used to define the mapping area. The unknown impedance of the passive sensor is determined by referring to the reference vectors with known impedances.

2.4.2 Measurement Results

The measurement setup and the experimental results for the vector backscattered signals of a commercial tag, AD-222, wirelessly coupled with various complex loads are presented in this section.

To measure the vector backscattered signal of a tag coupled with various impedances, the measurement setup is organized in an anechoic room. An antenna connected to a vector network analyzer is used for both transmitting and receiving signal. The RF output power is set at 0 dBm;

the frequency range covers the ISM band (902-928MHz) of UHF RFID systems in North America. In this measurement, the switch in not included and the ASIC is not awaked. The coupling loops connected to nine different complex loads are fabricated and measured, whereas each one of them is composed of one resistive load and one reactive load in series, as listed in Table 2-1.

The experimental results of the vector backscattered signals of the tag coupled with various loads at 902, 915, and 928 MHz are presented in Figure 2.32. The mapping of the backscattering vectors and impedances is frequency dependent. Each vector represents one unique complex load since none of the dashed line (constant resistive load) or the dot line (constant reactive load) intersects with one and the other. In the other words, the one-to-one mapping of the backscattering vectors and impedances is obtained for the frequency range of interest; therefore, complex loads can be exclusively determined.

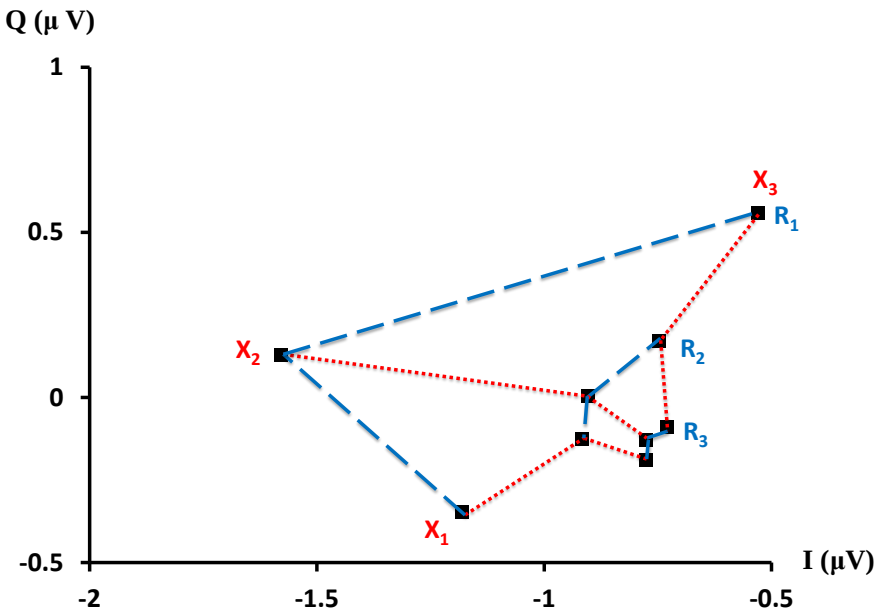

(a) 902 MHz

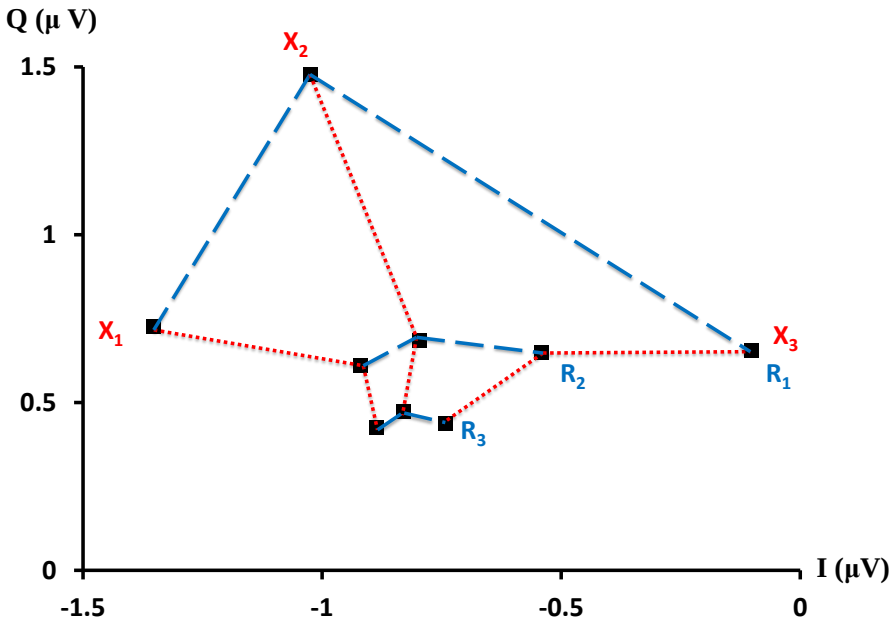

(b) 915 MHz

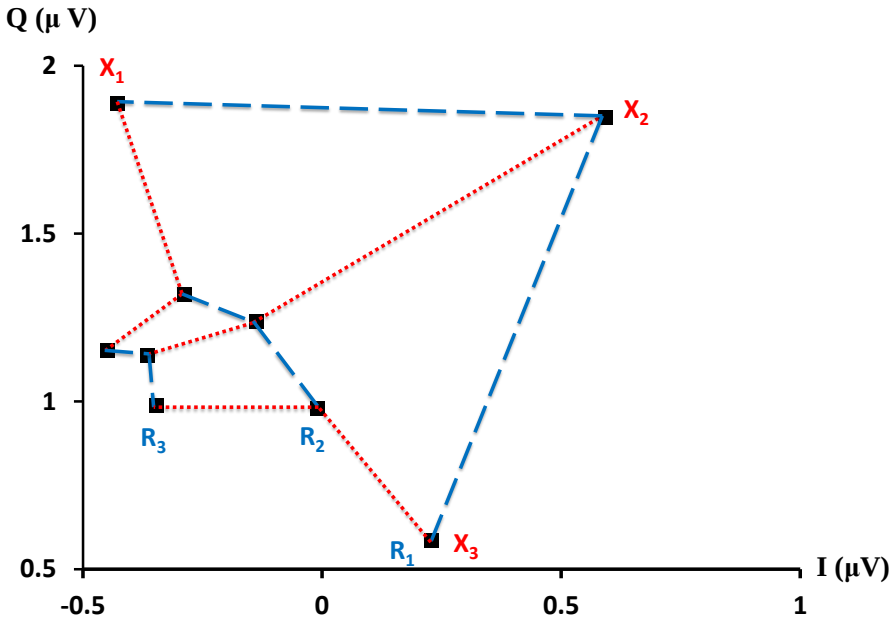

(c) 928 MHz

Figure 2.32. Measurement of vector backscattered signals from the tag coupled to various loads, each load composed of one resistive and one reactive component in series. The blue dash lines represent the constant resistive; the red dot lines represent the constant reactive loads.

Table 2-1. Resistive and reactance Loads

R_1	R_2	R_3
50 Ω	510 Ω	1000 Ω
X_1	X_2	X_3
-290Ω (0.6pF)	0	293 Ω (51 nH)

This work has demonstrated the method of coupling passive sensors on existing UHF RFID tags. Coupling passive sensor data to existing UHF RFID tags explores the possibility for low volume applications without designing a new tag ASIC. The existing UHF RFID system can be used to convey additional data by overlaying a coupling loop on the tag antenna and modulating vector backscatter. The design of the RFID passive sensor prototype is presented and the feasibility of this approach is demonstrated by the experimental results of the vector backscattered signals. The vector backscattered signal and the complex loads has presented the operation principle of the RFID passive sensor. The experimental results of the one-to-one mappings of the backscattering vectors and corresponding impedances have been obtained. With two reference impedances, the complex load of the passive sensor can be uniquely determined in noisy environments.

Chapter 3 Vector Backscattering from Planar Dipole Antenna with Complex Loads

3.1 Introduction

Scattering antenna theory has been studied for several decades [29–31], [35], [55]. The backscattering of a scattering antenna carries the properties of the connected load, and the backscattered wave is used for wireless sensing and communication. Based on this technique, the passive ultra-high-frequency radio frequency identification (UHF RFID) system is developed for wireless data access and widely applied in diverse fields, such as supply chain management, access and control, healthcare, and real-time location systems (RTLS) [1].

In a passive UHF RFID system, a reader initiates the communication with a tag (or a transponder) by transmitting out an electromagnetic wave, and the tag responds by conducting the backscattered modulation. The amplitude and the phase of the backscattering are manipulated by switching the tag's load impedance for the amplitude-shift keying (ASK) and the phase-shift keying (PSK) digital modulation schemes, respectively. In fact, both amplitude and phase are modulated in most of the passive UHF RFID tags. The potential of the vector backscattering modulation for pursuing better performances is revealed in [54], [56].

The radar cross-section (RCS) of a UHF RFID tag, which is proportional to the square of the amplitude of the backscattered wave, is described in [33], [34]. The relation between the amplitude of the backscattering and the load of the scattering antenna is established; however, the phase has not been thoroughly researched for an analytical description.

We review three backscattering-related equations and derive the equations for the amplitude of the backscattered electric field and backscattered voltage signal. The proposed models of the phase of the backscattered electric field and backscattered voltage signal are presented. The orientation effect and the polarization effect are incorporated in the vector backscattering model equations. A planar dipole antenna, which is designed as a scattering antenna with a resonant frequency located in the UHF band, is used in modeling, simulation, and

experiment. The three characteristic parameters of the scattering antenna, which are primary elements in the vector backscattering model equations, are obtained.

The simulated vector backscattered electric fields and the amplitudes and phases of the fields deviated from the model are presented. The environmental effect, the oriental effect, and the polarization effect are studied and presented with simulation results. Good consistency between the simulation outcomes and the model-predicted results is demonstrated. The experiment results of the vector backscattered voltage signals and the amplitudes and phases of the voltage signals deviated from the model are also presented, when the propagation loss factor and the propagation phase shift factor are included.

3.2 Vector Backscattering Model

Scattering happens when a wave propagates with the presence of an object (scatterer). The radar cross section (RCS), σ, characterizes the scattering property of a scatterer in the far field and it is defined as the equivalent area capturing and reradiating the incident energy isotropically.

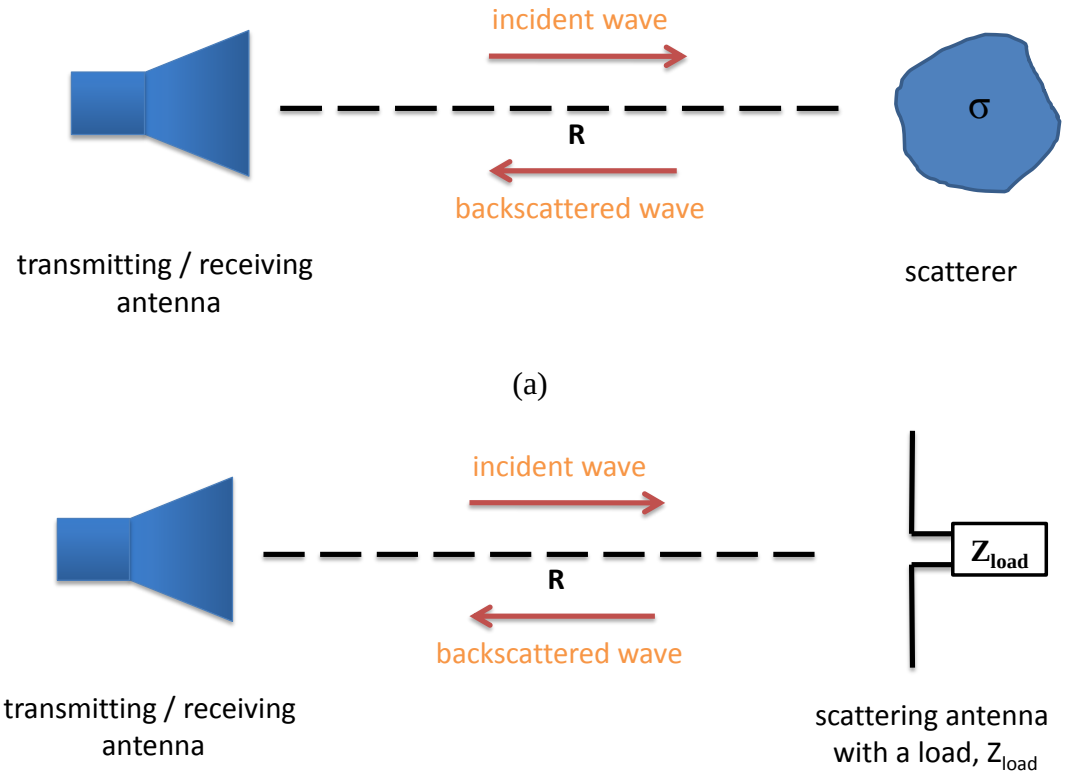

Figure 3.1. Backscattering of (a) a scatterer (b) a loaded scattering antenna.

Backscattering is the special case of scattering for a radar system in which transmitter and receiver are collocated. Backscattered RCS, σ_{BS}, is a function of the incident energy and the backscattered energy, as described in the equation (1.1).

3.2.1 Backscattered Electric Field

The general form of the backscattered RCS, σ_{BS}, of a loaded antenna is

$$\sigma_{BS} = \frac{\lambda^2}{4\pi}\left|\hat{p}_i \cdot \hat{p}_{ant}\right|^2 G_{SA}(\theta,\phi)^2 \left|\frac{Z_L - Z_A^*}{Z_L + Z_A} - A_S\right|^2 = \frac{\lambda^2}{4\pi}\left|\hat{p}_i \cdot \hat{p}_{ant}\right|^2 G_{SA}(\theta,\phi)^2 \left|\Gamma_m - A_S\right|^2 \qquad (3.1)$$

where

λ	=	wavelength of the incident/backscattered wave
$\left\|\hat{p}_i \cdot \hat{p}_{ant}\right\|$	=	polarization matching factor
$G_{SA}(\theta,\phi)$	=	scattering antenna gain
A_S	=	structure mode vector (load-independent structural mode scattering complex parameter)
Z_L	=	load impedance of the scattering antenna
Z_A	=	input impedance of the scattering antenna
Γ_m	=	modified reflection coefficient

To be focused on the analysis of the relation between the vector backscattering and the load impedance, the equation of the backscattered RCS, σ_{BS}, of a loaded antenna with polarization-matching (polarization matching factor = 1) and front-facing incidence ($G_{SA0} = G_{SA}(\theta = 0°, \phi = 0°)$) is simplified as

$$\sigma_{BS} = \frac{\lambda^2}{4\pi} G_{SA0}{}^2 \left|\frac{Z_L - Z_A^*}{Z_L + Z_A} - A_S\right|^2 = \frac{\lambda^2}{4\pi} G_{SA0}{}^2 \left|\Gamma_m - A_S\right|^2 \qquad (3.2)$$

Combining (1.1) and (3.2) and rearranging for the amplitude of the backscattered electric field gives

$$\left|\overrightarrow{E_{BS}}\right| = \frac{\lambda}{4\pi R} G_{SA0} \left|\Gamma_{BS}\right| \cdot \left|\overrightarrow{E_{INC}}\right| \tag{3.3}$$

$$\Gamma_{BS} = A_S - \Gamma_m = A_S - \frac{Z_L - Z_A^*}{Z_L + Z_A} \tag{3.4}$$

where Γ_{BS}, which is the vector between A_S and Γ_m, is defined as the backscattering coefficient. Because σ_{BS} is used to describe the strength of the backscattered wave, the derived equation (3.3) does not include any information for the phase of the backscattered wave. The amplitude of the backscattered electric field is fully described in (3.3), but the phase of the backscattered electric field is not provided.

The frequency-dependent constant phase model is proposed to formulize the phase of the backscattering from a loaded antenna. In this model, the phase of the backscattered electric field, θ_{EBS}, and the phase of the backscattering coefficient, $\theta_{\Gamma BS}$, are assumed to be in a constant phase difference for one scattering antenna in one single frequency, as follows,

$$\theta_{EBS} = \theta_{\Gamma BS} + \theta_0 \tag{3.5}$$

where θ_0 is field phase difference constant. In (3.3) and (3.5), both of the amplitude and the phase of the backscattered electric field are provided for describing the vector backscattering of an antenna with a complex load. Since the vector backscattering model is derived from the backscattered RCS equation (3.2), equation (3.3) is valid only when the far-field conditions are satisfied; the polarization is matched; and the front-facing incidence is made. This model will be verified by the simulation results in different scenarios and experiment results.

3.2.2 Backscattered Voltage Signal

The backscattered electric field is measured when it is transduced by an antenna and fed into an instrument as a current or voltage signal. The radar range equation [27] describes the ratio of the received power of backscattered and the transmitted power as

$$\frac{P_{BS}}{P_t} = \sigma_{BS} \frac{G_{TR}^2}{4\pi} \left(\frac{\lambda}{4\pi R^2}\right)^2 \tag{3.6}$$

$$P_t = \frac{\left|\overrightarrow{V_{TX}}\right|^2}{2Z_0} \tag{3.7.1}$$

$$P_{BS} = \frac{\left|\overrightarrow{V_{BS}}\right|^2}{2Z_0} \tag{3.7.2}$$

where the V_{TX} and V_{BS} are transmitted and backscattered voltage signals; G_{TR} is the gain of the transmitting/receiving antenna. Substituting (3.6), (3.7.1) and (3.7.2) into (3.2) leads to the amplitude of the backscattered voltage signal expressed as

$$\left|\overrightarrow{V_{BS}}\right| = \left(\frac{\lambda}{4\pi R}\right)^2 G_{TR} G_{SA0} A_C \cdot \left|\overrightarrow{V_{TX}}\right| \cdot \left|\Gamma_{BS}\right| \tag{3.8}$$

In (3.8), the amplitude compensation factor, A_C, is added and it accounts for the propagation attenuation which is not included in the situation described by the radar range equation. Like the phase of the backscattered electric field, the phase of the backscattered voltage signal is missed in the derived equation (3.8). To formulize the phase of the backscattered voltage signal from a loaded antenna, the same principle of the frequency-dependent constant phase difference is applied, resulting in

$$\theta_{VBS} = \theta_{\Gamma BS} + \theta_0 + \theta_C \tag{3.9}$$

where the phase of the backscattered voltage signal, θ_{VBS}, and the phase of the backscattering coefficient, $\theta_{\Gamma BS}$. In the backscattered voltage signal model, θ_{VBS} and $\theta_{\Gamma BS}$ are assumed to be in a constant phase difference for one scattering antenna in one single frequency; the voltage signal phase difference constant is comprised of the field phase difference constant, θ_0, and the compensation phase, θ_C. The compensation phase is added for the phase of the propagation path in the actual experiments. With (3.8) and (3.9), both of the amplitude and the phase of the backscattered voltage signal are provided for fully describing the vector backscattering of a scattering antenna with a complex load.

3.3 Planar Dipole Antenna

This research is focused on the extended applications of the existing UHF RFID tags. The dipole structure is chosen since this antenna and its various derivatives, including meandered antennas, tip-loaded antennas, and folded antennas, form the majority of the UHF RFID tag antenna designs [28], [57–61]. The proposed model, which has been verified for planar dipole antennas, is expected to be valid for most of the UHF RFID tag antennas.

The practical challenges for the tag antenna design includes: cost, size, polarization, matching to the chip, and environmental effects [19], [57], [62]. A variety of tag antennas derived from the dipole antenna structure have been presented to meet these constraints. General approaches and concerns for RFID tag antenna design are listed below,

- The unit price of a tag is expected to be as low as 5 cents for high volume applications; therefore the planar structures which can be manufactured very efficiently by the printing technologies are popular for RFID tag antennas.
- A tag with a compact size is appealing in many applications as a dipole antenna resonating around 900 MHz needs to be about 16 cm long. To reduce the antenna size, several methods, like bending and folding antenna structures, have been presented.
- For a highly linearly polarized antenna, like a dipole antenna, almost no energy is transduced when the incident wave is cross polarized to a tag antenna. A circularly polarized reader antenna is commonly used to solve this problem but the transduced energy is sacrificed. Polarization diverse tag antenna is another solution and it is implemented by a dual-dipole structure design which is a combination of two dipole antennas.
- The power delivered to the chip is determined by the matching between the tag antenna and the chip. Most of the RFID tag chips are highly capacitive so the tag antenna needs to be inductive enough for a good matching. The tip-loading structure and the additional inductor portion are commonly used for the implementation.
- Tags are usually attached to objects when used for identifying these objects. Actually operation of the tag is affected by the attached or adjacent object and this environmental effect varies for different materials (difference dielectric constant). In

general, tags still work with the presence of the low-dielectric-constant (ε_r = 1 - 5) material, like paper and glass; however, tags may malfunction under environmental effects caused by high-dielectric-constant ($\varepsilon_r \approx 80$) material, like water, or by metal. This is one of the most active and challenging research topics in the RFID community. Based on author's knowledge, no specific tag antenna design provides a good solution for solving this problem completely. The environmental effect will be addressed in Section V.

A planar dipole-based antenna design can be cost-effective, compact-sized, diversely-polarized, and well-matched; these features make the dipole antenna and its various derivatives popular and representative for UHF RFID tag antenna designs. After the vector backscattering model and the wireless impedance measurement method are validated for UHF planar dipole antennas, the same approaches will be applicable for a majority of the UHF RFID tag derived from the dipole antenna structure.

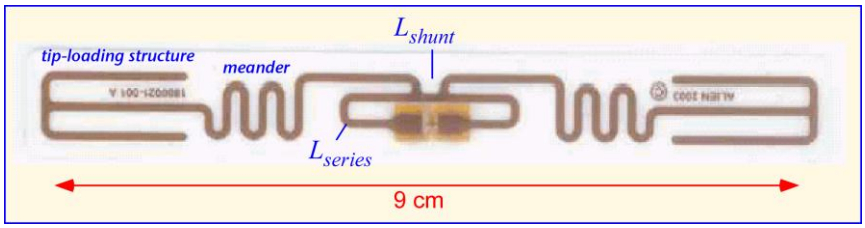

(a)

(b)

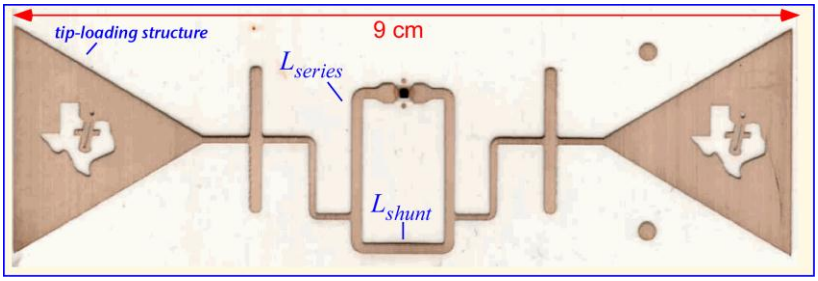

(c)

Figure 3.2. UHF RFID tag antenna designs: (a) Alien Technology (using tip loading, meandered lines, and additional inductor portions), (b) Symbol Technology (using dual dipoles), and (c) Texas Instruments (using tip-loading and additional inductor portions) [19].

When an antenna operates as a scattering antenna, it is characterized by the following three parameters: the input impedance, Z_A, the antenna gain, G_{SA}, and the structure mode vector, A_S (a complex parameter represents the RCS component which is load-independent). These three scattering antenna characterization parameters play key roles for the studies of the backscattering from a loaded antenna. In other words, the proposed models can predict the vector backscattering from a scattering antenna when the load impedance and the scattering antenna characterization parameters are provided.

A planar dipole antenna is designed for operating in the UHF band and used in simulations and experiments to verify the proposed equations of the vector backscattering from a loaded antenna. This UHF planar dipole antenna fabricated on an FR4 substrate is designed as a scattering antenna and the resonant frequency is within the frequency band from 800 MHz to 1200 MHz. The layout and the dimension of the UHF planar dipole antenna are shown in Figure 3.3 and listed in Table 3-1.

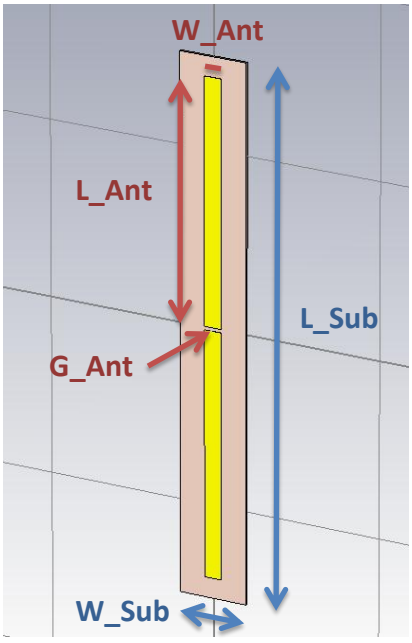

Figure 3.3. UHF planar dipole antenna.

Table 3-1. Planar dipole antenna layout parameters.

Parameter	Description	Dimension (mm)
G_Ant	Gap of antenna	1.0
L_Ant	Length of antenna	70.0
W_Ant	Width of antenna	5.0
T_Ant	Thickness of antenna	0.1
L_Sub	Length of antenna substrate	152.0
W_Sub	Width of antenna substrate	20.0

Among the three scattering antenna characterization parameters, the input impedance of the antenna, Z_A, can be obtained accurately by a EM simulation tool. The UHF planar dipole antenna is constructed and simulated in CST Microwave Studio for both of the real part and imaginary part of Z_A within frequency ranged from 800 MHz to 1200 MHz, as shown in Figure 3.4.

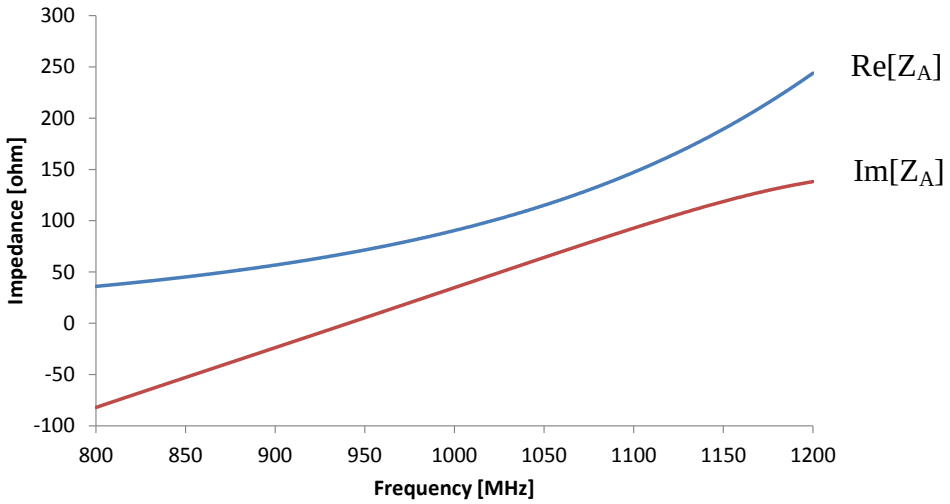

Figure 3.4. Simulation result of the input impedance of the planar dipole antenna.

With the simulation result of Z_A, the structure mode vector, A_S, and the antenna gain, G_{SA}, can be determined graphically or analytically with three simulated σ_{BS} which corresponds to three arbitrarily loads. The planar dipole antenna characterization parameters within the frequency of interest (800MHz -1200MHz) are listed in Table 3.2.

Table 3-2. Planar dipole antenna characterization parameters.

Frequency (MHz)	Z_A (Ω)	A_S	G_{SA}
800	36.6 - 77.2j	0.99 + 0.18j	1.55
900	58.0 – 19.9j	0.97 + 0.28j	1.57
1000	92.2 + 38.2j	0.91 + 0.42j	1.62
1100	152.1 + 97.1j	0.78 + 0.62j	1.67
1200	259.5 + 138.6j	0.49 + 0.88j	1.70

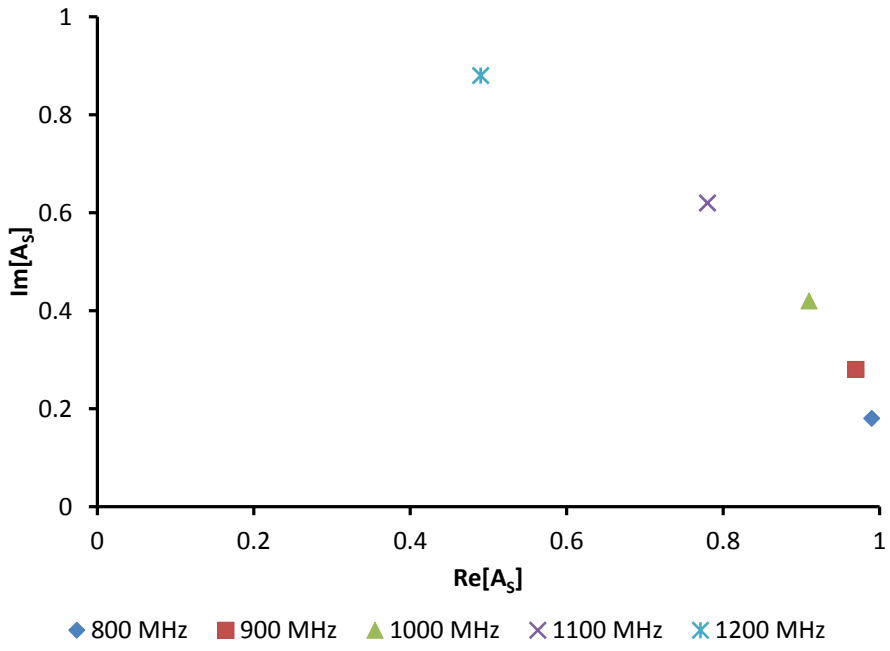

Figure 3.5. Simulation result of the structural mode vector, A_S. Frequency: 800 – 1200 MHz.

3.4 Loads under Test

The loads under test are categorized into open, Z_{LR}, and Z_{LC}. Open load represents for connecting nothing as infinite impedance. Z_{LR} is a set of five resistive loads: [0Ω, 50Ω, 75Ω, 100Ω, 125Ω]. The impedances and the modified reflection coefficients of five Z_{LR}s at frequencies of interest are listed in Table 3-3 and Table 3-4.

Z_{LC} is a set of five complex loads with corresponding Γ_m approximate to 0, +0.5, +0.5j, -0.5, -0.5j at 1000MHz: [100Ω + 4.5pF, 280Ω + 4.5pF, 53.6Ω + 6.3nH, 30.1Ω + 4.5pF, 53.6Ω + 1.5 pF], as listed in Table 3-5. The impedances and the modified reflection coefficients of five Z_{LC}s at frequencies of interest are listed in Table 3-6 and Table 3-7

Table 3-3. Resistive loads under test.

	Z_{LR1}	Z_{LR2}	Z_{LR3}	Z_{LR4}	Z_{LR5}
Impedance (Ω)	0	50	75	100	125

Table 3-4. Modified reflection coefficient of resistive loads under test.

Frequency (MHz)	Z_{LR1}	Z_{LR2}	Z_{LR3}	Z_{LR4}	Z_{LR5}
800	0.68 – 0.73 j	0.56 – 0.42 j	0.58 – 0.31 j	0.61 – 0.23 j	0.65 – 0.18 j
900	-0.69 – 0.72 j	-0.01 – 0.23 j	0.17 – 0.15 j	0.29 – 0.11 j	0.39 – 0.08 j
1000	-0.75 + 0.67 j	-0.22 + 0.30 j	-0.05 + 0.22 j	0.08 + 0.17 j	0.18 + 0.13 j
1100	-0.44 + 0.90 j	-0.23 + 0.57 j	-0.13 + 0.47 j	-0.05 + 0.39 j	0.03 + 0.33 j
1200	-0.52 + 0.85 j	-0.36 + 0.64 j	-0.29 + 0.26 j	-0.23 + 0.49 j	-0.16 + 0.43 j

Table 3-5. Complex loads under test.

	Z_{LC1}	Z_{LC2}	Z_{LC3}	Z_{LC4}	Z_{LC5}
Resistance (Ω)	100	280	54	30	54
Reactance	4.5 pF	4.5 pF	6.3 nH	4.5 pF	1.5 pF

Table 3-6. Impedance (Ω) of complex loads under test.

Frequency (MHz)	Z_{LC1}	Z_{LC2}	Z_{LC3}	Z_{LC4}	Z_{LC5}
800	100 – 44.2 j	280 – 44.2 j	53.6 + 31.7 j	30.1 – 44.2 j	53.6 – 132.6 j
900	100 – 39.3 j	280 – 39.3 j	53.6 + 35.6 j	30.1 – 39.3 j	53.6 – 117.9 j
1000	100 – 35.4 j	280 – 35.4 j	53.6 + 39.6 j	30.1 – 35.4 j	53.6 – 106.1 j
1100	100 – 32.2 j	280 – 32.2 j	53.6 + 43.5 j	30.1 – 32.2 j	53.6 – 96.5 j
1200	100 – 29.5 j	280 – 29.5 j	53.6 + 47.5 j	30.1 – 29.5 j	53.6 – 88.4 j

Table 3-7. Modified reflection coefficient of complex loads under test.

Frequency (MHz)	Z_{LC1}	Z_{LC2}	Z_{LC3}	Z_{LC4}	Z_{LC5}
800	0.72 – 0.26 j	0.80 – 0.08 j	0.39 – 0.34 j	0.77 – 0.45 j	0.88 – 0.28 j
900	0.38 – 0.25 j	0.67 – 0.06 j	-0.02 + 0.11 j	0.15 – 0.62 j	0.61 – 0.50 j
1000	0.05	0.51	+0.51 j	-0.50	-0.50 j
1100	-0.13 + 0.27 j	0.32 + 0.10 j	-0.01 + 0.68 j	-0.49 + 0.51 j	-0.47 – 0.03 j
1200	-0.30 + 0.41 j	0.10 + 0.18 j	-0.19 + 0.73 j	-0.54 + 0.61 j	-0.60 + 0.26 j

3.5 Simulation Results

In this section, the simulation results of the electric field backscattered from a loaded antenna are provided in different scenarios:

- polarization-matching and front-facing incidence in the far-field region;
- polarization-matching and front-facing incidence in the non-far-field region;
- non-polarization-matching and front-facing incidence in the far-field region;
- non-front-facing incidence in the far-field region;
- polarization-matching and front-facing incidence in the far-field region with the presence of an object.

To validate the equations (3.4) and (3.5) of the backscattered electric field of a scattering antenna with a complex load, a planar dipole antenna with various resistive and complex loads is constructed and simulated in the CST Microwave Studio. In the simulation, vacuum is the propagation medium; an ideal sinusoidal planar wave source is set as the incident wave source; the polarization of the incident field and the dipole antenna are matched; the wavefront of the incident field is aligned with the front plane of the dipole antenna; the planar dipole antenna is set as the scattering antenna and modeled with the parameters listed in Table 3-1.

The far-field region are determined by the maximum extent of an antenna, D, the distance between the dipole antenna and the observation point, R, and the wavelength, λ; the far-filed conditions are defined and summarized as follows [63]:

- $R > \frac{2D^2}{\lambda}$
- $R >> D$
- $R >> \lambda$

For the planar dipole antenna used in this case, the maximum extent of an antenna, D, is less than the wavelength, λ. Therefore, the far-field conditions are fulfilled when the distance between the dipole antenna and the observation point, R, is much larger than the wavelength, λ. When the far-field conditions are satisfied, the electromagnetic fields are in the TEM mode (transverse electromagnetic) in which electric field is perpendicular to magnetic field, and neither electric

nor magnetic field is in the direction of propagation. For far-field simulations, the distance between the dipole antenna and the observation point, R, is set much larger than the wavelength; for non-far-field simulations, the distance between the dipole antenna and the observation point, R, is set to be 700 mm which is around 2λ to 3λ within the frequency range between 800 MHz and 1200 MHz. In the experiment setting, the distance between the dipole antenna and the transmitting/receiving antenna is 700mm as well.

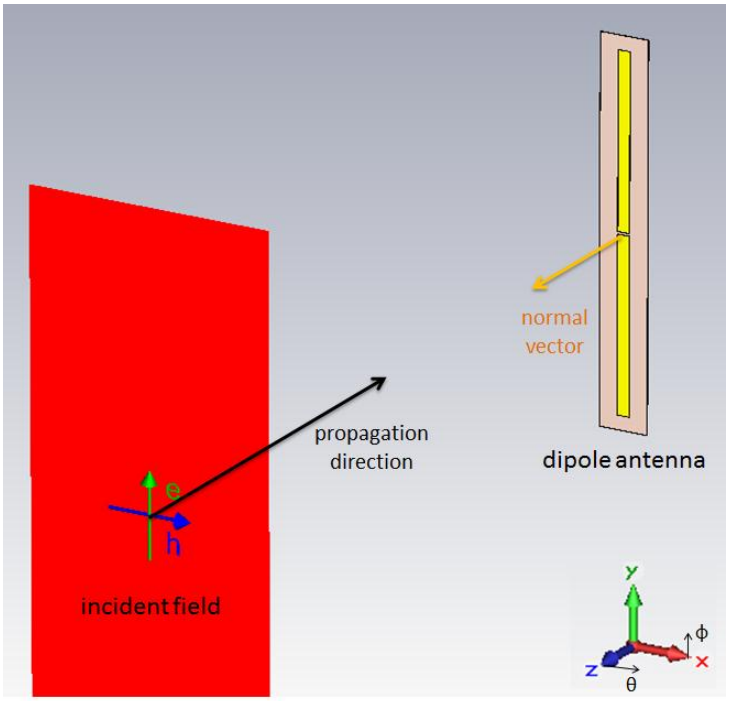

Figure 3.6. Simulation of the vector backscattering model for a planar dipole antenna with polarization-matching and front-facing incidence

The incident field is set as a linearly polarized plane wave propagating along -Z-axis: the electric field is on Y-axis; the magnetic field is on X-axis. The tilted angle is defined as the angle deviated from the Y-axis toward the X-axis for identifying the polarization of the incident field. As indicated in Figure 3.6, the polarization matching is achieved by setting the tilted angle = 0°. The polarization effect will be presented later when the tilted angle varies from 0° to 90° (i.e. the polarization of the incident field rotates from Y-axis to X-axis).

The dipole antenna sits on the XY-plane with its front surface facing toward the +Z-axis. The two arms of this dipole antenna extend along the Y-axis; therefore this antenna strongly interacts with the fields polarized along Y-axis and hardly interacts with the fields polarized along the X-axis and Z-axis. The normal vector of the dipole antenna is defined as the unit vector perpendicular to the front surface of the antenna; in this case, the normal vector is identical to the unit vector of +Z-axis. In this case, the normal vector is equal to ($\theta = 0°$, $\phi = 0°$) where the front-facing incidence occurs. Later, the orientation effect will be illustrated by having different orientations of the antenna which is specified by the antenna normal vector in the spherical coordinate system with two parameters: θ and ϕ.

Again, the simplifications made for the vector backscattering model of a loaded dipole antenna with polarization-matching and front-facing incidence are: the tilted angle = 0° and the normal vector is ($\theta = 0°$, $\phi = 0°$). The simulation settings for this case are summarized and listed in Table 3-8.

Table 3-8. Simulation settings for the vector backscattering model with polarization-matching and front-facing incidence.

Frequency [GHz]	1.0
Load impedance [Ω]	Five different Z_{LR} / Z_{LC}
Incident field propagation vector	$-\hat{a}_z$ ($\theta = 180°$; $\phi = 0°$)
Polarization tilted angle [deg]	$+\hat{a}_y$ ($\theta = 90°$; $\phi = 90°$)
Antenna normal vector	$+\hat{a}_z$ ($\theta = 0°$; $\phi = 0°$)
Adjacent object	No

To quantify the error between the results of $|E_{BS}|$ from simulation and model, the simulation amplitude error ratio, $AERR_S$, is defined as

$$AERR_S = \left| \frac{\left|\overrightarrow{E_{BS}}\right|_S - \left|\overrightarrow{E_{BS}}\right|_M}{\left|\overrightarrow{E_{BS}}\right|_M} \right| \tag{3.10.1}$$

where, $|E_{BS}|_S$ is the simulated $|E_{BS}|$ and $|E_{BS}|_M$ is the model $|E_{BS}|$.

To quantify the error between the results of θ_{EBS} from simulation and model, the simulation phase error, PER_S, is defined as

$$PER_S = \left| \theta_{EBS,S} - \theta_{EBS,M} \right| \tag{3.10.2}$$

where, $\theta_{EBS,S}$ is the simulated θ_{EBS} and $\theta_{EBS,M}$ is the model θ_{EBS}. The simulation amplitude error ratio, $AERR_S$ and the simulation phase error, PER_S, of a loaded dipole antenna with polarization-matching and front-facing incidence for the five Z_{LR}s and the five Z_{LC}s in the far-field region and the non-far-field region are presented in Figure 3.7, Figure 3.8, Figure 3.9, and Figure 3.10.

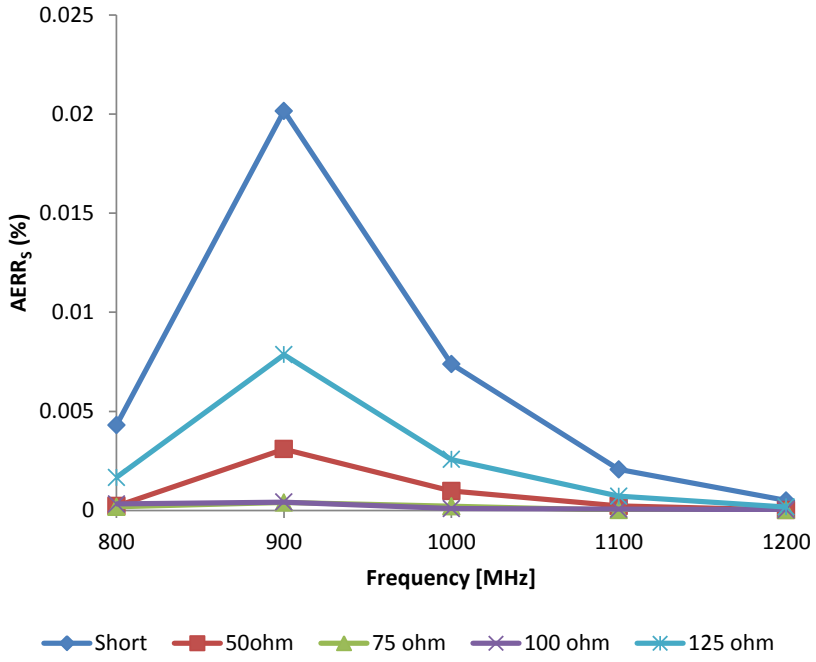

(a)

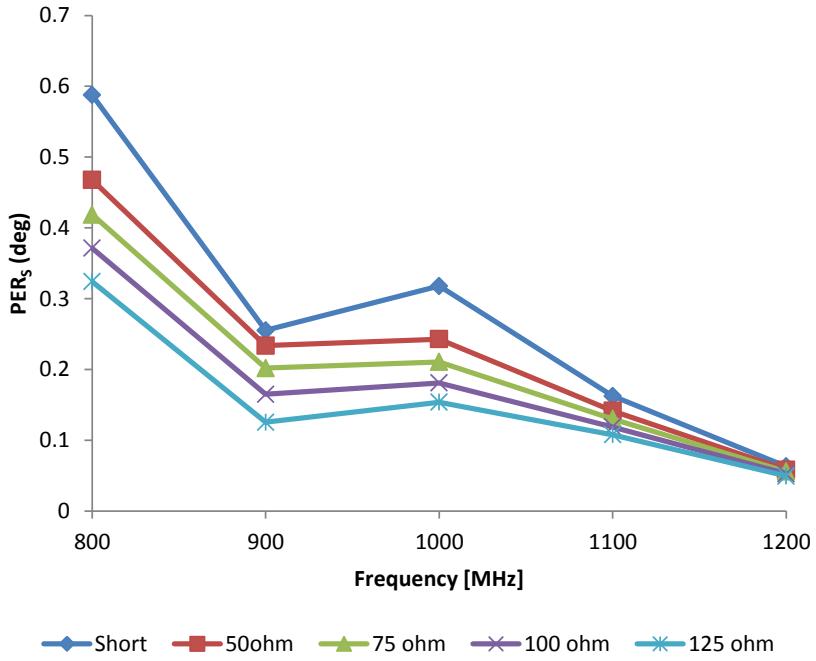

(b)

Figure 3.7. The far-field simulation error of the backscattered electric field of the scattering antenna loaded with Z_{LR}; (a) Amplitude: $AERR_S$ (b) Phase: PER_S.

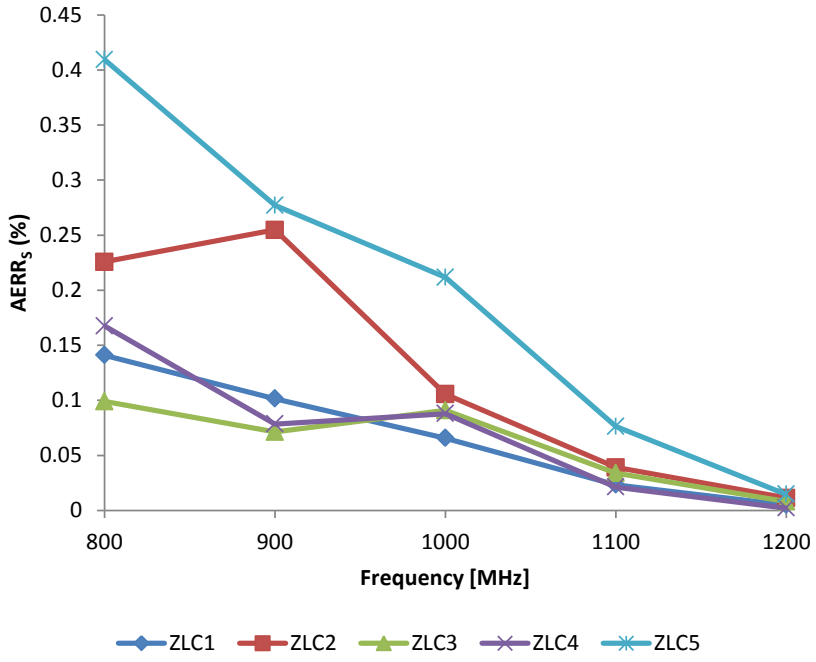

(a)

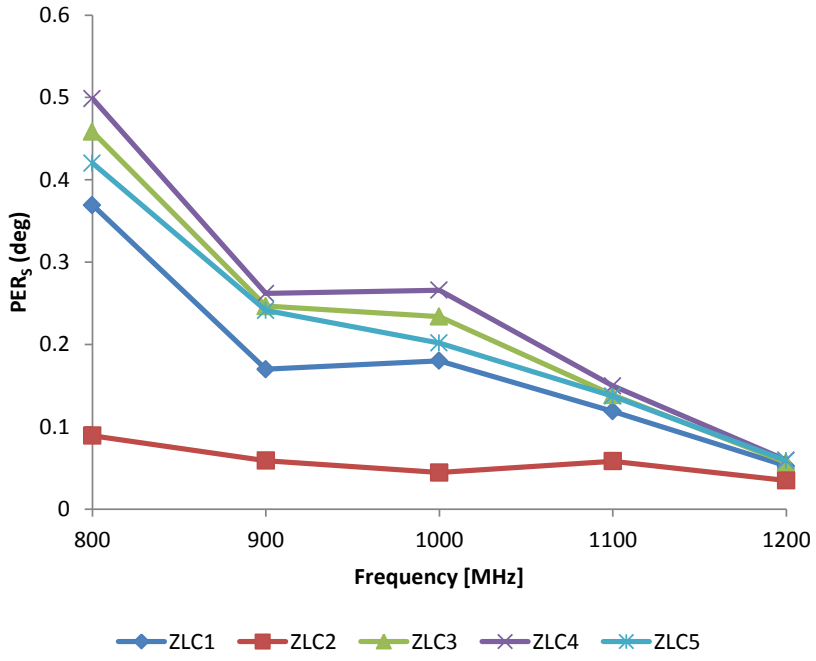

(b)

Figure 3.8. The far-field simulation error of the backscattered electric field of the scattering antenna loaded with Z_{LC}; (a) Amplitude: $AERR_S$ (b) Phase: PER_S.

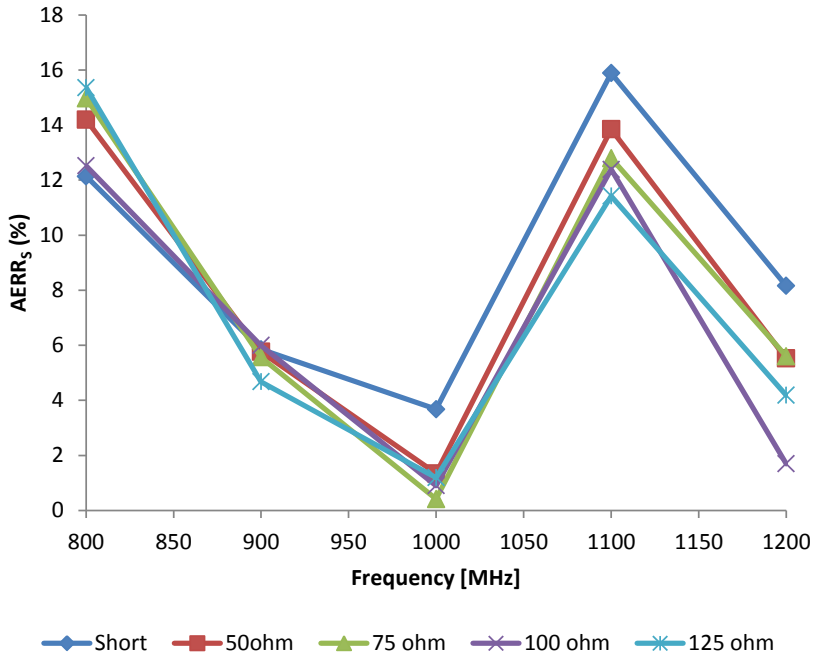

(a)

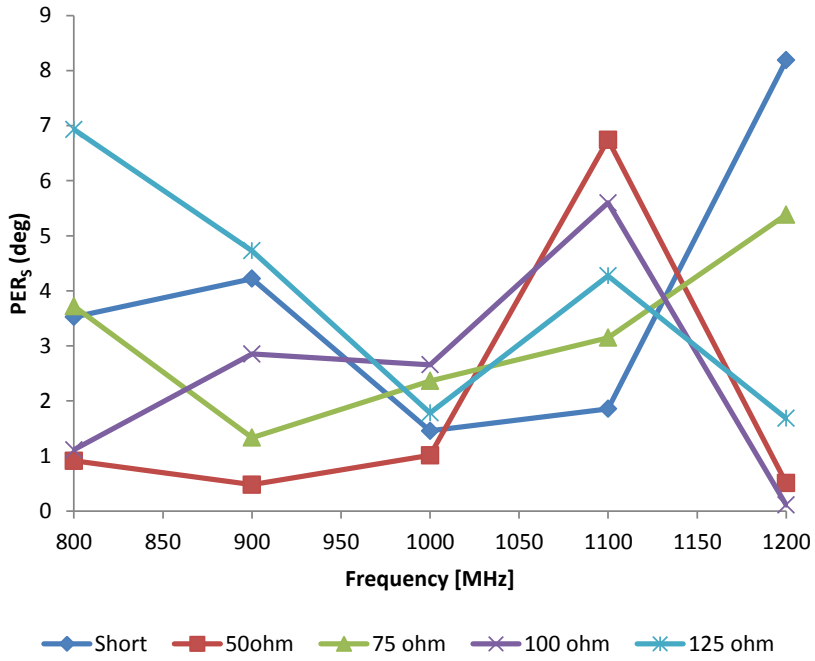

(b)

Figure 3.9. The non-far-field simulation error of the backscattered electric field of the scattering antenna loaded with Z_{LR}; (a) Amplitude: $AERR_S$ (b) Phase: PER_S.

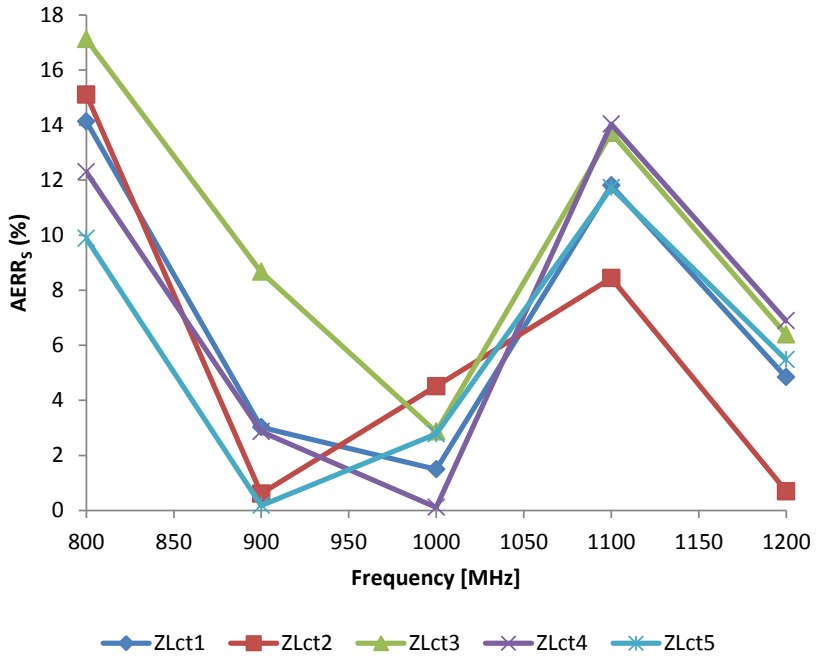

(a)

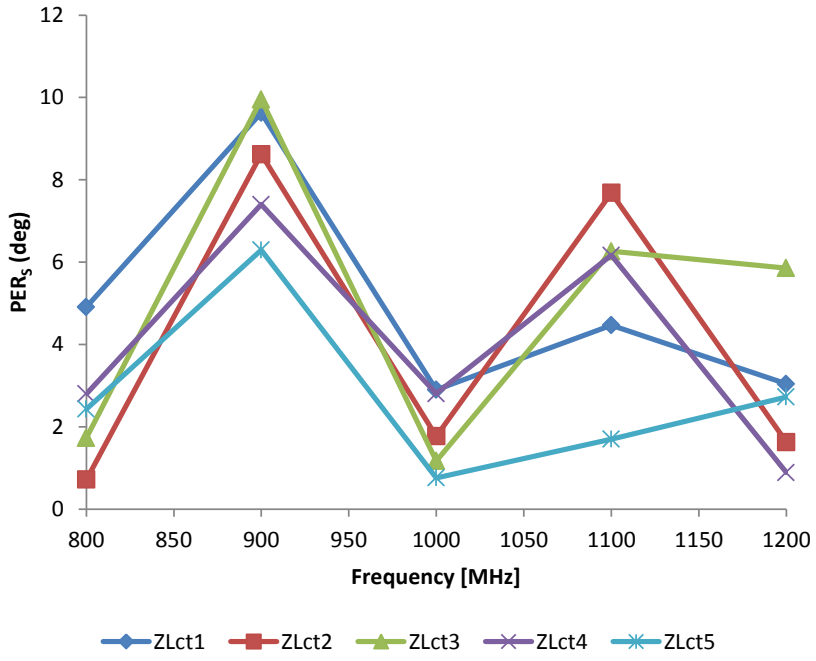

(b)

Figure 3.10. The non-far-field simulation error of the backscattered electric field of the scattering antenna loaded with Z_{LC}; (a) Amplitude: $AERR_S$ (b) Phase: PER_S.

The far-field simulation error of the backscattered electric field of the scattering antenna loaded with five Z_{LR} and five Z_{LC} for 800 MHz – 1200 MHz are presented in Figure 3.7 and Figure 3.8. For $Z_{LR,}$ the maximum $AERR_S$ and PER_S are less than 0.02% and 0.6 degree respectively; for $Z_{LC,}$ the maximum $AERR_S$ and PER_S are less than 0.45% and 0.6 degree respectively through the whole frequency range. These simulation results show high accuracy of the vector backscattering model in the far-field region.

The non-far-field simulation error of the backscattered electric field of the scattering antenna loaded with five Z_{LR} and five Z_{LC} for 800 MHz – 1200 MHz are presented in Figure 3.9 and Figure 3.10. For $Z_{LR,}$ the maximum $AERR_S$ and PER_S are about 16% and 8.0 degree respectively; for $Z_{LC,}$ the maximum $AERR_S$ and PER_S are about 17% and 10.0 degree respectively through the whole frequency range. The vector backscattering model predicts the simulation results in the non-far-field region with lower accuracy.

As presented in the previous section, the vector backscattering model is valid only when the far-field conditions are satisfied; the polarization is matched; and the front-facing incidence is made. When the distance between the observation point and the antenna under test was only two or three times the wavelength and the far-field conditions were not sufficiently achieved. As a result, the model cannot very precisely predict the simulation results. The comparison between the far-field and the non-far-field simulation results are presented in Table 3-9 (the $AERR_S$ and PER_S are averaged through five frequencies and five load impedances).

Table 3-9. Averaged $AERR_S$ and PER_S for far-field and non-far-field simulations.

	Far-field: R >> λ		**Non-far-field: R = 2~3λ**	
Average	**Z_{LR}**	**Z_{LR}**	**Z_{LR}**	**Z_{LC}**
$AERR_S$ (%)	0.002	0.002	7.8	7.2
PER_S (deg)	0.2	0.2	3.1	4.2

3.5.1 Polarization and Orientation Effects

Beforehand, some simplifications were made, and polarization mismatch and orientation of the antenna were not taken into account. In reality, the polarization and the angle of the incident electromagnetic wave transmitted from the reader could be arbitrary with respect to a tag. After validating the vector backscattering model for the simplified case (polarization-matching and front-facing incidence), this model will be extended for considering the polarization effect and the orientation effect.

When the polarization effect and the orientation effect are taken into consideration, the equation of the amplitude of the backscattered field is rewritten as

$$\left|\overrightarrow{E_{BS}}\right| = \frac{\lambda}{4\pi R}\left|\hat{p}_i \cdot \hat{p}_{ant}\right| G_{SA}(\theta,\phi)\left|\Gamma_{BS}\right| \cdot \left|\overrightarrow{E_{INC}}\right| \tag{3.11}$$

where the polarization matching factor is included and the antenna gain becomes a function of its orientation. It is worth noting that the phase of the backscattered electric field is the same as equation (3.5), and is unaffected by the polarization and the orientation.

In the study of the polarization effect, each simulation setting is kept the same except that the polarization of the incident wave rotates from Y-axis to Z-axis (i.e. the tilted angle varies from 0° to 90°), as shown in Table 3-10. According to the equation (3.11), the amplitude of the backscattered field is proportional to the polarization matching factor which is determined by the polarization of the incident field when the antenna polarization is fixed. In fact, the polarization matching factor is the sine function of the tilted angle. As a result, the backscattered RCS is predicted to be proportional to the square of the sine function of the tilted angle. In other words, when the tilted angle increases, the backscattered RCS gradually decreases.

Table 3-10. Simulation settings for the vector backscattering model for polarization effect.

Frequency [GHz]	1.0
Load impedance [Ω]	∞
Incident field propagation vector	$-\hat{a}_z$
Polarization tilted angle [deg]	0°, 15°, 30°, 45°, 60°, 75°, 90°
Antenna normal vector	$+\hat{a}_z$ ($\theta = 0°; \phi = 0°$)
Adjacent object	No

The simulation results have a great agreement with the model prediction, as shown in Figure 3.11 (a), except for the case of tilted angle = 90° where the model predicted backscattered RCS is 0 (-∞ dBsm). When the incident wave is cross polarized (X-axis polarized in this case), non-zero but small Y-axis polarized field (backscattered RCS is less than -100 dBsm) is generated and backscattered since the dipole antenna is not perfectly linear polarized along Y-axis.

On the other hand, the phase of the backscattered field is expected to be unchanged. As shown in Figure 3.11 (b), the phases of the y-component of the backscattered field are constant except for the case of tilted angle = 90° where a small Y-axis polarized backscattered field is inducted by the X-axis polarized incident field. In conclusion, the vector backscattering model can precisely predict the polarization effect on the vector backscattered fields except for the extreme case in which the incident field is exactly cross-polarized to the antenna polarization.

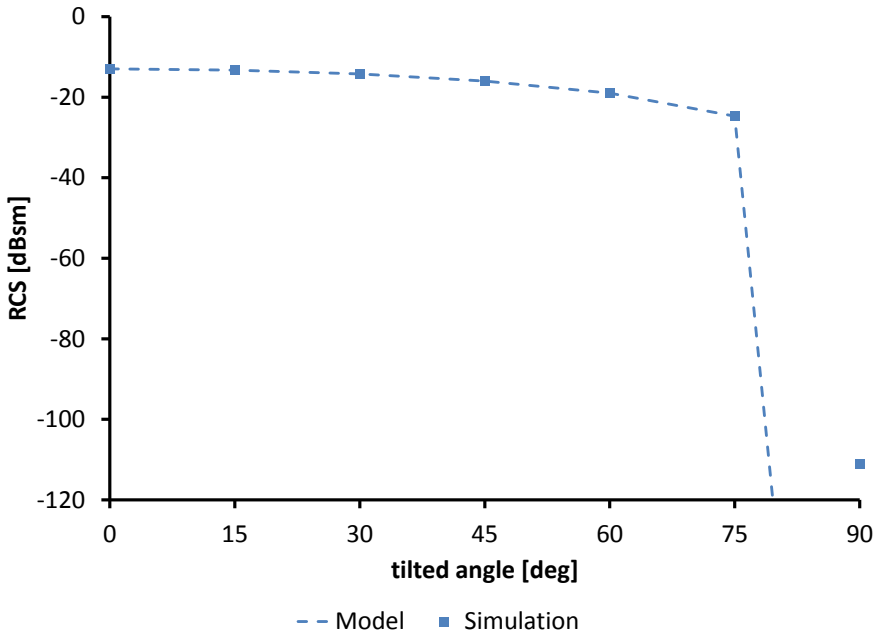

(a)

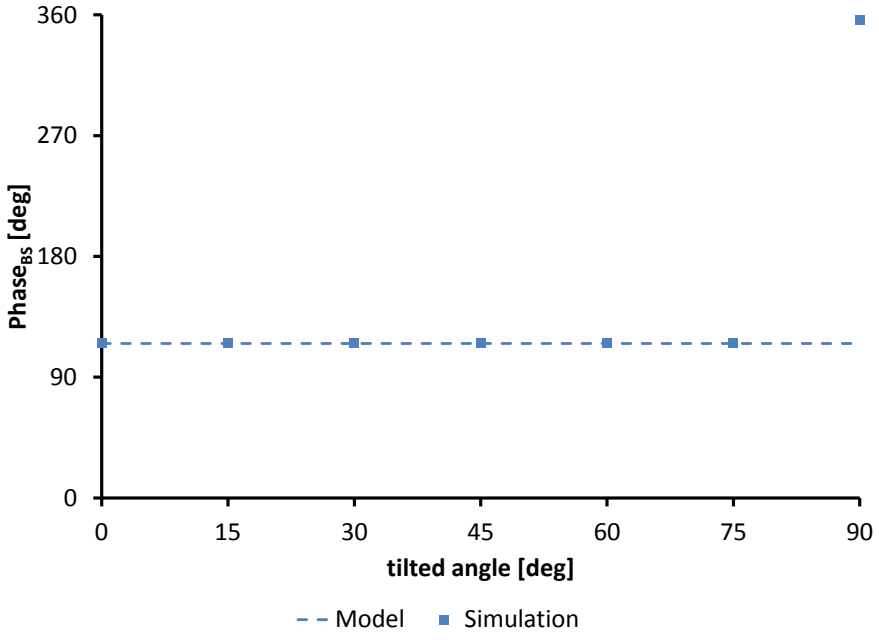

(b)

Figure 3.11. The model-predicted results and simulation results of the vector backscattering of a dipole antenna with different tilted angles.

In the study of the orientation effect, all the simulation settings are kept the same except that the antenna normal vector is set in the range: θ = 0° - 180° and ϕ = 0° - 90°, as shown in Table 3-11.

Table 3-11. Simulation settings for the vector backscattering model for orientation effect.

Frequency [GHz]	1.0
Load impedance [Ω]	∞
Incident field propagation vector	$-\hat{a}_z$
Polarization tilted angle [deg]	$+\hat{a}_y$
Antenna normal vector	θ = 0°, 30°, 60°, 90°, 120°, 150°, 180° ϕ = 0°, 15°, 30°, 45°, 60°, 75°, 90°
Adjacent object	No

The spherical surface surrounding the dipole antenna is formed when θ and φ are ranged from 0 to 180° and from 0 to 360° respectively. Because the antenna structure is symmetric to XZ-plane and YZ-plane, only one-fourth portion of the whole spherical surface needs to be considered. Therefore, φ is ranged from 0° to 90° rather than being ranged from 0° to 360°.

Based on the equation (3.11), the amplitude of the backscattered field is proportional to not only the incident field projected on the antenna polarization (Y-axis) but also the gain of the antenna. Actually, both these are dependent on the antenna orientation which is described by the antenna normal vector. The Y-component of the incident field is the cosine function of ϕ; the gain of the antenna is a function of both θ and ϕ. Hence, when the different orientations of the antenna are applied, the amplitude of the backscattered field varies.

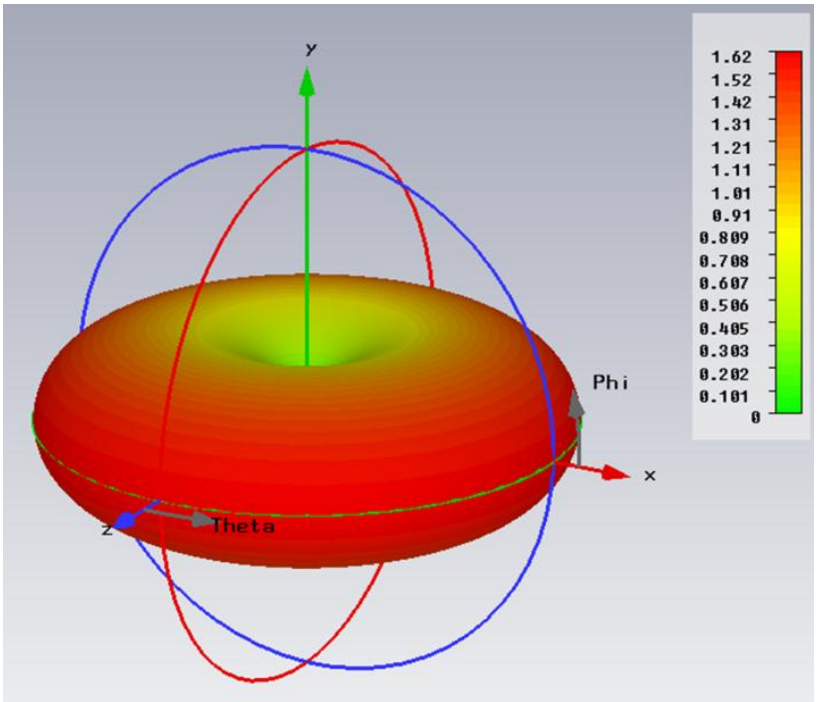

Figure 3.12. The field pattern of the dipole antenna.

The field pattern of this planar dipole antenna which is used to describe the gain at different directions is simulated and presented in figure 3.12. The donut shape field pattern is almost omnidirectional for theta variation and diminishes when phi increases. The model-predicted results and simulation results of the vector backscattering of a dipole antenna with different angles are presented in Figure 3.13. These two results are quite consistent for low ϕ and the errors between the simulation and the model increase when ϕ increases.

As indicated in the vector backscattering model equations, the phases of the backscattered field for different orientations are not changed. These statements are supported by the simulation results as shown in Figure 3.13 (b) except for $\phi = 90°$ where the y-component of the backscattered field drops to a negligible level.

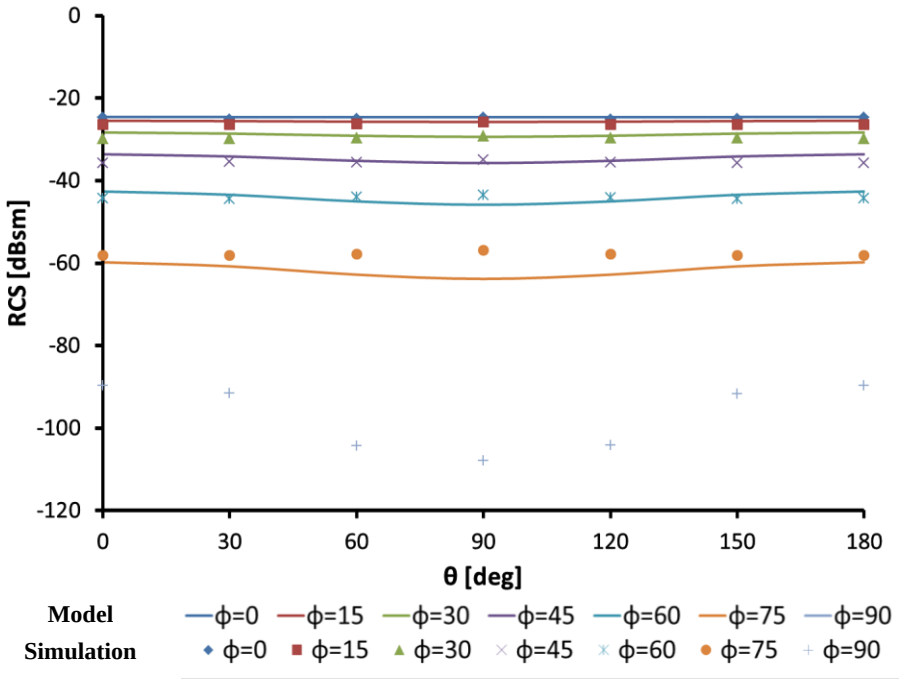

(a)

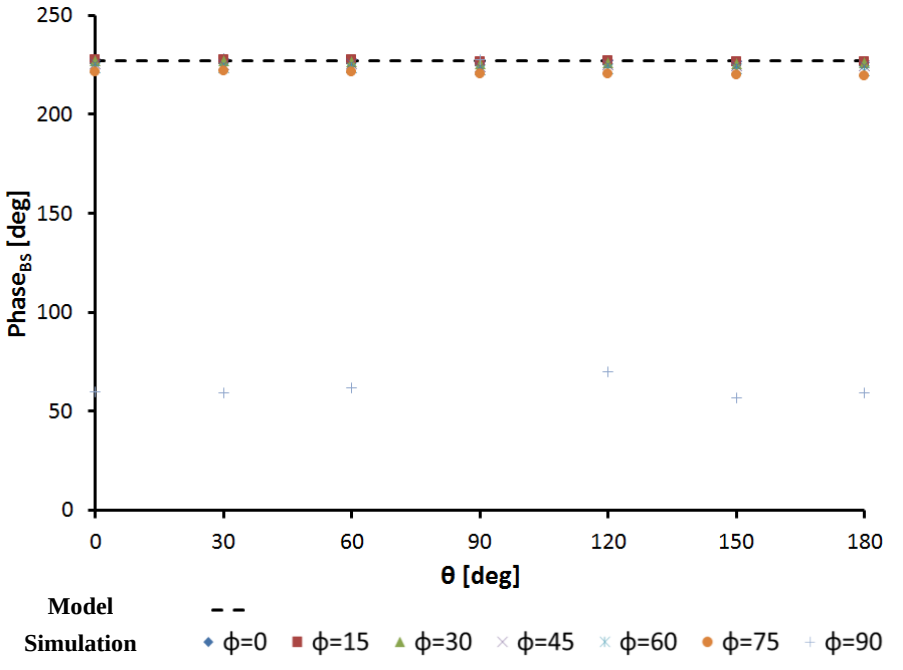

(b)

Figure 3.13. The model-predicted results and simulation results of the vector backscattering of a dipole antenna with different angles.

In conclusion, the vector backscattering model can accurately predict the polarization effect on the vector backscattered fields given the polarization of the incident wave and the orientation effect on the vector backscattered fields given the antenna field pattern and the incident angle. Since the amplitude of the backscattering is dependent on the polarization and the orientation of the antenna but the phase of the backscattering is not, only the backscattered power is affected by these two effects. Actually, backscattered power is also a function of the distance between a reader and a tag, and existing RFID systems work for various distances on condition that the power is higher than the sensitivity level of the reader. Therefore, the proposed vector backscattering modulation would work under the orientation effect because only the amplitude of the backscattered field is affected by the polarization and the orientation effect.

3.5.2 Environmental Effect

Previously the relation between the vector backscattering and the load impedance was illustrated. Some simplifications were made and applied for developing the vector backscattering model; they were: no surrounding effect, no polarization mismatch, and single angle incidence. In other words, nothing but the antenna under test standing in the free space was considered. Actually, a tag is normally attached to an object as an identifier and the performance is affected or deteriorated by the electromagnetic properties of the object.

Recently, research has presented different ways to improve the reliability of passive tags when placed on objects with different dielectric constant or metallic objects [64–69]. Any object adjacent to the antenna is treated as a new add-on of the antenna and consequently the character of the antenna, like input impedance, is modified. In this section, the environmental effect is referred to the effect caused by the presence of any object adjacent to the tag; it is a function of the shape and the dimensions of the object, and the distance between the antenna and the object. Moreover, the environmental effect also depends on the dielectric constant (relative permittivity) of the object.

In this section, the study is focused on the environmental effect caused by an adjacent object with the different dielectric constants. Research on the environmental effects of metal objects has presented in [67–69], and it is not in the scope of this study. Different materials have

different dielectric constants which vary as the temperature or the frequency change. Common materials in the real world are listed in Table 3-12 for their dielectric constants at room temperature and at 915 MHz.

Table 3-12. Dielectric constants for common materials at room temperature and 915 MHz [65].

Material	Dielectric Constant (ε_r)
Cardboard	≈ 1.0
Acrylic Slab	2.6
Pine Plywood	1.7
Ground Beef	50
Water	77

As shown in Figure 3.14, an additional adjacent object which is a square sheet is included in the simulation. This sheet is co-centered with the dipole antenna with no gap; the dimensions of this square sheet are set as: length = width = 76 mm (half of the length of the dipole antenna) and thickness = 1.5 mm (0.5% of the wavelength of 1 GHz). The dielectric constants of the square sheet are categorized into two sets: [1, 2, 3, 4, 5] and [1, 20, 40, 60, 80], as listed in Table 3-13.

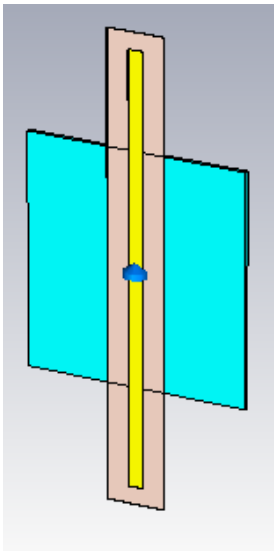

Figure 3.14. Simulation setting of the vector backscattering model for a planar dipole antenna with the presence of an object, a square sheet.

Table 3-13. Simulation settings for the vector backscattering model for environmental effects

Frequency [GHz]	1.0
Load impedance [Ω]	∞
Incident field propagation vector	$-\hat{a}_z$
Polarization tilted angle [deg]	$+\hat{a}_y$
Antenna normal vector	$+\hat{a}_z$ ($\theta = 0°; \phi = 0°$)
Adjacent object	Yes (a square sheet) dielectric constants: 1, 2, 3, 4, 5, 20, 40, 60, 80

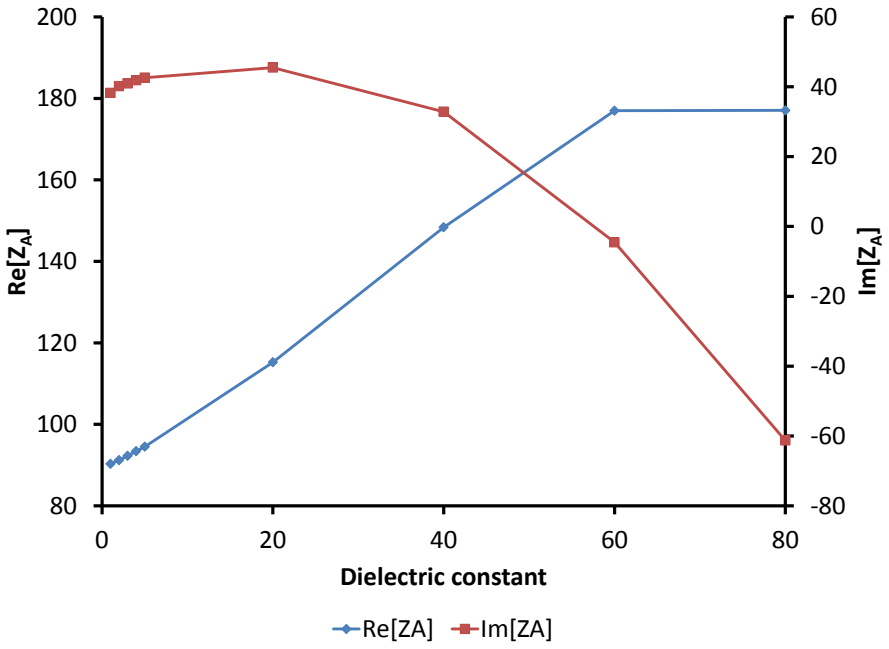
200
180
160
140
120
100
80
60
40
20
0
-20
-40
-60
-80
0
20
40
60
80
Re[Z_A]
Im[Z_A]
Dielectric constant
Re[ZA]
Im[ZA]

(a)

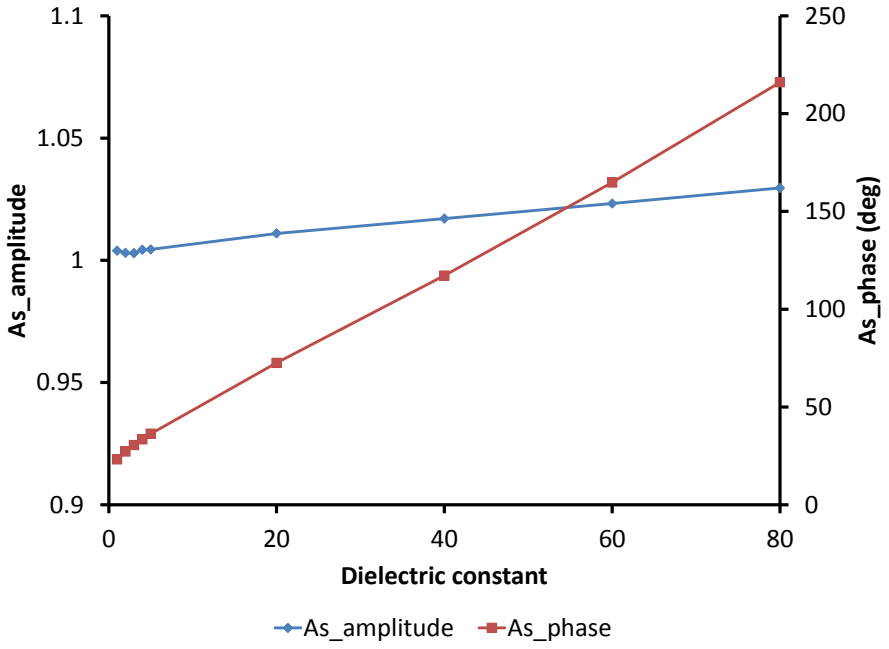
1.1
1.05
1
0.95
0.9
250
200
150
100
50
0
0
20
40
60
80
As_amplitude
As_phase (deg)
Dielectric constant
As_amplitude
As_phase

(b)

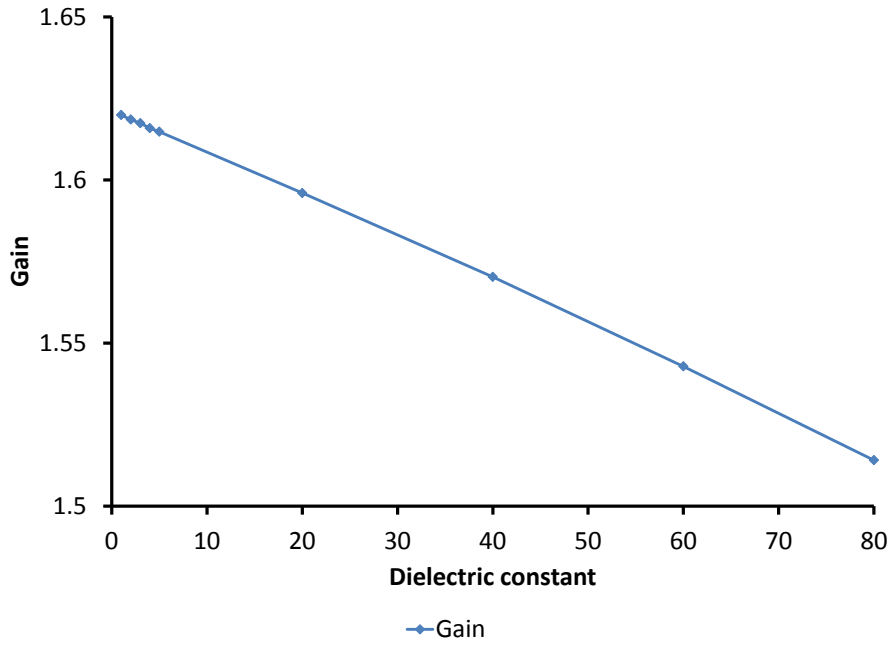

(c)

Figure 3.15. Simulation results for the antenna characterization parameters under the environmental effects; the range of the dielectric constants: [1, 2, 3, 4, 5, 20, 40, 60, 80]. (a) Z_A (b) A_S (c) gain.

In conclusion of the simulations based on the settings in Table 3-13, the antenna characterization parameters (Z_A, A_S, and gain) are changed under the environmental effect caused by an object with different dielectric constants. When dielectric constant linearly rises from 1 to 80,

- the real part of the antenna input impedance increases monotonically while the imaginary part of it becomes more inductive first but becomes more capacitive later;
- the locations of the A_S rotates counterclockwise around the origin in the complex plane, and the amplitude and the phase of A_S increase linearly;
- the gain of the antenna decreases in a linear fashion because more energy is directed toward the other side.

To validate the vector backscattering model under the environmental effect, the numerical results are provided for the error between the results of $|E_{BS}|$ from the model and the simulation; the errors are quantified in $AERR_S$ (amplitude error ratio in simulation defined in (3.10.1) and PER_S (phase error in simulation defined in (3.10.2)). Two cases are considered in the error analysis; in case 1, the antenna characterization parameters corresponding to dielectric constants, ε_r = [1, 2, 3, 4, 5], are used in the model predicting the vector backscattering from the antenna under the presence of an object with the dielectric constant = [1, 2, 3, 4, 5]; in case 2, the antenna characterization parameters of dielectric constant, ε_r = 1, are used in the model predicting the vector backscattering from the antenna under the presence of an object with the dielectric constant = [1, 2, 3, 4, 5].

The averaged $AERR_S$ and PER_S are presented in Table 3-14; the $AERR_S$ and PER_S are averaged through five dielectric constants and five resistive or complex load impedances as listed in Table 3-3 and 3-5. The accuracy of the vector backscattering model is good in case I, while the averaged amplitude and phase errors in case 2 is higher than those in case 1.

Table 3-14. Averaged $AERR_S$ and PER_S under the environmental effect.

	Case 1*		**Case 2****	
Average	**Z_{LR}*****	**Z_{LC}******	**Z_{LR}*****	**Z_{LC}******
$AERR_S$ (%)	0.077655861	0.347835453	3.143406691	3.798522675
PER_S (deg)	0.007225474	0.192558265	5.725390214	5.664619615

*(Case I): the antenna characterization parameters corresponding to dielectric constants, εr = [1, 2, 3, 4, 5], are used in the model predicting the vector backscattering from the antenna under the presence of an object with the dielectric constant = [1, 2, 3, 4, 5]

**(Case II): the antenna characterization parameters of dielectric constant, εr = 1, are used in the model predicting the vector backscattering from the antenna under the presence of an object with the dielectric constant = [1, 2, 3, 4, 5]

***(Z_{LR}): resistive load impedances listed in Table 3-3

***(Z_{LC}): complex load impedances listed in Table 3-5

The vector backscattering model is valid for the prediction of the vector backscattered field and the wireless measurement of the load impedance when the well-characterized antenna parameters are provided. In other words, when these three antenna parameters characterized in the free space are used in the vector backscattering model to predict the vector backscattered fields from an antenna in the free space, the results can be highly accurate, as shown in the previous section. The vector backscattering model is also capable of high accurate prediction of the vector backscattering under the environmental effects when the corresponding antenna characterization parameters are used. However, the vector backscattering model becomes less accurate when the antenna characterization parameters which is characterized in the free space are used to predict the vector backscattered fields of an antenna under the environmental effect, as shown in Case II. This is the same challenge the RFID tag designers are facing when dealing with the environmental effects on RFID tags.

3.6 Experiment Results

A vector network analyzer (VNA) is used for the backscattered voltage signal measurement of the loaded planar dipole antenna. The experiment setup is shown in Figure 3.16, the vector network analyzer is connected to a horn antenna which is used as a transmitting/receiving antenna operating through 800 – 1200 MHz. Both this horn antenna and the load scattering antenna are placed in an anechoic chamber room for reduction of the interference of the external waves and internal reflections. The planar dipole antenna is aligned with the polarization of the incident field and positioned for front-facing incidence.

The received signal is composed of the backscattered signal from the scatterer and two signals: the reflection of antenna mismatching and the reflection of the imperfect anechoic chamber. These two reflected signals are removed by doing the background subtraction which requires high consistency of the whole experimental condition through the process for each measurement.

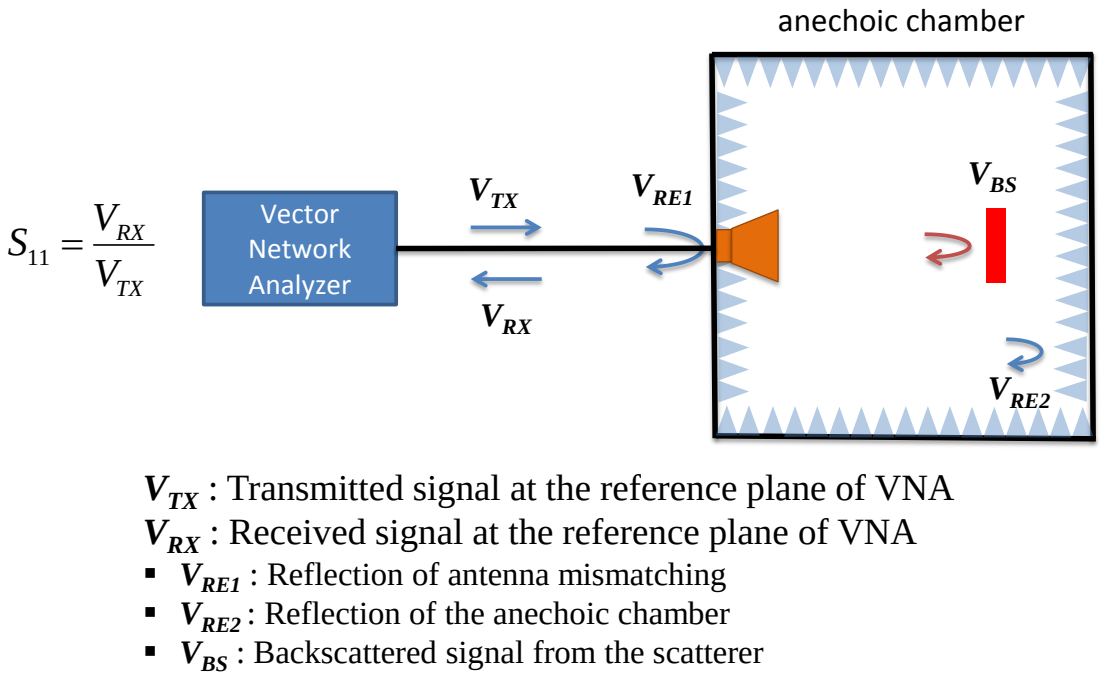

Figure 3.16. Experiment setup for the backscattered voltage signal measurement of the loaded planar dipole antenna in an anechoic chamber.

Ten samples of measurement are conducted for each load and the experimental results of the backscattered voltage signal of the scattering antenna are loaded with the open load, the five Z_{LR}s, and the five Z_{LC}s.

In the actual experiments, the propagation path introduces energy loss (amplitude attenuation) and phase increment. Therefore, the amplitude compensation factor, A_C, and compensation phase, θ_C, are included in equations. A_C is acquired by taking the ratio between the experimental and model amplitude when the scattering antenna is open-loaded; θ_C is acquired by taking the difference between the simulated and model phase when the scattering antenna is open-loaded.

The error between the results of $|V_{BS}|$ from experiment and model is quantified by the experiment amplitude error ratio, $AERR_E$, which is defined as

$$AERR_E = \left| \frac{\left|\overrightarrow{V_{BS}}\right|_E - \left|\overrightarrow{V_{BS}}\right|_M}{\left|\overrightarrow{V_{BS}}\right|_M} \right| \tag{3.12.1}$$

where, $|V_{BS}|_E$ is the experimental $|V_{BS}|$ and $|V_{BS}|_M$ is the model $|V_{BS}|$.

The error between the results of θ_{VBS} from experiment and model is quantified by the experiment phase error, PER_E, which is defined as

$$PER_E = \left|\theta_{VBS,E} - \theta_{VBS,M}\right| \tag{3.12.2}$$

where, $\theta_{VBS,E}$ is the experimental θ_{VBS} and $\theta_{VBS,M}$ is the model θ_{VBS}.

The experiment amplitude error ratio, $AERR_E$ and the experiment phase error, PER_E, for the five Z_{LR}s and the five Z_{LC}s are presented in Figure 3.17 and Figure 3.18.

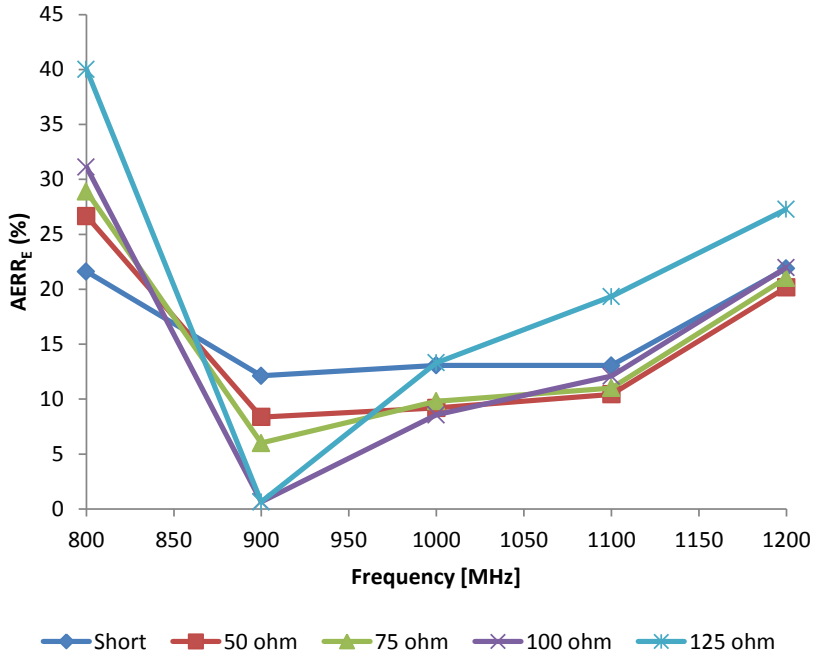

(a)

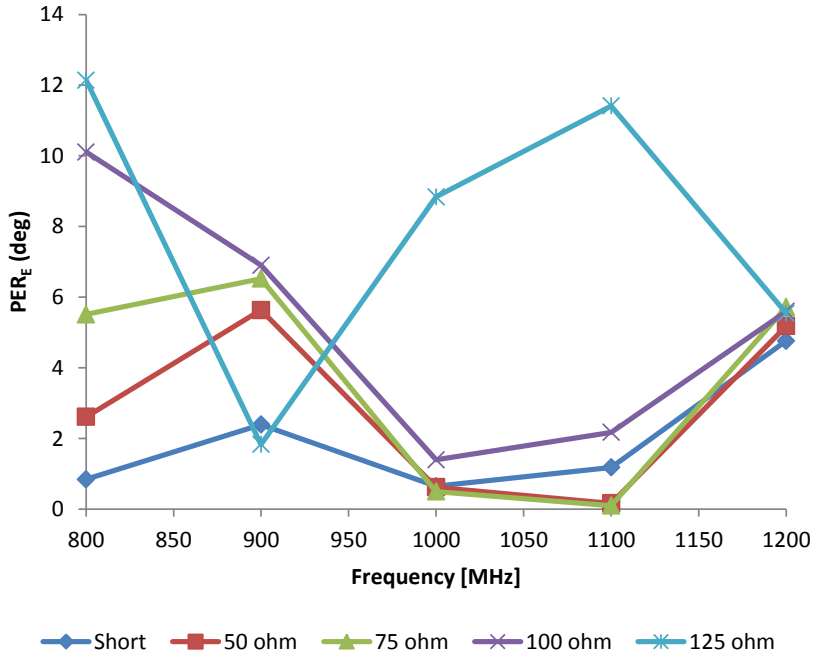

(b)

Figure 3.17. The experiment error of the backscattered electric field of the scattering antenna loaded with Z_{LR}; (a) Amplitude: $AERR_E$ (b) Phase: PER_E.

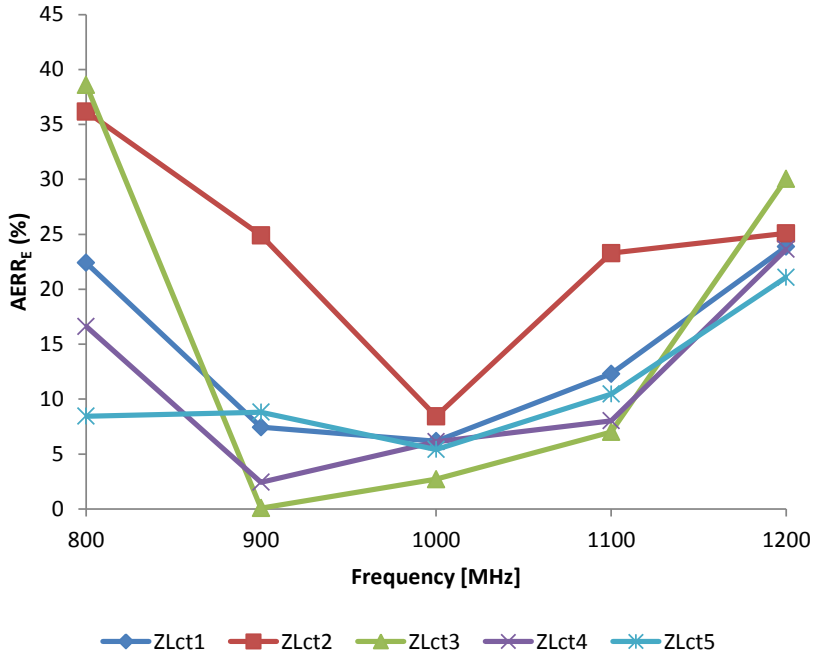

(a)

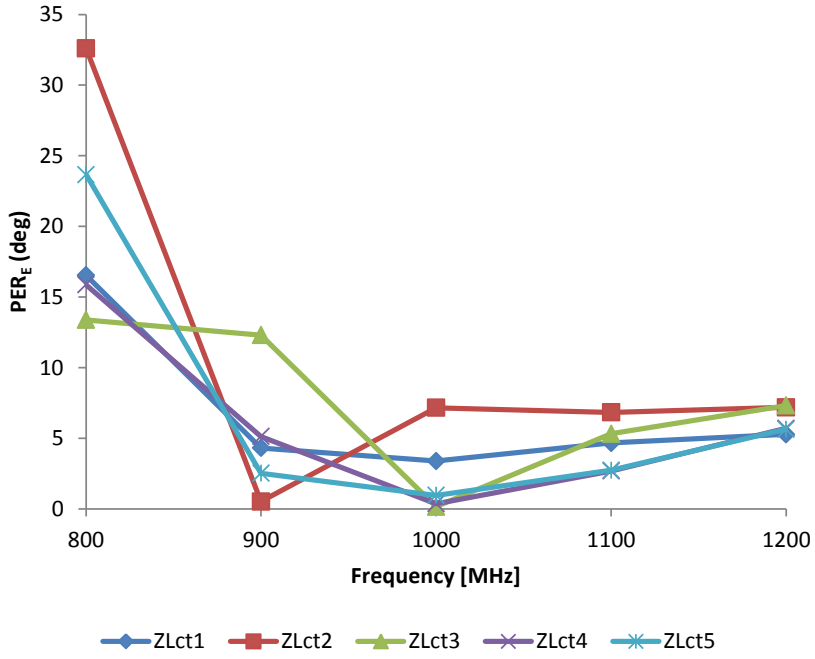

(b)

Figure 3.18. The experiment error of the backscattered electric field of the scattering antenna loaded with Z_{LC}; (a) Amplitude: $AERR_E$ (b) Phase: PER_E.

The proposed model can predict the vector backscattered fields but the accuracy of experimental results is not as good as what is provided by the simulation results. The main reason is that the far field conditions could be satisfied in simulations but experiments are done when the distance is insufficient for fulfilling the far-field conditions. In the experiment setting, the distance between the transmitting/receiving antenna and the scattering antenna is 700 mm which is roughly triple the wavelength for frequency ranged from 800 MHz to 1200 MHz. To more approach the far-field conditions, the distance between the transmitting/receiving antenna and the scattering antenna must be increased. In general, when the distance is larger than ten times the wavelength, the error caused by the non-perfection of the far-field conditions is within an acceptable range. For the operation frequency range between 800 MHz and 1200 MHz, the accuracy of the experimental results can be improved when the transmitting/receiving antenna is placed more than 3750 mm away from the scattering antenna.

However, it is challenging for having an anechoic chamber with sufficient space and detecting signal with a low power level. For a round trip wave propagation (starting from the transmitting/receiving antenna to the scattering antenna, and then scattered back to the transmitting/receiving antenna), the power density of the backscattered field is inversely proportional to the fourth power of the distance. When the backscattered power is decreased, reliable signal detection is difficult and the experimental results are vulnerable to noise.

Even though the far-field conditions are not fulfilled in practice, the experiment results can be fairly estimated by the vector backscattering model. As indicated in Figure 3.17 and Figure 3.18, most of the experiment amplitude error ratio, $AERR_E$, are below 15%, and most of and the experiment phase error, PER_E, are below 10 degree. In fact, this model is practically suitable for applications in which only multiple discrete values are needed with better error tolerance.

Chapter 4 Wireless Impedance Measurement by Vector Backscattering

4.1 Introduction

Impedance measurement is accomplished by detecting the reflection coefficient which is by definition the ratio of the reflected wave and the transmitted wave. The reflection coefficient is also a complex parameter and a function of the characteristic impedance of the measurement system and the impedance of the load under test. In general, a vector network analyzer is used to generate a transmitted wave and receive the reflected wave. With the measured reflection coefficient, the impedance of the load under test is determined [70].

In the past decades, the theory of loaded scattering antenna has been studied and applied in various aspects [29–31], [35], [55]. The scattering of a loaded antenna carries the properties of the connected load and the scattering antenna itself. Therefore, scattering-based antenna characterization techniques have been developed in [71], [72]. On the other hand, radar cross section (RCS) equation is used for linking the scattering power and the load connected to the scattering antenna. This mechanism can be applied to wireless sensing or wireless communication, such as the passive ultra high frequency radio-frequency identification (UHF RFID). In a RFID system, the communication between a reader and a tag is established when the RCS of a passive tag is modulated by switching the load impedance of the tag. Actually, not only the scattering strength is used for modulation, but also the scattering phase is used for modulation. However, the phase of a scattered wave has not been thoroughly researched for an analytical description.

In Chapter 3, the equations of the vector backscattering of a loaded scattering antenna are presented. These equations lead to the equation of the link between the ratio of two backscattered voltage signals and the ratio of the corresponding modified reflection coefficients. And then, the equations are derived for both the scattering antenna parameter and the wirelessly measured impedance.

The structure mode vector A_S is one of the scattering antenna parameters. It is characterized in one equation and can be obtained from the measurement of the backscattered voltage signals and the modified reflection coefficient of two loads. Conventionally, it is necessary to have three loads for the structure mode vector characterization in graphical or analytical methods, as presented in [33], [34]. This proposed method not only simplifies the process of the scattering antenna characterization but also reduces the required number of loads from three to two. Although the gain of the scattering antenna cannot be characterized, it is not necessary for the wireless impedance measurement.

With the completion of the scattering antenna characterization, the modified reflection coefficient of the load under test can be determined by the modified reflection coefficient of the reference load and the backscattered voltage signals of the load under test and reference load. Then, the impedance of the load under test is obtained from the corresponding modified reflection coefficient.

In the next section, the derivation of the equations for scattering antenna characterization and wireless impedance measurement are presented. Then the details of the scattering antenna used in the experiments are addressed. The experimental setups, the measurement results of the scattering antenna parameter, and the results of the wireless impedance measurements for resistive and complex loads are presented.

4.2 Wireless Impedance Measurement Model

Scattering of a loaded antenna carries the characteristics of the antenna and the load. The radar cross section (RCS), σ, is proportional to the scattering energy of a scatterer in the far field. Backscattering is the special case for a system in which the transmitting antenna and the receiving antenna are collocated. For a scattering antenna, the backscattering RCS, σ_{BS}, is a function of the connected load; it is described in chapter 3 and given by

$$\sigma_{BS} = \frac{\lambda^2}{4\pi} G_{SA}^2 \left| \Gamma_m - A_S \right|^2 = \frac{\lambda^2}{4\pi} G_{SA}^2 \left| \frac{Z_L - Z_A^*}{Z_L + Z_A} - A_S \right|^2 \tag{4.1}$$

where the wavelength of the carrier wave is λ, the gain of the scattering antenna is G_{SA}, the input impedance of the scattering antenna is Z_A, the load impedance is Z_L, and the structure mode vector is A_S, and the modified reflection coefficient is Γ_m. A_S is a load-independent complex parameter representing for the structural mode scattering; whereas Γ_m, which represents for the antenna mode scattering, is depends on both Z_A and Z_L.

In chapter 3, the equations of the backscattered voltage signal vector are also presented for a scattering antenna with a complex load. The amplitude and the phase are expressed as

$$\left| \overrightarrow{V_{BS}} \right| = \left(\frac{\lambda}{4\pi R} \right)^2 G_{TR} G_{SA} A_C \cdot \left| \overrightarrow{V_{TX}} \right| \cdot \left| \Gamma_{BS} \right| \tag{4.2}$$

$$\theta_{VBS} = \theta_{\Gamma BS} + \theta_0 + \theta_C \tag{4.3}$$

in which Γ_{BS} is the vector between A_S and Γ_m and it is defined as the backscattering coefficient. V_{TX} and V_{BS} are transmitted and backscattered voltage signals. G_{TR} is the gain of the transmitting/receiving antenna. R is the distance from the observation point to the scatterer. In

(4.2), the amplitude compensation factor, A_C, accounts for the propagation attenuation which is not included in the situation described by the radar range equation. In (4.3), the compensation phase, θ_C, is added for the phase of the propagation path in the actual experiment setup.

Like the conventional reflection coefficient used in Smith Chart, the modified reflection coefficient Γ_m is a conformal mapping function between the input impedance of the scattering antenna Z_A and the load impedance Z_L. In other words, given one Z_A at one frequency, every Z_L corresponds to exactly one Γ_m. In addition, the structure mode vector A_S at one frequency is a constant complex number; therefore, the backscattering coefficient Γ_{BS} and the load impedance Z_L form a one-to-one mapping. Therefore, two impedance loads Z_{L1} and Z_{L2} correspond to two backscattered voltage signals respectively. The amplitude ratio of these two signals is expressed as

$$\frac{\left|\overrightarrow{V_{BS,Z_{L2}}}\right|}{\left|\overrightarrow{V_{BS,Z_{L1}}}\right|} = \frac{\left|\Gamma_{BS,Z_{L2}}\right|}{\left|\Gamma_{BS,Z_{L1}}\right|} \tag{4.4}$$

; the phase difference of these two signals is written as

$$\theta_{V_{BS,Z_{L2}}} - \theta_{V_{BS,Z_{L1}}} = \theta_{\Gamma_{BS,Z_{L2}}} - \theta_{\Gamma_{BS,Z_{L1}}} \tag{4.5}$$

Equation (4.4) and (4.5) are valid when all the other parameters are identical and the load impedance is the only parameter varied in the measurement setting. The combination of (4.4) and (4.5) gives the ratio of these two backscattered voltage signals:

$$\frac{\overrightarrow{V_{BS,Z_{L2}}}}{\overrightarrow{V_{BS,Z_{L1}}}} = \frac{\Gamma_{BS,Z_{L2}}}{\Gamma_{BS,Z_{L1}}} = \frac{A_S - \Gamma_{m,Z_{L2}}}{A_S - \Gamma_{m,Z_{L1}}} \tag{4.6}$$

As shown in (4.6), the ratio of the two backscattered voltage signals is equal to the ratio of the corresponding two modified reflection coefficients, and this equation can be rearranged for the structure mode vector and expressed as

$$A_S = \frac{(\frac{\overrightarrow{V_{BS,Z_{L2}}}}{\overrightarrow{V_{BS,Z_{L1}}}}) * \Gamma_{m,Z_{L1}} - \Gamma_{m,Z_{L2}}}{(\frac{\overrightarrow{V_{BS,Z_{L2}}}}{\overrightarrow{V_{BS,Z_{L1}}}}) - 1} \tag{4.7}$$

Equation (4.7) indicates that the structure mode vector A_S is characterized by the ratio of two backscattered voltage signal and the corresponding modified reflection coefficients. For a given Z_A, the modified reflection coefficients are obtained for Z_{L1} and Z_{L2}, as follows:

$$\Gamma_{m,Z_{L1}} = \frac{Z_{L1} - Z_A^*}{Z_{L1} + Z_A} \tag{4.8.1}$$

$$\Gamma_{m,Z_{L2}} = \frac{Z_{L2} - Z_A^*}{Z_{L2} + Z_A} \tag{4.8.2}$$

In other words, the characterization of A_S requires the vector signal measurement of only two load impedances and it can be done in one equation.

To wirelessly measure the impedance of a load, Z_L, a reference load with a known impedance value is needed and it can be arbitrarily chosen. Equation (4.6) is rephrased for $Z_L = Z_{L2}$, $Z_{L,ref} = Z_{L1}$ as

$$\Gamma_{m,Z_L} = A_S - (\frac{\overrightarrow{V_{BS,Z_L}}}{\overrightarrow{V_{BS,Z_{Lref}}}}) * (A_S - \Gamma_{m,Z_{Lref}}) \tag{4.9}$$

which specifies the modified reflection coefficient of the load under test. With the measured ratio of two backscattered voltage signal and the modified reflection coefficient of the reference load, the modified reflection coefficient of the reference load is determined for a given Z_A. Derived from the definition of Γ_m, the load impedance is rearranged as

$$Z_L = \frac{Z_A^* + \Gamma_{m,Z_L} * Z_A}{1 - \Gamma_{m,Z_L}} \tag{4.10}$$

, and Z_L is determined by the modified reflection coefficient of the load under test which is obtained from (4.9).

In conclusion, the procedure of the wireless impedance measurement of a loaded scattering antenna is described below,

- Characterize Z_A: Run the simulation for the input impedance of the antenna in a 3D EM simulation tool.
- Characterize A_S: Measure vector backscattering of the two loads with two loads with known impedances. In general, open load and short load are chosen because of simplicity and the least device error.

- Determine $\Gamma_{m,ZL}$: Measure vector backscattering of the scattering antenna with the load under test while the open load is taken as the reference impedance.
- Calculate Z_L: Make the calculation for Z_L with the simulated Z_A and the measured $\Gamma_{m,ZL}$.

Given the completion of the scattering antenna characterization, both of the amplitude and the phase of the backscattered electric field are provided for fully describing the vector backscattering of an antenna with a complex load. Therefore, when a vector backscattering field is obtained, the load impedance can be precisely predicted by using this model for both real part and imaginary part regardless the values of the impedances. Based on the far-field simulation results of the vector backscattering fields presented in preceding chapter, the wireless impedance measurement for five resistive load impedances is conducted with the maximum error for the real part and imaginary part are less than 0.3 and 0.4 ohms respectively; the wireless impedance measurement for five complex load impedances is conducted with the maximum error for the real part and imaginary part are less than 0.6 and 1.0 ohms respectively through the whole frequency range. These simulation results show high accuracy of the method of the wireless impedance measurements in the far field.

In the following sections, the proposed wireless impedance measurement method will be performed experimentally for a UHF planar dipole antenna loaded with static resistive and complex impedances. This wireless impedance measurement procedure will also be applied to a UHF RFID tag antenna loaded with a tag chip switching between two different complex impedances.

4.3 Loaded Planar Dipole Antenna

In this section, a loaded planar dipole antenna is measured for the verification of the proposed wireless impedance measurement method. The planar dipole antenna used in the wireless impedance measurement is the same one used in Chapter 3. This antenna fabricated on an FR4 substrate is designed as a scattering antenna and the resonant frequency is within the ultra-high-frequency (UHF) band from 800MHz to 1200MHz. The input impedance of this planar dipole antenna is simulated in the CST Microwave Studio and the results are indicated in Figure 4.1.

4.3.1 Experiment Setup

Vector network analyzer (VNA) is used for the backscattered voltage signal measurement of the loaded planar dipole antenna. The experiment setup is shown in Figure 4.1, the vector network analyzer is connected to a horn antenna which is used as a transmitting/receiving antenna operating through the frequencies of interest (800, 900, 1000, 1100, and 1200 MHz). Both this horn antenna and the load scattering antenna are placed in an anechoic chamber room for reduction of the interference of the external waves and internal reflections.

The received signal is composed of the backscattered signal from the scatterer and two signals: the reflection of antenna mismatching and the reflection of the imperfect anechoic chamber. These two reflected signals are removed by doing the background subtraction which requires high consistency of the whole experimental condition through the process for each measurement.

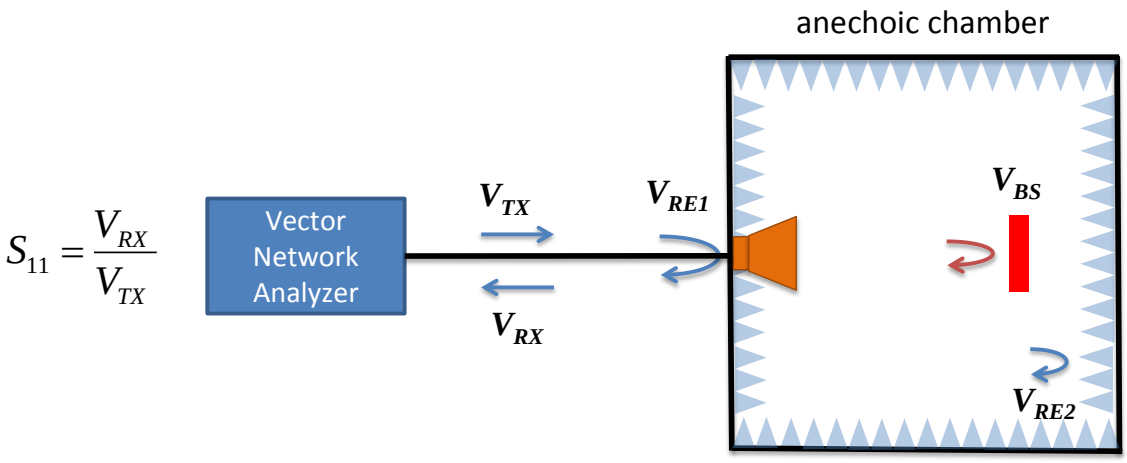

V_{TX} : Transmitted signal at the reference plane of VNA
V_{RX} : Received signal at the reference plane of VNA
- V_{RE1} : Reflection of antenna mismatching
- V_{RE2} : Reflection of the anechoic chamber
- V_{BS} : Backscattered signal from the scatterer

Figure 4.1. Experiment setup for the backscattered voltage signal measurement of the loaded planar dipole antenna in an anechoic chamber.

4.3.2 Characterization of Structure Mode Vector

The equation of the structure mode vector A_S is described by (4.7), and Z_{L1} and Z_{L2} are chosen to be infinite (open) and zero (short) for the least error of load impedance. Ten samples of measurement are performed for the backscattered voltage signals corresponding to Z_{L1} (open) and Z_{L2} (short). A_S can also be solved analytically with three simulated σ_{BS} which corresponds to three different loads. The characterization of A_S of the planar dipole antenna is completed and the simulated result is presented in Table 3.2 and Figure 3.4. Ten samples of backscattered voltage signal measurement are performed for open and short loaded planar dipole antennas. The measurement and simulation results show a good agreement through different frequencies in Figure 4.2.

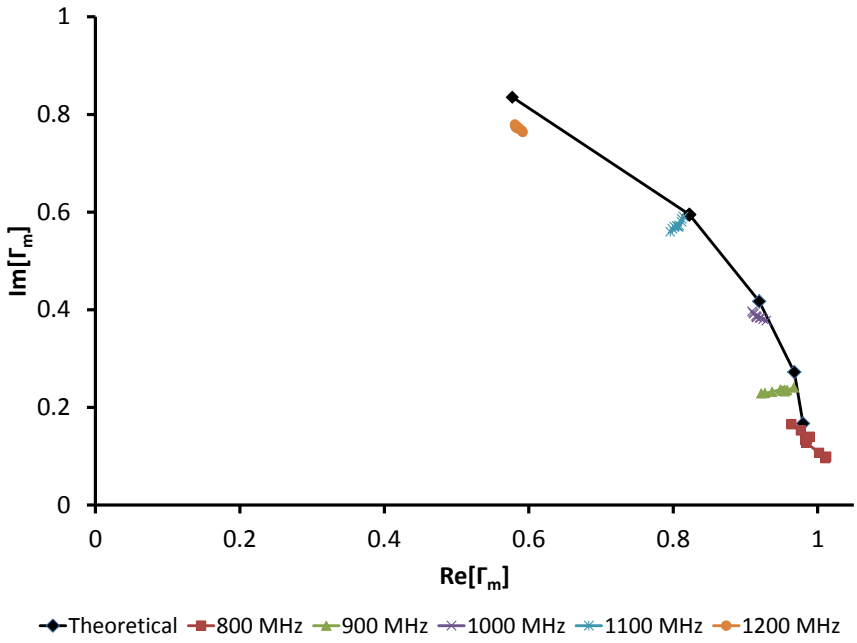

Figure 4.2. The structure mode vector A_S for frequency = 800, 900, 1000, 1100, and 1200 MHz. (Black: simulation; color: measurement).

4.3.3 Experiment Results

The loads under test are categorized into two groups: resistive loads (Z_{LR}) and complex loads (Z_{LC}). Z_{LR} is the set of five resistive loads: [0Ω, 50Ω, 75Ω, 100Ω, 125Ω]; Z_{LC} is the set of five complex loads with corresponding Γ_m approximate to 0, +0.5, +0.5j, -0.5, -0.5j at 1000MHz: [100Ω + 4.5pF, 280Ω + 4.5pF, 53.6Ω + 6.3nH, 30.1Ω + 4.5pF, 53.6Ω + 1.5 pF]. The impedances and the modified reflection coefficients of five Z_{LR}s at frequencies of interest are listed in Table 3.3 and Table 3.4; the impedances and the modified reflection coefficients of five Z_{LC}s at frequencies of interest are listed in Table 3.6 and Table 3.7

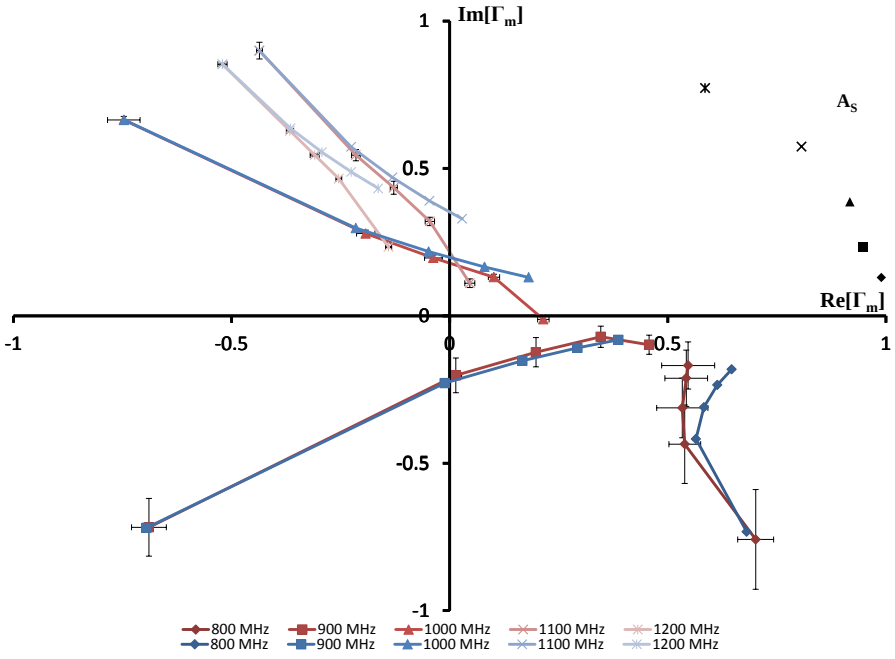

(a)

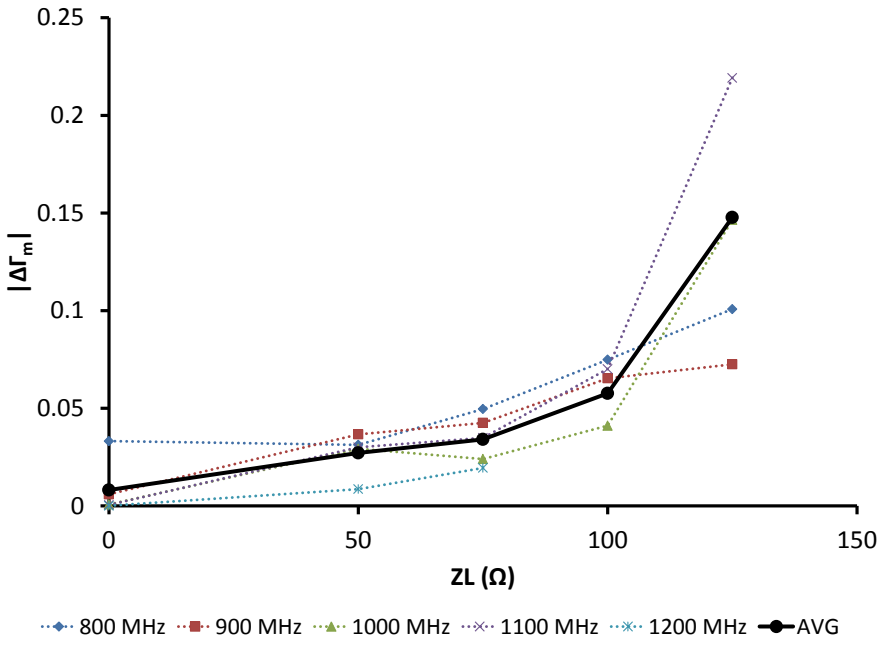

(b)

Figure 4.3. (a) The modified reflection coefficient Γ_m for five Z_{LR} for 800 MHz – 1200 MHz. (b) The absolute value of the modified reflection coefficient error $|\Delta\Gamma_m|$ for 800 MHz – 1200 MHz.

Ten samples of measurement are conducted for each resistive load and the averaged experimental results of the corresponding modified reflection coefficients are shown on the Γ_m–plane as five red curves for five frequencies in Figure 4.3. The horizontal and vertical error bars are included to indicate the plus and minus standard deviation of the ten samples of measurement for the real and imaginary part of the modified reflection coefficients individually. The measurement of 800 MHz shows the most error compared with all the other frequencies and it may result from the obvious deflection effect at low frequency.

The modified reflection coefficients of five Z_{LR}s are calculated and presented as five blue curves for five frequencies in Figure 4.3. As noticed, each measured Γ_m shows great consistency with the calculated one at low impedance but it start deviating from the calculated for higher impedance. The absolute values of the difference between the measured and calculated Γ_m for Z_{LR} are also shown in Figure 4.3.

With the measured Γ_m, each of the Z_{LR} is determined by (4.10); the average and standard deviation error bar of the ten sample measurement are displayed in Figure 4.4. The notable error bar at 800 MHz indicated in the results of Z_L reflects the larger error bar of Γ_m at the same frequency. Since the resistive loads are not frequency-dependent, straight lines are expected for impedance = 0Ω, 50Ω, 75Ω, 100Ω, 125Ω at different frequencies. The results of low impedances (0Ω, 50Ω, and 75Ω) match the correct impedance value in straight lines through frequencies while the results of high impedances (100Ω and 125Ω) have greater errors. The averaged errors and error bars for five Z_{LR} are also shown in Figure 4.4.

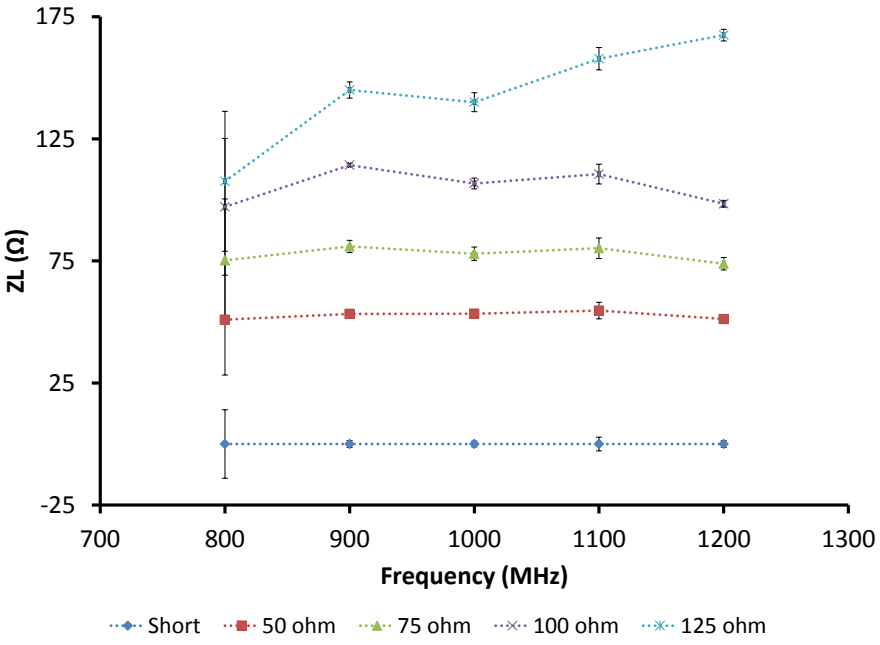

(a)

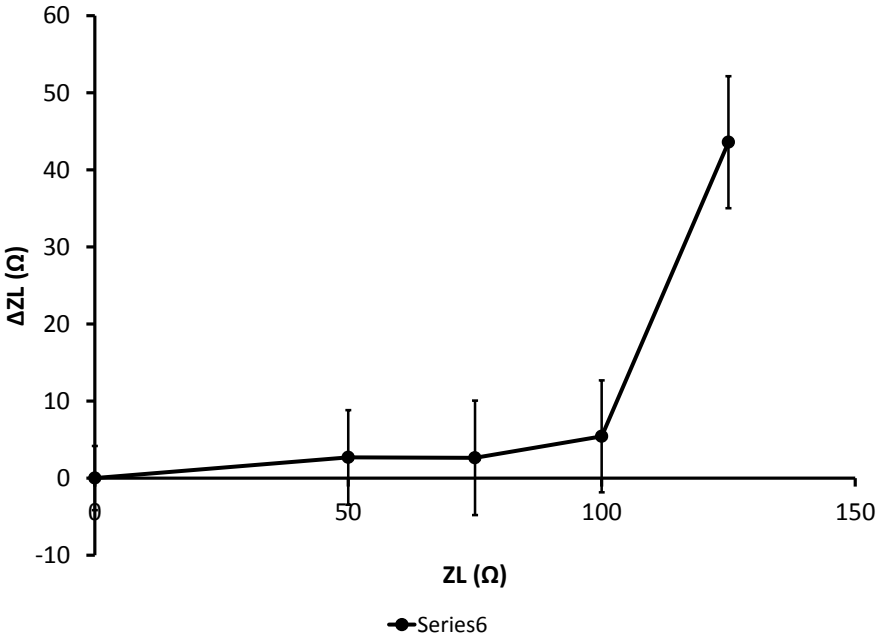

(b)

Figure 4.4. (a) The measured impedances of five Z_{LR} for 800 MHz – 1200 MHz. (b) The average error of measured impedances of five Z_{LR} through five frequencies.

There are two main reasons for the lower accuracy of the measured loads in higher impedances: higher Γ_m error and higher gradient of Γ_m. As displayed in Figure 4.3, the measured Γ_m deviates more from the calculated one for load with higher impedance because the accuracy of the constant phase model drops when Γ_m gets closer to A_S. In other words, a more sophisticated phase model is needed to improve the accuracy of Γ_m.

The other primary factor of the inferior performance of the measured loads in higher impedances results from the higher gradient of Γ_m. As shown in the Smith Chart, the gradient of the reflection coefficient depends on the impedances. That means the rates of impedance change of two loads are different if the same reflection coefficient deviation is applied. For the example of a standard 50Ω-system, the impedance errors for the short load (0Ω; Γ = -1) and the matched load (50Ω; Γ = 0) are 2.63 and 11.11 Ω respectively. Given a fixed amount of reflection coefficient deviation, more impedance error is caused by the load with higher impedance value. This principle applies to the modified reflection coefficient since the Γ_m and Γ share the same conformal mapping mechanism for impedances. Having these two factors taken into consideration, it is expected that the errors of the measured impedance increases as the impedance rises, as shown in Figure 4.4.

The same process of ten sample measurement is performed for complex loads. The average experimental results of the corresponding modified reflection coefficients are shown on the Γ_m–plane as the red curves for 1000 MHz in Figure 4.5. These five Z_{LC} are intentionally chosen to correspond five Γ_m approximate to 0, +0.5, +0.5j, -0.5, -0.5j at 1000MHz as shown in the blue line in Figure 4.5. The horizontal and vertical error bars are also included to for showing the plus and minus standard deviation of the ten samples of measurement for the real and imaginary part of the modified reflection coefficients individually. The measurement errors are not significant in this case. In general, the results of the measurement and calculation are fairly matched. The absolute values of the modified reflection coefficient error $|\Delta\Gamma_m|$ are from 0.02 to 0.1. The worst case happens to the load with $\Gamma_m \approx +0.5$; that is the one closest to A_S among all the Z_{LC}.

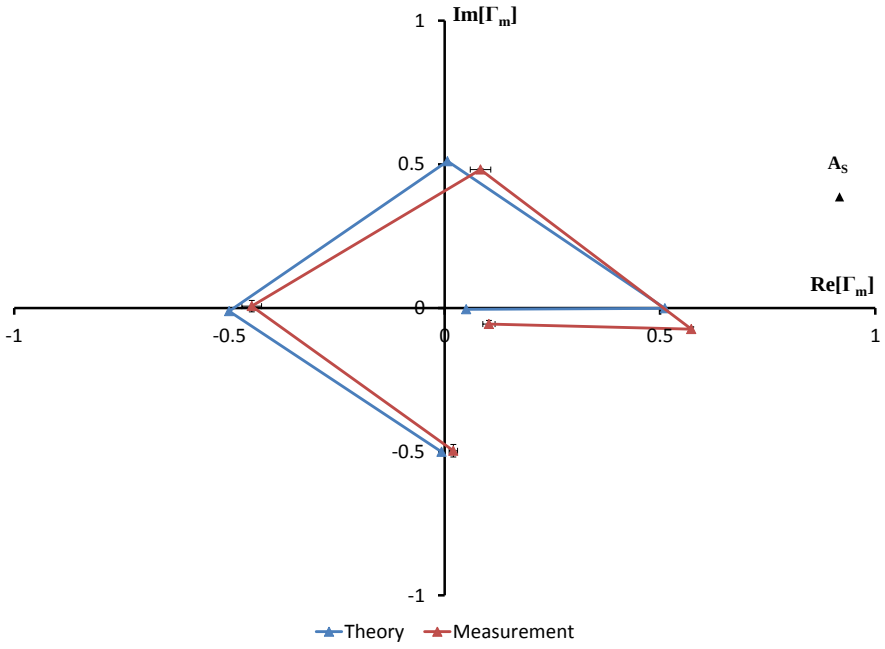

(a)

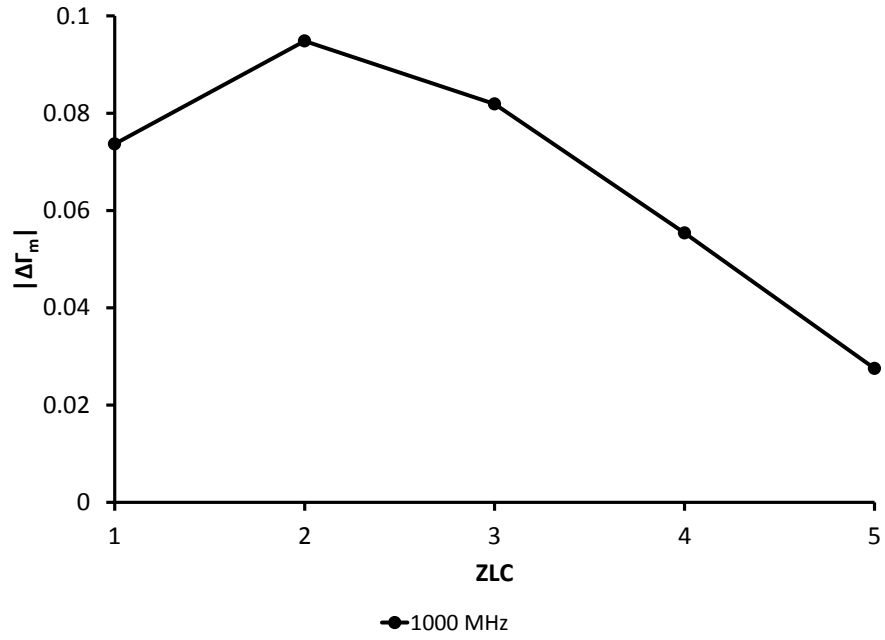

(b)

Figure 4.5. (a) The modified reflection coefficient Γ_m for five Z_{LC} at 1000 MHz. (b) The absolute value of the modified reflection coefficient error $|\Delta\Gamma_m|$ for five Z_{LC} at 1000 MHz.

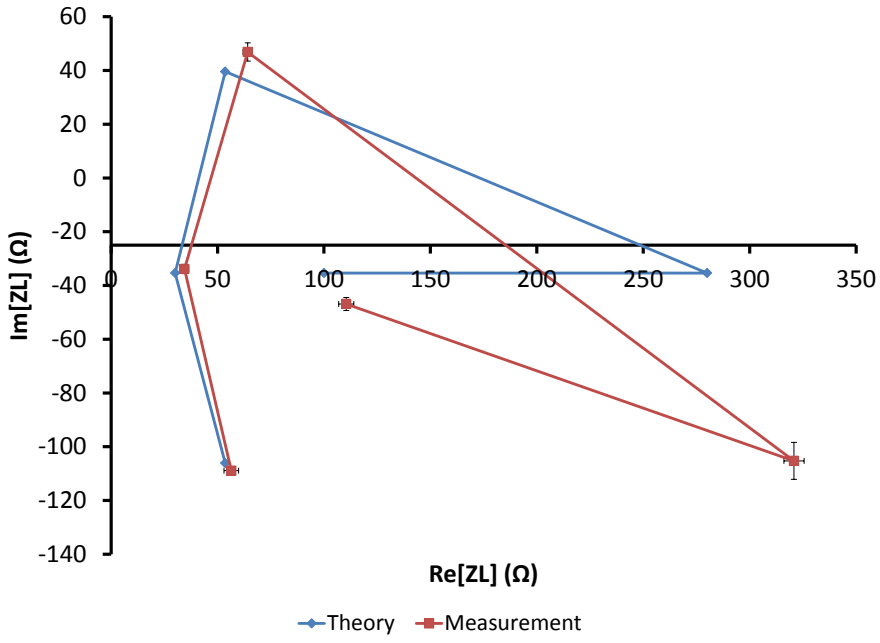

(a)

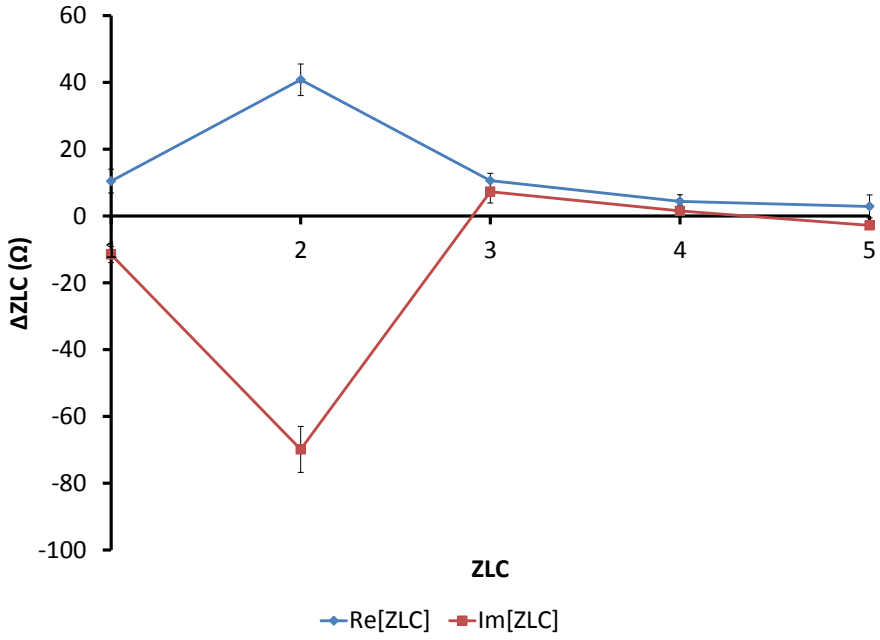

(b)

Figure 4.6. (a) The measured impedances of five Z_{LC} at 1000 MHz. (b) The error of measured impedances of five Z_{LC}.

With the measured Γ_m, each of the Z_{LC} is determined by (4.10); the average and standard deviation error bar of the ten sample measurement are shown in Figure 4.6. The error bars of most of the Z_{LC}s are within an acceptable range when the error bar of the second one is not trivial. In addition, the Γ_m of the second Z_{LC} is located at the highest gradient compared with all the other loads. Consequently, the second Z_{LC} is the worst case and the errors in real part and imaginary part are around 40 and 70 Ω individually while the errors of the rest of Z_{LC}s are less than 10 Ω, as shown in Figure 4.6.

We presented a method of wireless impedance measurement by vector backscattering and verified it experimentally. Derived from the equations of the vector backscattering of a loaded scattering antenna, both the scattering antenna parameter and the wirelessly measured impedance are formulized. A UHF planar dipole antenna is designed as a scattering antenna and used in the experiment. The characterization of the structure mode vector A_S is achieved by the measurement of two backscattered voltage signals of the open-loaded and short-loaded scattering antenna. This new method of the characterization of the structure mode vector not only simplifies the process but also reduces the required number of measured loads. The measurement results of the modified reflection coefficients and impedances of the load under test are presented for resistive and complex loads. For most of the loads, the measurement results are fairly accurate while the errors of the loads with higher impedances are not insignificant.

4.4 Passive UHF RFID Tag

Radio-frequency identification (RFID) technology has been developed and widely applied in diverse aspects in the past decades [19]. It provides simple and economical solutions for wireless identification and data access. In a RFID system, the communication between a reader and a tag is established when the backscatter of a passive tag is modulated by switching the impedance of the tag chip (or so-called ASIC: application-specific integrated circuit). The chip impedance is critical for the design of the tag antenna and the performance of the passive tag.

Conventionally, vector network analyzer (VNA) is used for the wired impedance measurement by connecting the device under test to a 50-Ω-system connector and detecting the reflection coefficient [70]. Typically, a test fixture and a matching network are needed for the technique of the wired tag chip impedance measurement. A test fixture is used for connecting the tag chip and the 50-Ω-system connector. For most of the passive tag chips, the input impedances are highly reactive. Therefore, a matching network is used to improve the measurement accuracy.

On the other hand, the tag chip switches between the absorbing state and the reflecting state only when it receives the query signal in which the command sequence is modulated. The modulation feature is not provided by VNAs, and only the impedance of the absorbing state can be measured [73]. To measure the impedance of the reflecting state, the query signal is required to wake the tag up and it can be generated by a vector signal generator. An experiment setup, which has a vector signal generator cooperating with a VNA, an oscilloscope, and a test fixture, is presented [74].

In chapter 3, we present the method of wireless impedance measurement by vector backscattering, which is derived from the theory of the vector backscattering of loaded scattering antenna. This technique enables the measurement of a complex impedance load which is connected to a scattering antenna by the detection of the vector backscattering wirelessly. Base on the same principle, the experiment setup is modified to apply for the wireless impedance measurement for a tag chip in two states. A time-domain vector reflectometer system is set and provides the capacities of generating modulated signals and receiving reflected (backscattered) signals in time domain. In this method, there is no need to remove the chip from the tag and the

chip is measured in the balanced mode while it is connected to the tag antenna as it operates. Therefore, no test fixture and matching network is needed. In the next section, the equations for scattering antenna characterization and wireless impedance measurement are presented.

The wireless impedance measurement of the tag chips includes the scattering antenna characterization and the detection of the vector backscattering signals. The procedure is described below,

- Characterize Z_A: Run the simulation in a 3D EM simulation tool.
- Characterize A_S: Measure vector backscattering of the two loads with known impedances. In general, open load and short load are chosen because of simplicity and the least device error.
- Determine $\Gamma_{m,ZASIC1}$ and $\Gamma_{m,ZASICC2}$: Measure vector backscattering of the chip-loaded AD-222 in the time-domain vector reflectometer system. The open load is taken as the reference impedance.
- Calculate Z_{ASIC1} and Z_{ASIC2} for the absorbing state and the reflecting state respectively.

4.4.1 Experiment Setup

The measurement setup and the experimental results for the wireless impedance measurement are presented in this section. The tag used in this experiment is AD-222 loaded with Impinj Monza2 chip, as shown in Figure 4.7. AD-222 is simulated in CST Microwave Studio and the input impedance of this tag antenna at 915 MHz is 6.8 + 208.4j.

The experimental setup is displayed in Figure 4.8. Backscattered voltage signals from the tag in two states are measured by the time-domain vector reflectometer system, which is composed of a vector signal generator (VSG), a vector signal analyzer (VSA), a circulator, a transmitting/receiving antenna, and an anechoic chamber. The EPCglobal Gen2 standard query signal is emulated by VSG and transmitted out through the transmitting/receiving antenna to wake up the tag for the responses in both the absorbing state and the reflecting state.

Figure 4.7. UHF RFID passive tag under test: AD-222 (loaded with Monza2 chip).

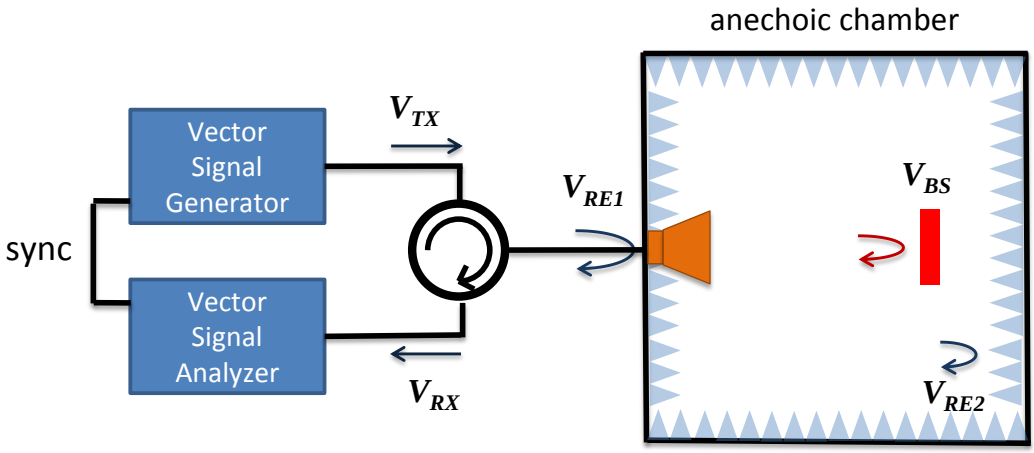

V_{TX} : Transmitted signal from VSG
V_{RX} : Received signal to VSA

- V_{RE1} : Reflection of antenna mismatching
- V_{RE2} : Reflection of the anechoic chamber
- V_{BS} : Backscattered signal from the tag

Figure 4.8. Experiment setup for the backscattering measurement of AD-222.

4.4.2 Experiment Results

The received signal consists of the backscattered signal from the scatterer and two signals: the reflection of antenna mismatching and the reflection of the imperfect anechoic chamber. These two signals is removed by the background subtraction. The backscattering measurement is achieved by using one single antenna for transmission and reception. VSG and VSA are synchronized with rms phase error less than 1 degree for accurate phase measurement. The carrier frequency is controllable and fixed to 915 MHz (the center frequency of the UHF RFID band in North America). The output power of VSG is ranged from 12 to 18 dBm; 12 dBm is the minimum power to turn on the chip, and 18 dBm is the maximum power VSG can provide.

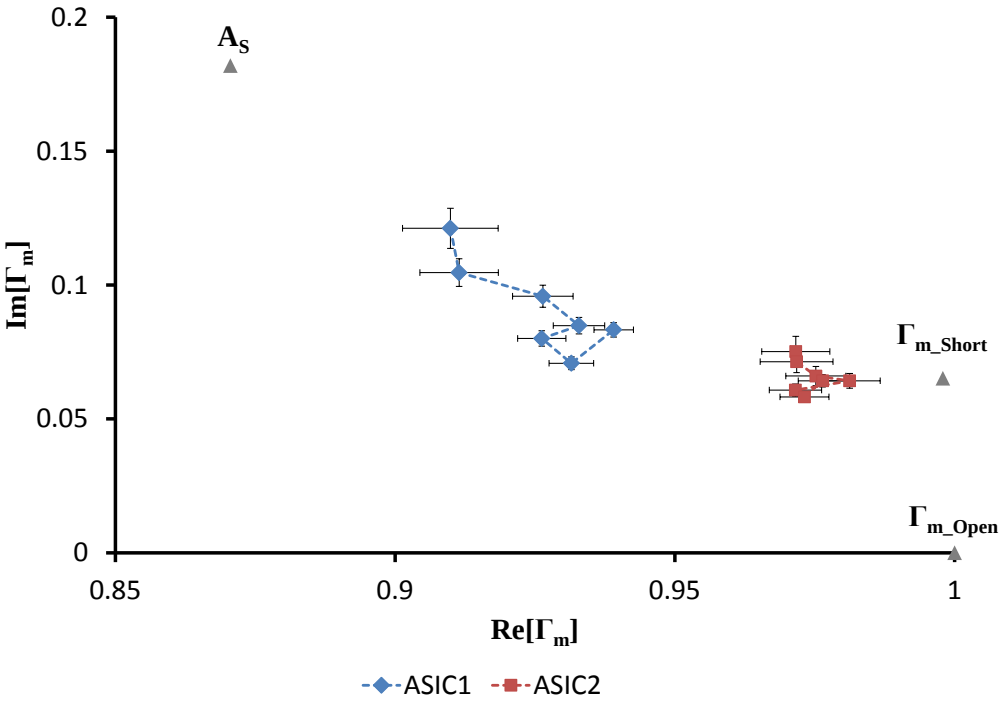

Figure 4.9. The structure mode vector A_S and the modified reflection coefficients of open load, short load, and the tag chip in two states (ASIC1 and ASIC2) on the Γ_m–plane.

The equation of the structure mode vector A_S is determined two known impedances: Z_{L1} and Z_{L2}; they are chosen to be infinite (open) and zero (short) for the simplicity and the least

error of load impedance. Two hundred sample measurements are performed for the backscattered voltage signals corresponding to Z_{L1} (open) and Z_{L2} (short). The averaged result is shown in Figure 4.9. The backscattered voltage signals from AD-222 in two states, ASIC1 and ASIC2, are conducted for two hundred samples in each power level (12–18 dBm). The averaged experimental results of the corresponding modified reflection coefficients are shown on the Γ_m–plane in Figure 4.9. The horizontal and vertical error bars are included to indicate the plus and minus standard deviation of the measurements for the real and imaginary part of Γ_m respectively.

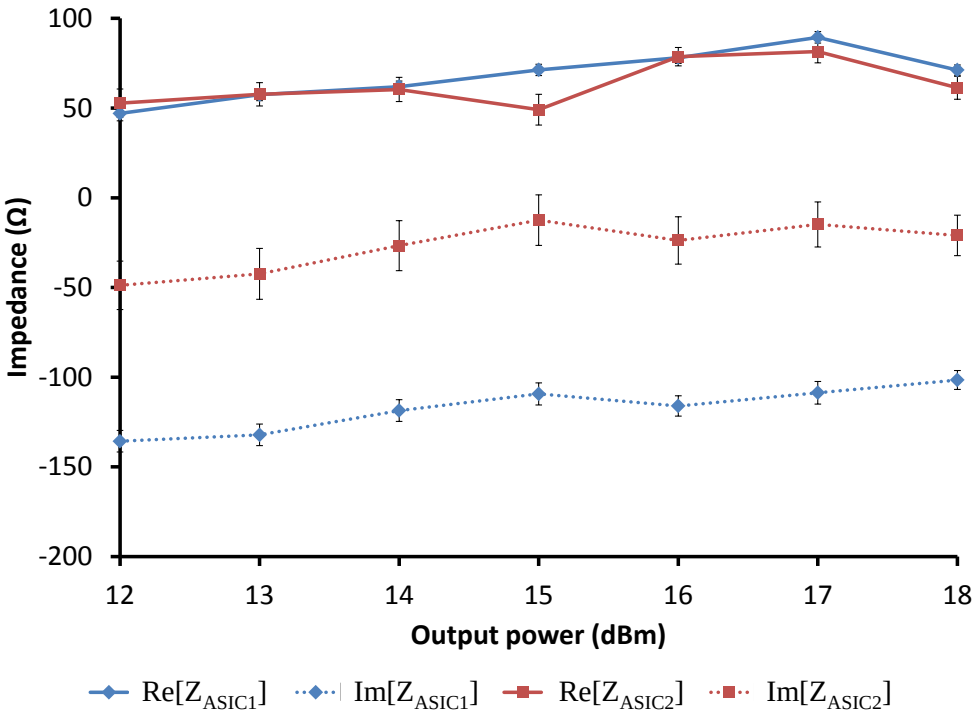

Figure 4.10. The measurement of the tag chip in absorbing state (Z_{ASIC1}) and the reflecting state (Z_{ASIC2}) at 915 MHz.

With the measured Γ_m, the chip impedances of the absorbing state (Z_{ASIC1}) and the reflecting state (Z_{ASIC2}) are calculated by (4.10); the results of the average and the standard deviation error bar are shown in Figure 4.10. The real part of Z_{ASIC1} and Z_{ASIC2} are quite consistent while the imaginary part of Z_{ASIC1} and Z_{ASIC2} differ in 100 Ω approximately. On the other hand, the trend shows slight increase for all as power goes up.

In this chapter, the method of wireless impedance measurement by vector backscattering is presented. Derived from the equation of the vector backscattering of a loaded scattering antenna, the equation is presented for the link between the ratio of two backscattered voltage signals and the ratio of the corresponding modified reflection coefficients. This equation not only leads to a new and improved process for the characterization of the scattering antenna but also provide an approach of wireless impedance measurement. This method is validated by experimental results of a UHF planar dipole antenna loaded with a number of resistive and complex loads.

This method also applies to the passive ultra high frequency (UHF) radio-frequency identification (RFID) tag chips in both the absorbing state (Z_{ASIC1}) and the reflecting state (Z_{ASIC2}). The measurements are performed for the tag chip connected to the tag antenna in the balanced mode as it operates. No test fixture and matching network is needed. The chip impedance measurement in both the absorbing state and the reflecting state is achieved by using the time-domain vector reflectometer system, which is composed of a vector signal generator and a vector signal analyzer. The experimental results are presented for a UHF RFID Gen2 chip (Impinj Monza2).

Chapter 5 Conclusion and Future Directions

This thesis presents the method of the piggyback modulation which integrates sensor data into existing commercial passive UHF RFID tags. This technique is applicable to both active sensor signals and passive sensor loads. We perform the demodulation analysis, and numerical simulation for the conventional amplitude-shift keying (ASK) and quasi-4-quadrature amplitude modulation (quasi-4-QAM). The measurement of the vector backscattering make it possible for the Quasi-4-QAM demodulation which reduces the interference between two independent data streams and improves the bit error rate for the same RF power. In this thesis, the model of the backscattering phase is proposed to complete the analytical description of the vector backscattering. A planar dipole antenna operating in the ultra-high-frequency (UHF) band is used as a scattering antenna to validate the proposed vector backscattering models in both simulations and experiments. Last but not the least, the method of wireless impedance measurement by vector backscattering is presented. Derived from the equations of the vector backscattering of a loaded scattering antenna, the equation is presented for the link between the ratio of two backscattered voltage signals and the ratio of the corresponding modified reflection coefficients. This method is applied for the static impedance measurement of a loaded UHF planar dipole antenna and the dynamic impedance measurement of a passive UHF RFID tag.

In summary, we developed and reported on the first piggyback modulation for generic wireless sensors, opening the door to a wide range of wireless sensing networks enabled by the existing and pervasive UHF RFID infrastructure. To gain a deeper understanding of the limits and possibilities of wireless sensing with our new scheme, we proposed a closed-form vector backscattering model that reports the complex load at a tag antenna. Building on this, we are the first to accomplish the wireless complex impedance measurement for a UHF RFID ASIC for all operating states. This opens the field to development of many passive sensing modalities as well as the potential for more accurate yet contactless vector measurements of (active) microwave circuits. We close with a discussion of the future research directions that arise naturally from this work.

- A passive RFID sensor design

  The piggyback modulation can be implemented for active sensor signal and passive sensor load. The former needs power to drive the modulator and the later still requires an active switching between reference loads and sensor load. To achieve the goal of a passive RFID sensor design, the duel RFID passive sensor is modified from the principle of the RFID sensing by passive sensor load and the proposed as a candidate. In the design of the duel RFID passive sensor, two RFID tags and two passive sensor coupling modules are used. One of them is connected to the reference impedance load while the other one is connected to the passive sensor load. Since the sensing information of each load can be convey to a RFID reader in different frequencies, the active switching between the reference impedance load and the passive sensor load is implemented by a reader.

- Improvement for the vector backscattering model in the non-far-field region

  As indicated in Chapter 3, the far-field simulation results of the vector backscattered fields are precisely predicted by the proposed vector backscattering model, whereas the experiment results are fairly estimated with reduced accuracy due to the limitations of space and RF power. Therefore, to improve the accuracy of the vector backscattering model and the wireless impedance measurement for real-world situations, the next research focus would be the modification of the far-field vector backscattering model for being further practically realized.

- Wireless impedance measurement for scattering antenna by vector backscattering

  The vector backscattering is used for the wireless impedance measurement for the load of a scattering antenna while it has the potential for the measurement of the input impedance of the scattering antenna itself. The impedance measurement of an antenna by backscattering was presented previously, but it can be done by vector backscattering in a simpler fashion since additional quantity: backscattering phase is taken into consideration.

REFERENCES

[1] Dong-Liang Wu, W. W. Y. Ng, D. S. Yeung, and Hai-Lan Ding, "A brief survey on current RFID applications," in *Machine Learning and Cybernetics, 2009 International Conference on*, 2009, vol. 4, pp. 2330–2335.

[2] L. Catarinucci, R. Colella, A. Esposito, L. Tarricone, and M. Zappatore, "A context-aware smart infrastructure based on RFID sensor-tags and its application to the health-care domain," in *Emerging Technologies & Factory Automation, 2009. ETFA 2009. IEEE Conference on*, 2009, pp. 1–8.

[3] "Design and development of radio frequency identification (RFID) and RFID-enabled sensors on flexible low cost substrates.pdf." .

[4] L. Yang, A. Rida, and M. Tentzeris, *Design and Development of Rfid and Rfid-Enabled Sensors on Flexible Low Cost Substrates*. Morgan & Claypool Publishers, 2009.

[5] D. Brenk, J. Essel, J. Heidrich, and R. Weigel, "Ultra low-power techniques for sensor-enhanced RFID tags," in *Wireless Sensing, Local Positioning, and RFID, 2009. IMWS 2009. IEEE MTT-S International Microwave Workshop on*, 2009, pp. 1–4.

[6] A. Aljaafreh and Liang Dong, "Cooperative detection of moving targets in wireless sensor network based on fuzzy dynamic weighted majority voting decision fusion," in *Networking, Sensing and Control (ICNSC), 2010 International Conference on*, 2010, pp. 544–548.

[7] Qi Zhang, Peng Feng, Shenghua Zhou, Zhiqing Geng, and Nanjian Wu, "A novel RFID tag chip with temperature sensor in standard CMOS process," in *Circuits and Systems (ISCAS), Proceedings of 2010 IEEE International Symposium on*, 2010, pp. 1109–1112.

[8] Zhou Shenghua and Wu Nanjian, "A novel ultra low power temperature sensor for UHF RFID tag chip," in *Solid-State Circuits Conference, 2007. ASSCC '07. IEEE Asian*, 2007, pp. 464–467.

[9] R. J. Barton, T. F. Kennedy, R. M. Williams, P. W. Fink, P. H. Ngo, and R. R. Ingle, "Detection, identification, location, and remote sensing using SAW RFID sensor tags," in *Aerospace Conference, 2010 IEEE*, 2010, pp. 1–19.

[10] J. Marjonen, R. Alaoja, H. Ronkainen, and M. Aberg, "Low power successive approximation A/D converter for passive RFID tag sensors," in *Baltic Electronics Conference, 2006 International*, 2006, pp. 1–4.

[11] Huan-Yang Chen, A. Bhadkamkar, and D. W. van der Weide, "Coupling sensors to UHF RFID tags," in *Wireless Sensing, Local Positioning, and RFID, 2009. IMWS 2009. IEEE MTT-S International Microwave Workshop on*, 2009, pp. 1–4.

[12] H.-Y. Chen, A. Bhadkamkar, and D. W. van der Weide, "Piggyback modulation for UHF RFID sensors," in *Microwave Symposium Digest (MTT), 2010 IEEE MTT-S International*, 2010, pp. 1776–1779.

[13] T. Someya, T. Sekitani, S. Iba, Y. Kato, H. Kawaguchi, and T. Sakurai, "A large-area, flexible pressure sensor matrix with organic field-effect transistors for artificial skin applications," *Proceedings of the National Academy of Sciences of the United States of America*, vol. 101, no. 27, pp. 9966 –9970, Jul. 2004.

[14] C. Jiang, S. Markutsya, Y. Pikus, and V. V. Tsukruk, "Freely suspended nanocomposite membranes as highly sensitive sensors," *Nat Mater*, vol. 3, no. 10, pp. 721–728, Oct. 2004.

[15] E. T. Carlen, M. S. Weinberg, C. E. Dubé, A. M. Zapata, and J. T. Borenstein, "Micromachined silicon plates for sensing molecular interactions," *Appl. Phys. Lett.*, vol. 89, no. 17, p. 173123, 2006.
[16] S. Satyanarayana, D. T. McCormick, and A. Majumdar, "Parylene micro membrane capacitive sensor array for chemical and biological sensing," *Sensors and Actuators B: Chemical*, vol. 115, no. 1, pp. 494–502, May 2006.
[17] T. J. Kang, M. Cha, E. Y. Jang, J. Shin, H. U. Im, Y. Kim, J. Lee, and Y. H. Kim, "Ultra-thin and Conductive Nanomembrane Arrays for Nanomechanical Transducers," *Adv. Mater.*, p. NA–NA, Jul. 2008.
[18] "uhfc1g2_1_2_0-standard-20080511.pdf." .
[19] D. M. Dobkin, *The RF in RFID: passive UHF RFID in practice*. Newnes, 2007.
[20] S. Pellerano, J. Alvarado, and Y. Palaskas, "A mm-Wave Power-Harvesting RFID Tag in 90 nm CMOS," *Solid-State Circuits, IEEE Journal of*, vol. 45, no. 8, pp. 1627–1637, 2010.
[21] V. Rizzoli, A. Costanzo, E. Montanari, and A. Benedetti, "A New Wireless Displacement Sensor Based on Reverse Design of Microwave and Millimeter-Wave Antenna Array," *Sensors Journal, IEEE*, vol. 9, no. 11, pp. 1557–1566, 2009.
[22] D. Gabbay, "Highly Integrated mm-Wave Motion and Proximity Detector Front-End," in *Electrical and Electronics Engineers in Israel, 2006 IEEE 24th Convention of*, 2006, pp. 87–90.
[23] A. Muller, D. Neculoiu, P. Pursula, T. Vaha-Heikkila, F. Giacomozzi, and J. Tuovinen, "Hybrid integrated micromachined receiver for 77 GHz millimeter wave identification systems," in *Microwave Conference, 2007. European*, 2007, pp. 1034–1037.
[24] S. K. Padhi, N. C. Karmakar, C. L. Law, S. Aditya, Z. Shen, and P. Hui, "Microstrip-fed slot antenna for millimetre-wave RFID system," in *Microwave Conference, 2000 Asia-Pacific*, 2000, pp. 1396–1399.
[25] P. Pursula, T. Vaha-Heikkila, A. Muller, D. Neculoiu, G. Konstantinidis, A. Oja, and J. Tuovinen, "Millimeter-Wave Identification—A New Short-Range Radio System for Low-Power High Data-Rate Applications," *Microwave Theory and Techniques, IEEE Transactions on*, vol. 56, no. 10, pp. 2221–2228, 2008.
[26] A. Wu, K. Mahbobi, H. Ghajari, Y. Mykula, and B. Woods, "Passive chip-less millimeter wave Radio Frequency Identification," in *Military Communications Conference, 2008. MILCOM 2008. IEEE*, 2008, pp. 1–7.
[27] C. A. Balanis, *Antenna Theory: Analysis and Design, 3rd Edition*, 3rd ed. Wiley-Interscience, 2005.
[28] Taeik Kim, Uisheon Kim, Gyubong Jung, and Jaehoon Choi, "Design of an UHF RFID tag antenna for paper money management system," in *Microwave Conference, 2009. APMC 2009. Asia Pacific*, 2009, pp. 1056–1059.
[29] R. E. Collin and F. J. Zucker, *Antenna theory. Part 1-2: Inter-university electronics*. McGraw-Hill, 1969.
[30] R. C. Hansen, "Relationships between antennas as scatterers and as radiators," *Proceedings of the IEEE*, vol. 77, no. 5, pp. 659–662, May 1989.
[31] R. B. Green, "The general theory of antenna scattering," OhioLINK / Ohio State University, 1963.
[32] E. F. Knott, M. T. Tuley, and and J. F. Shaeffer, *Radar Cross Section, Second Edition*, 2nd ed. SciTech Publishing, 2004.

[33] Chih-Chuan Yen, A. E. Gutierrez, D. Veeramani, and D. van der Weide, "Radar Cross-Section Analysis of Backscattering RFID Tags," *Antennas and Wireless Propagation Letters, IEEE*, vol. 6, pp. 279–281, 2007.

[34] A. Bletsas, A. G. Dimitriou, and J. N. Sahalos, "Improving Backscatter Radio Tag Efficiency," *Microwave Theory and Techniques, IEEE Transactions on*, vol. 58, no. 6, pp. 1502–1509, 2010.

[35] Yueh-Ying Hu, "Back-scattering cross section of a center-loaded cylindrical antenna," *IRE Transactions on Antennas and Propagation*, vol. 6, no. 1, pp. 140–148, Jan. 1958.

[36] P. B. Khannur, Xuesong Chen, Dan Lei Yan, Dan Shen, Bin Zhao, M. K. Raja, Ye Wu, R. Sindunata, Wooi Gan Yeoh, and R. Singh, "A Universal UHF RFID Reader IC in 0.18-µm CMOS Technology," *IEEE Journal of Solid-State Circuits*, vol. 43, no. 5, pp. 1146–1155, May 2008.

[37] I. Kipnis, S. Chiu, M. Loyer, J. Carrigan, J. Rapp, P. Johansson, D. Westberg, and J. Johansson, "A 900MHz UHF RFID Reader Transceiver IC," in *Solid-State Circuits Conference, 2007. ISSCC 2007. Digest of Technical Papers. IEEE International*, 2007, pp. 214–598.

[38] Jingchao Wang, Chun Zhang, and Zhihua Wang, "A low power low cost fully integrated UHF RFID reader with 17.6dBm output P1dB in 0.18 µm CMOS process," in *2010 IEEE Radio Frequency Integrated Circuits Symposium (RFIC)*, 2010, pp. 109–112.

[39] Ickjin Kwon, Heemun Bang, Kyudon Choi, Sangyoon Jeon, Sungjae Jung, Donghyun Lee, Yunseong Eo, Heungbae Lee, and Bongyoung Chung, "A Single-Chip CMOS Transceiver for UHF Mobile RFID Reader," in *Solid-State Circuits Conference, 2007. ISSCC 2007. Digest of Technical Papers. IEEE International*, 2007, pp. 216–598.

[40] Runxi Zhang, Chunqi Shi, Yihao Chen, Wei He, Ping Xu, Shuai Xu, and Zongsheng Lai, "A single-chip CMOS UHF RFID reader transceiver," in *2010 IEEE Radio Frequency Integrated Circuits Symposium (RFIC)*, 2010, pp. 101–104.

[41] Jeiyoung Lee, Jaehong Choi, Kang Ho Lee, Bonkee Kim, Minsu Jeong, Youngho Cho, Heeyong Yoo, Kyoungon Yang, S. Kim, Seong-Mo Moon, Jae-Young Lee, Sangkyu Park, Wanchul Kong, Jin Kim, Tae-Ju Lee, Bo-Eun Kim, and Beom-Kyu Ko, "A UHF Mobile RFID Reader IC with Self-Leakage Canceller," in *2007 IEEE Radio Frequency Integrated Circuits (RFIC) Symposium*, 2007, pp. 273–276.

[42] A. Safarian, A. Shameli, A. Rofougaran, M. Rofougaran, and F. De Flaviis, "An Integrated RFID Reader," in *Solid-State Circuits Conference, 2007. ISSCC 2007. Digest of Technical Papers. IEEE International*, 2007, pp. 218–598.

[43] T. Boles, R. Houlihan, and C. Weigand, "An HMIC I/Q modulator/demodulator for RFID applications," in *Microwave Conference Proceedings, 2005. APMC 2005. Asia-Pacific Conference Proceedings*, 2005, vol. 2.

[44] J. Bae, K. Kim, W. Choi, C. Park, and C. Pyo, "Study on the reader baseband receiver structure for the demodulation of subcarrier signal in a passive RFID environment," *Microwave and Optical Technology Letters*, vol. 53, no. 6, pp. 1264–1272, Jun. 2011.

[45] Jingchao Wang, Baoyong Chi, Xuguang Sun, Tongqiang Gao, Chun Zhang, and Zhihua Wang, "System design considerations of highly-integrated UHF RFID reader transceiver RF front-end," in *Solid-State and Integrated-Circuit Technology, 2008. ICSICT 2008. 9th International Conference on*, 2008, pp. 1560–1563.

[46] "Impinj Indy RFID Reader Chips." [Online]. Available: http://www.impinj.com/Indy_RFID_Reader_Chips.aspx. [Accessed: 17-Jan-2012].

[47] “LT5516 - 800MHz to 1.5GHz Direct Conversion Quadrature Demodulator - Linear Technology.” [Online]. Available: http://www.linear.com/product/LT5516. [Accessed: 17-Jan-2012].
[48] “LT5575 - 800MHz to 2.7GHz High Linearity Direct Conversion Quadrature Demodulator - Linear Technology.” [Online]. Available: http://www.linear.com/product/LT5575. [Accessed: 17-Jan-2012].
[49] “MAX2021 High-Dynamic-Range, Direct Up-/Downconversion, 750MHz to 1200MHz Quadrature Modulator/Demodulator - Overview.” [Online]. Available: http://www.maxim-ic.com/datasheet/index.mvp/id/3451. [Accessed: 17-Jan-2012].
[50] “ADF9010 | 900MHz ISM Band Analog RF Front End | Modulators / Demodulators | RF / IF ICs | Analog Devices.” .
[51] “DATA SHEET SKY73012: 400 – 3900 MHz Direct Quadrature Demodulator. http://www.skyworksinc.com/uploads/documents/200473B.pdf.” .
[52] S. Verdú, *Multiuser Detection*. Cambridge University Press, 1998.
[53] S. Thomas and M. S. Reynolds, “QAM backscatter for passive UHF RFID tags,” in *RFID, 2010 IEEE International Conference on*, 2010, pp. 210–214.
[54] Huan-Yang Chen, A. Bhadkamkar, Tzu-Han Chou, and D. W. van der Weide, “Vector backscattered signal analysis of piggyback modulation for passive UHF RFID Tags,” in *Microwave Symposium Digest (MTT), 2011 IEEE MTT-S International*, 2011, pp. 1–4.
[55] R. F. Harrington, “Theory of loaded scatterers,” *Electrical Engineers, Proceedings of the Institution of*, vol. 111, no. 4, pp. 617–623, 1964.
[56] S. Thomas and M. S. Reynolds, “QAM backscatter for passive UHF RFID tags,” in *2010 IEEE International Conference on RFID*, 2010, pp. 210–214.
[57] K. V. S. Rao, P. V. Nikitin, and S. F. Lam, “Antenna design for UHF RFID tags: a review and a practical application,” *Antennas and Propagation, IEEE Transactions on*, vol. 53, no. 12, pp. 3870–3876, 2005.
[58] Gi-Chul Jung, Hong Kyun Ryu, Sungkyun Lim, and Jong Myung Woo, “Design of a spherical-shaped, UHF RFID tag antenna with 3-axes polarization,” in *Antennas and Propagation Society International Symposium, 2009. APSURSI ’09. IEEE*, 2009, pp. 1–4.
[59] Chihyun Cho, Hosung Choo, and Ikmo Park, “Design of UHF Small Passive Tag Antennas,” vol. 2B, pp. 349–352.
[60] G. Marrocco, “Gain-optimized self-resonant meander line antennas for RFID applications,” *IEEE Antennas and Wireless Propagation Letters*, vol. 2, no. 1, pp. 302–305, 2003.
[61] P. Wongsiritorn, C. Phongcharoenpanich, D. Torrungrueng, and M. Krairiksh, “UHF-RFID tag antenna design using dipole with parasitic lines,” in *Electrical Engineering/Electronics, Computer, Telecommunications and Information Technology, 2009. ECTI-CON 2009. 6th International Conference on*, 2009, vol. 02, pp. 794–797.
[62] P. R. Foster, “Antenna problems in RFID systems,” 1999, vol. 1999, p. 3–3.
[63] W. L. Stutzman and G. A. Thiele, *Antenna Theory and Design*, 3rd ed. Wiley, 2012.
[64] D. M. Dobkin and S. M. Weigand, “Environmental effects on RFID tag antennas,” in *Microwave Symposium Digest, 2005 IEEE MTT-S International*, 2005.
[65] J. D. Griffin, G. D. Durgin, A. Haldi, and B. Kippelen, “RF Tag Antenna Performance on Various Materials Using Radio Link Budgets,” *IEEE Antennas and Wireless Propagation Letters*, vol. 5, no. 1, pp. 247–250, Dec. 2006.

[66] K. M. Ramakrishnan and D. D. Deavours, “Performance Benchmarks for Passive UHF RFID Tags,” in *Measuring, Modelling and Evaluation of Computer and Communication Systems (MMB), 2006 13th GI/ITG Conference*, 2006, pp. 1–18.

[67] P. Raumonen, L. Sydanheimo, L. Ukkonen, M. Keskilammi, and M. Kivikoski, “Folded dipole antenna near metal plate,” in *IEEE Antennas and Propagation Society International Symposium, 2003*, 2003, vol. 1, pp. 848– 851 vol.1.

[68] Tae-Wan Koo, Dongsu Kim, Jong-In Ryu, Hae-Moon Seo, Jong-Gwan Yook, and Jun-Chul Kim, “Design of a Label-Typed UHF RFID Tag Antenna for Metallic Objects,” *Antennas and Wireless Propagation Letters, IEEE*, vol. 10, pp. 1010–1014, 2011.

[69] Lingfei Mo and Chunfang Qin, “Planar UHF RFID Tag Antenna With Open Stub Feed for Metallic Objects,” *Antennas and Propagation, IEEE Transactions on*, vol. 58, no. 9, pp. 3037–3043, 2010.

[70] J. F. White, *High Frequency Techniques: An Introduction to Rf and Microwave Engineering*. John Wiley & Sons, 2004.

[71] P. Pursula, D. Sandstrom, and K. Jaakkola, “Backscattering-Based Measurement of Reactive Antenna Input Impedance,” *Antennas and Propagation, IEEE Transactions on*, vol. 56, no. 2, pp. 469–474, 2008.

[72] B. Monsalve, S. Blanch, J. Romeu, and L. Jofre, “A contact-less small antenna characterization through impedance modulation,” in *Antennas and Propagation, 2009. EuCAP 2009. 3rd European Conference on*, 2009, pp. 696 –698.

[73] P. V. Nikitin, K. V. S. Rao, R. Martinez, and S. F. Lam, “Sensitivity and Impedance Measurements of UHF RFID Chips,” *Microwave Theory and Techniques, IEEE Transactions on*, vol. 57, no. 5, pp. 1297–1302, 2009.

[74] L. W. Mayer and A. L. Scholtz, “Sensitivity and impedance measurements on UHF RFID transponder chips,” in *2nd Int. EURASIP RFID Technol. Workshop, Budapest, Hungary*, 2008.